UNIVERSITY OF OSLO
Department of Chemistry

Defect chemistry and DFT modelling of $La_3Ta_{0.5}Ga_{5.5}O_{14}$

Master thesis in Materials, energy and nanotechnology (MENA)

Vijay Shanmugappirabu

June 3rd 2013

Preface

This master thesis is a part of the "Material, Energy and Nanotechnology" program at the Department of Chemistry, University of Oslo. The experimental work presented in this thesis was done in the laboratories of Centre for Material science and Nanotechnology (SMN) in the time period August 2011 to June 2013. For the DFT calculations the supercomputer Abel at the University of Oslo was made use of.

This thesis was written in Microsoft Word 2010, and Endnote was used as the citation tool. The crystallographic figures were represented in Vesta, and figures and plots were made in Origin. It should be noted that "." has been used as decimal separator in this thesis, with the exception of some Origin figures where "," has been used.

I would like to thank my supervisor Truls Norby and my co-supervisor Tor Bjørheim for much guidance and discussion, especially in the DFT part of the thesis.

Vijay Shanmugappirabu
(University of Oslo, June 2013)

Abstract

Langatate (LGT) is a piezoelectric oxide used in the high temperature region. As opposed to α-quartz, which is the most used piezoelectric today, langatate preserves its piezoelectric properties at temperatures up to 1470 °C. The defect chemistry of langatate has, however, not been fully understood. In this thesis, this will be addressed through AC impedance spectroscopy and DFT calculations.

The defect chemistry and conductivity of nominally undoped and acceptor doped polycrystalline langatate, as well as single crystals, has been studied through impedance spectroscopy in the temperature range from 400 up to 1200 °C in oxygen partial pressure of 1 to 10^{-5} atm, as well as water vapour partial pressure of approximately 10^{-2} to 10^{-5} atm. Measurements have shown that the nominally undoped langatate was effectively donor doped and was compensated by oxygen interstitial and probably some cation vacancy. This sample showed no significant effect of either pO_2 or pH_2O on the conductivity at temperatures up to 1200 °C, and did not show any sign of degradation in oxidizing or inert conditions, making it ideal for use as a piezoelectric in varying atmospheric conditions. The major charge carrier is interstitial oxygen and its enthalpy of mobility was calculated to 89±4 kJ/mol.

In the nominally 2.5 mol% gallium doped polycrystalline langatate the major charge compensating defect was oxygen vacancies. These defects dominate the conductivity in dry conditions at low pO_2 at temperatures up to at least 1000 °C. In wet conditions at temperatures below 700 °C the major charge carrier was protons with enthalpy of mobility of 70±0.5 kJ/mol. From DFT calculations using GGA-PBE exchange-correlation potential a favourable hydration enthalpy of -90 kJ/mol was obtained. DFT results showed that hydration involves vacancies and protons near the gallium ions, which might indicate that increasing the gallium content, might be favourable to the protonation of the material. At higher temperatures and high pO_2 there are significant contributions from electron holes. This composition of langatate could be ideal for use as a humidity sensor at temperatures up to 700 °C.

The Z-cut and X-cut single crystalline langatate showed similar behaviour as the acceptor doped polycrystalline langatate, *i.e.* it must be effectively acceptor doped

with gallium excess. These crystals however exhibited a slight anisotropic effect where proton transport along the xy-plane is more favourable than along the z-axis. Langatate is a modest proton conductor compared to other proton conducting oxides.

Table of contents

1. Introduction

Langatate (LGT), $La_3Ga_{5.5}Ta_{0.5}O_{14}$, is a *high temperature piezoelectric* oxide, which belongs to the so-called langasite family. One of the key properties of these materials is that there are no phase transitions below the melting point. Langatate remains piezoelectric up to its melting point at 1470 °C, as opposed to the most common piezoelectric today, α-quartz, which loses the effect at its phase transition at 573 °C (Curie point). [4] The main uses of piezoelectric materials is as sensors and resonators, and langatate is increasingly used as a piezoelectric material in the high temperature range.

All materials will at any given temperature have defects, and as the temperature rises, the defect concentration generally increases. The mobility increases as well with temperature for the atoms/defects, which enables thermodynamic equilibrium between the material and its surroundings. Since the piezoelectric effect is based on the displacement of atoms relative to each other, it is expected that the properties of the material will be sensitive to various kinds of defects in the structure. One type of defect is protons. Protons have been reported in langasite by Bjørheim *et al.* [5] and Schulz *et al.* [2] among others. Fritze *et al.* reported that the uptake of protons in langasite affects the conductivity of the material at temperatures up to 800 °C [6]. In other studies of langasite and the other oxides in the same family, the effect of protons is not investigated. However, it has been shown for other structure classes, *e.g.* perovskites and monazites, that the concentration and transport properties of protons vary with the composition of the oxide [7] [8] [9]. Protons are positively charged, and the concentration of these can be changed by doping the material with an effectively negative charged dopant. This is called acceptor doping.

It has been shown that the langasite family is subjected to degradation and chemical instability at higher temperatures, as well as loss in conductivity and deviation from stoichiometry. [6] To achieve a better understanding of this and investigate the proton content and transport properties, the defect chemistry has to be addressed. As of date, there has been little work on the defect chemistry of langatate, contrary to langasite, which has been studied extensively.

1.1 Piezoelectricity

Piezoelectricity was first discovered in 1880 by the brothers Jacques and Pierre Curie. The first major application was for military use as a transducer in sonar, *i.e.* a device that converts one type of energy to another, in this case, electrical energy to acoustic energy. However, today, piezoelectric devices have a vast application; from production and detection of sound in the music industry to high-precision mechanical instruments, *e.g.* in a SEM, and every day consumables like lighters.

A piezoelectric is a material which has a linear relationship between mechanical stress and electric voltage. An applied pressure in a specific crystallographic direction will generate electric charges on the surface of the material. This is called the direct piezoelectric effect. These materials also show the converse piezoelectric effect; an applied electric field will deform the material. This property has its origin in the crystal structure of the material. When the crystal is deformed in a specific crystallographic direction, the positive and negative charges in the material are distorted relative to each other such that a dipole moment is created (Figure 1). Only structures with no inversion symmetry exhibit the piezoelectric effect. Because of the direct and converse piezoelectric effect, these materials are capable of acting both as a sensor and as a transmitter. [10]

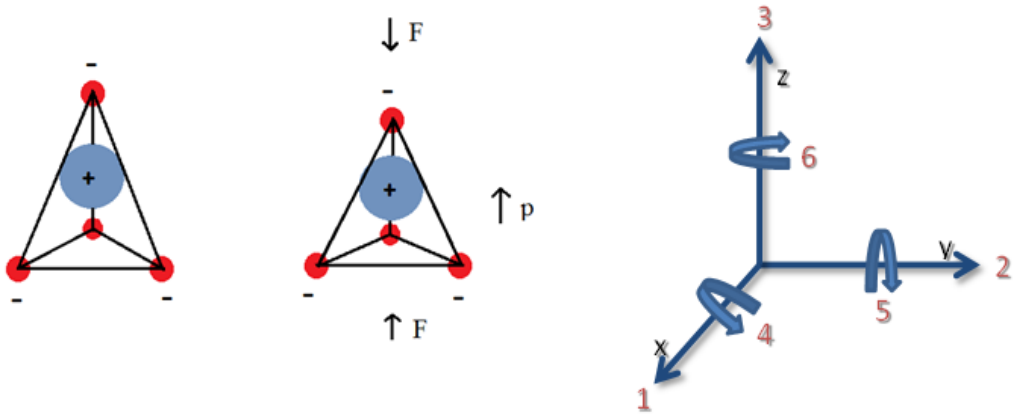

Figure 1 An example of piezoelectricity. When the tetrahedron is strained, as in the middle figure, there is a relative displacement of the negative and positive charge centres. This results in a dipole. When this is reproduced across the periodic crystal, the surfaces of the material will have positive and negative charge on opposite surfaces. On the right, the different terms used to describe the directions of the piezoelectric effect.

In piezoelectric materials three axes are defined; 1, 2 and 3, where the latter refers to the polar axis and the two former refer to arbitrarily chosen orthogonal axes perpendicular to the polar axis. Shear stress about the three aforementioned axes, are represented by 4, 5 and 6, respectively (see Figure 1). The relationship between the applied force and the resultant charge is expressed through the piezoelectric coefficient, e_{ij}, expressed in C/m^2 for the direct piezoelectric effect. The double subscript links the electrical and mechanical quantities. The first subscript gives the direction of the applied electric field (or the charge produced), while the second subscript gives the direction of the strain produced (or the force applied). For instance e_{13} describes the relationship of an applied electric field along the x-axis and the resultant strain along the z-axis, or conversely the electric field generated along the x-axis as a consequence of an applied stress along the z-axis. A large value means large electric charge induced with little mechanical stress, or large mechanical strain generated at small cost of electric field.

1.2 Proton conduction

Many materials exhibit significant proton conduction. These materials are used as electrolytes in fuel cells where protons dissociate from hydrogen gas and get absorbed in the material (Eq. 1). They are also used as hydrogen separation membranes.

$$H_2 = 2H^+ + 2e^- \qquad \text{Eq. 1}$$

One of the most popular materials for proton conduction today is Y-doped $BaZrO_3$-based oxides. These materials exhibit high stability and conductivity at temperatures below 700 °C. [11] In Figure 2 proton conductivities of various oxides are shown as a function of temperature. The conductivities were calculated from data on proton concentrations and mobilities by Norby. [12]

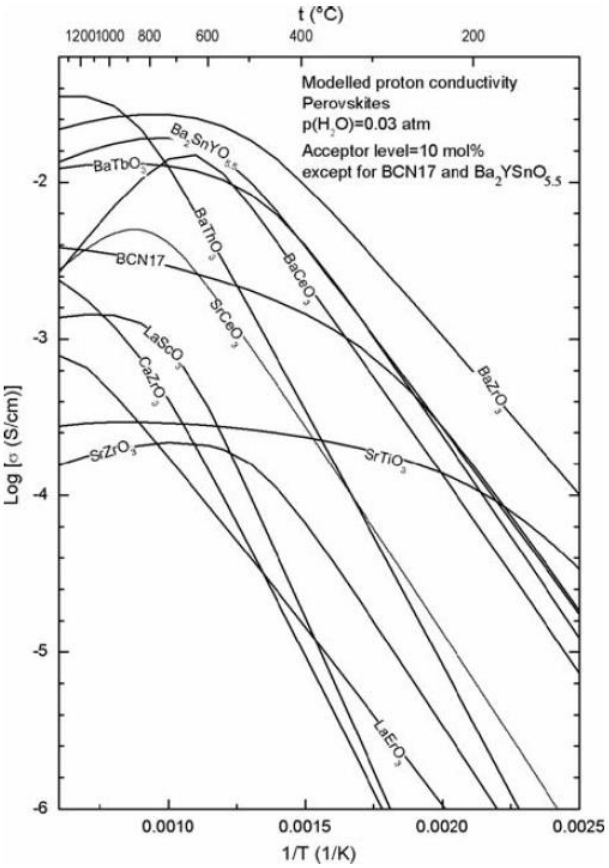

Figure 2 The proton conductivity vs. temperature of various acceptor doped perovskites according to Norby calculated from data on proton concentrations and mobilities. Figure is from [12].

The langasite family is a new interesting material group where there have been hardly any studies on the proton conductivity.

1.3 Langatate

Langatate belongs to the langasite family and crystalizes in the calcium gallium germanate structure ($Ca_3Ga_2Ge_4O_{14}$), with the space group P321 (150). These materials belong to the same crystal class as α-quartz. In langatate there are 4 different cation-sites and the general formula is $A_3B_3C_2DO_{14}$ ($La_3Ga_3Ga_2[Ga_{0.5}Ta_{0.5}]O_{14}$). La^{3+} occupies the 3e dodecahedron sites while Ga^{3+} occupies the tetrahedral 3f and 2d sites. These tetrahedra form a network with each other where the 3f site tetrahedra are connected with other tetrahedra on two of the vertices, and the 2d site tetrahedra are connected on three of the vertices (Figure 3). The 1a octahedral sites, which constitute the corners of the unit cell, are occupied by Ga^{3+} and Ta^{5+}, each with an half occupancy (see Table 1), which makes this a disordered cation site. In undoped langatate the ratio of tantalum and gallium on the 1a site is 1. By manipulating this ratio (Eq. 2), the defect structure of langatate can be changed. Increasing the ratio ($x > 1$) would make the material acceptor doped while decreasing this ratio ($x < 1$) would make it donor-doped.

$$\frac{Ga_{1a}}{Ta_{1a}} = x \qquad \text{Eq. 2}$$

Table 1 The different cation and anion sites in langatate crystal.

Site	Wyckoff position	Cation / anion	Fractional coordinate	Polyhedral
D	1a	Ta^{5+}, Ga^{3+}	(0.0 0.0 0.0)	Octahedron
C	2d	Ga^{3+}	(0.3333 0.6667 0.4687)	Tetrahedron
A	3e	La^{3+}	(0.4259 0.0 0.0)	Dodecahedron
B	3f	Ga^{3+}	(0.7618 0.0 0.5)	Tetrahedron
	2d	O^{2-}	(0.3333 0.6667 0.824)	
	6g	O^{2-}	(0.4518 0.3056 0.704)	
	6g	O^{2-}	(0.2172 0.0731 0.243)	

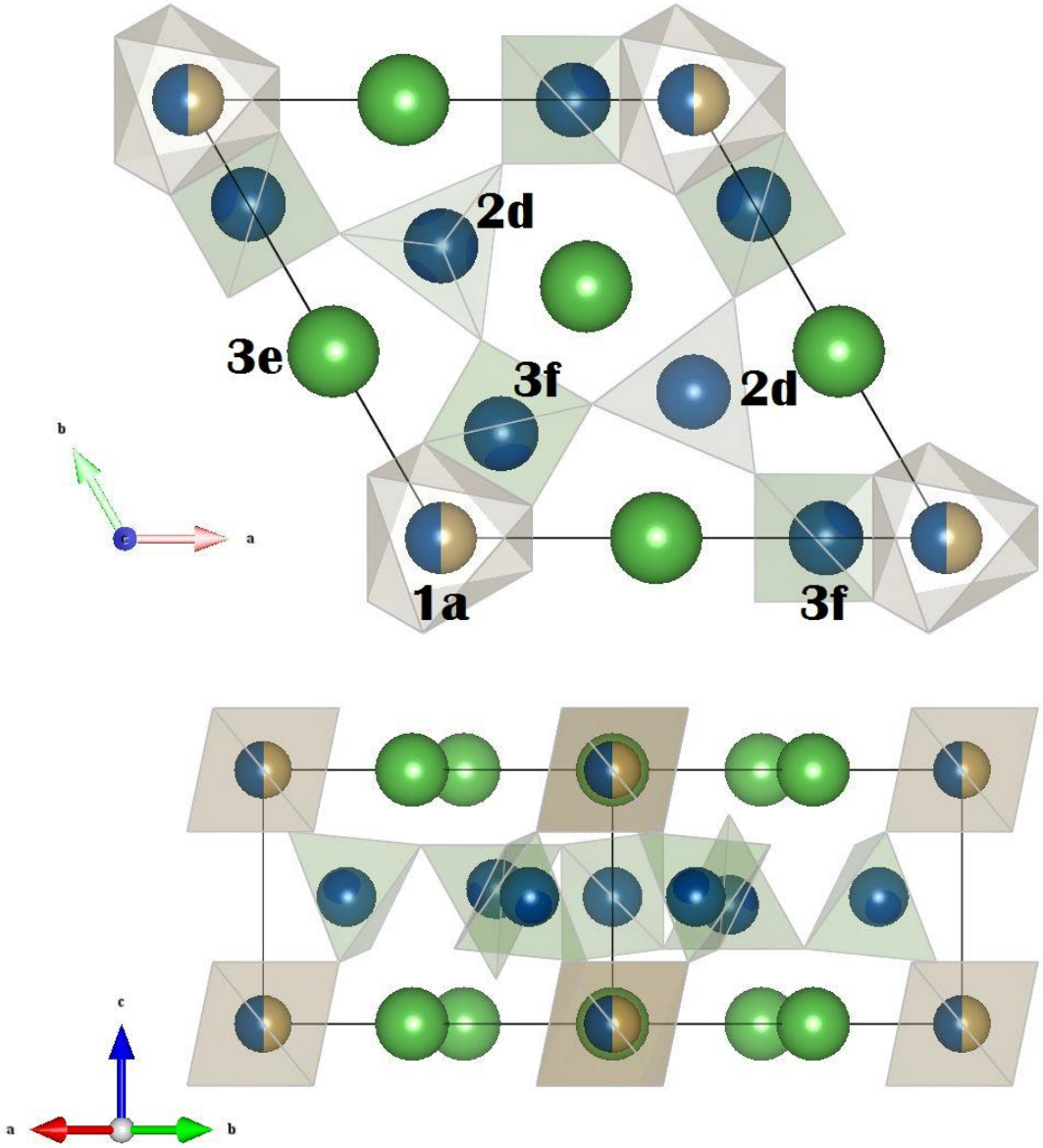

Figure 3 On the top figure, the crystal structure of langatate seen toward the z-axis. The 3e sites are occupied by La^{3+} (green), the 3f & 2d sites are occupied by Ga^{3+} (blue), the 1a site is occupied by both Ga^{3+} and Ta^{5+} (brown) in a 1-1 ratio. The corners of the polyhedra are oxygen ions. On the lower figure, the same structure is seen along the xy-plane.

1.4 Definition of the task

The main goal of this thesis is to understand the defect chemistry of langatate and predict how temperature and different atmospheric conditions will affect the conductivity and transport properties. Langatate samples with different compositions will be investigated. The uptake of protons will be investigated with respect to the doping level and the type of dopant, and values for mobility of different defect species will be obtained. The hydration enthalpy for the material will be examined. In addition to the experimental studies, a theoretical study of the material will be done through Density Functional Theory (DFT) calculations with the program VASP. In this part of the study it will be focused on cation configurations, different defects, local arrangements of the protons and their effect on the structure, as well as thermodynamics for incorporation of protons.

Both polycrystalline and single crystal langatate will be measured upon and compared through AC impedance spectroscopy from temperatures of 400 °C up to 1200 °C, mainly in mixtures of O_2/Ar with a varying water vapour partial pressure. Any anisotropic effects along the two unique crystallographic directions, x/y and z, will be investigated, specifically the proton transport along these directions.

2. Theory

The content of this chapter is mainly based on the compendium “Defects and Transport in Crystalline Solids” [13]. In addition, the compendium “Electrical Measurements” by Truls Norby has been used as reference for the theory on impedance spectroscopy [14].

2.1 Defect chemistry

In a perfect crystal the constituent atoms are all ordered in a strictly periodic manner with each atom type occupying certain defined positions. However, in reality, a perfect crystal is rare. In theory a perfect crystal can only exist at absolute zero (0 K). At temperatures above 0 K defects will appear in the crystal. The defects are simply irregularities from the perfect structure. Nevertheless, defects can still exist at 0 K if they were frozen.

There are several types of defects in a crystal; 0-, 1-, 2- and 3-dimensional defects. 0-dimensional defects are known as point defects and they are constrained to one structural site and its immediate region. Examples of these types of defects are cation and anion vacancies (an empty structural position) and interstitial atoms. 1-dimensional defects, such as dislocations, extend in one direction. 2-dimensional defects, also known as plane defects, comprise grain boundaries, interfaces, stacking faults and external surfaces. A secondary phase is an example of a 3-dimensional defect. In addition to these structural defects, electronic defects might occur as well in a crystal, as both electrons and holes.

Intrinsic defects are introduces in a crystal without any external influence. Examples of these types of defects are Schottky pair, which is an anion and cation vacancy pair, and Frenkel disorder, which is a cation/anion interstitial and a cation/anion vacancy. Intrinsic disorder is not limited to atoms however. An electron-hole pair is also a result of internal disorder. Extrinsic defects, on the other hand, are a term for foreign atoms in the crystal, either placed there unintentionally as impurities or intentionally as a dopant.

To describe point defects in a crystalline solid, Kröger-Vink notation is used. An element (atoms, ions or electron/holes) is identified with a major letter, and the position it occupies is identified with a subscript. For instance, a vacancy on a metal site is simply noted as v_M. However, this is not a complete notation. We have to describe the charge as well. Effective positive charge is denoted "•", while effective negative charge is expressed by "/". Effective neutral charge is expressed by an "x". This is not to be confused with formal charge. The effective charge is expressed as the difference between the charge of the element occupying the site and the charge of the element that should occupy the site in a perfect defect free crystal. In the case of the metal vacancy, if we assume the formal charge of a vacancy to be 0, and the formal charge of the metal to be 2+, the notation for the vacancy would be v_M''. Other examples for the notation is fully ionised oxygen vacancy $v_O^{\bullet\bullet}$, defect electrons in the conduction band e', holes in the valence band $h^{\bullet}$, and finally a non-defective species, a gallium ion on a gallium site Ga_{Ga}^{x}.

The formation of oxygen vacancies is described in Eq. 3 with Kröger-Vink notation.

$$O_O^{\times} = v_O^{\bullet\bullet} + 2e' + \frac{1}{2}O_2(g) \qquad \text{Eq. 3}$$

This reaction can be expressed with its equilibrium constant (Eq. 4) which relates the concentrations and the oxygen partial pressure.

$$K_{v_O^{\bullet\bullet}} = \frac{\frac{[v_O^{\bullet\bullet}]}{[O]}\left(\frac{n}{N_c}\right)^2}{\frac{[O_O^x]}{[O]}}\left(\frac{p_{O_2}}{p_{O_2}^0}\right)^{1/2} \qquad \text{Eq. 4}$$

The [O] is the total concentration of oxygen sites (occupied and vacant), n is the concentration of defect electrons, N_c is the density of states in the conduction band (*i.e.* total concentration of sites), and $[O_O^x]$ is the concentration of oxygen. For low defect concentration some simplifications are made; The N_c part is incorporated into the equilibrium constant, the $p_{O_2}^0$ is set to 1 bar, and $[O_O^x]$ is set equal to the amount oxygen per oxide.

$$K'_{v_O^{\bullet\bullet}} = N_C^2 K_{v_O^{\bullet\bullet}} = \frac{[v_O^{\bullet\bullet}] n^2 p_{O_2}^{1/2}}{[O_O^x]} = \exp\left(\frac{-\Delta G_{v_O^{\bullet\bullet}}}{RT}\right)$$ Eq. 5

One of the most significant reactions for absorption of protons in oxides is the uptake of water (Eq. 6).

$$H_2O(g) + v_O^{\bullet\bullet} + O_O^{\times} = 2OH_O^{\bullet}$$ Eq. 6

The Gibbs energy of this reaction is termed the Gibbs energy of hydration. Many oxides show negative standard hydration energy meaning it is thermodynamically favourable to absorb protons in the material. The equilibrium constant for the hydration reaction is expressed by Eq. 7.

$$K_{Hydr} = \frac{[OH_O^{\bullet}]^2}{[v_O^{\bullet\bullet}][O_O^x] p_{H_2O}} = \exp\left(\frac{-\Delta G^{\circ}_{Hydr}}{RT}\right)$$ Eq. 7

In Eq. 8 the formation of an electron-hole pair is displayed. The equilibrium constant for the intrinsic ionisation is given by Eq. 9.

$$0 = e' + h^{\bullet}$$ Eq. 8

$$K_i = \frac{np}{N_c N_V} = \exp\left(-\frac{E_g}{RT}\right)$$ Eq. 9

n and p are the concentrations of electrons and holes, respectively, N_C and N_V are the density of states in the conduction and valence band, respectively, and E_g is the band gap.

2.1.1 Point defects in oxides

Common point defects one generally found in oxides are vacancies on the different cation and anion sites, substitutional and interstitial defects, as well as electronic defects. By doping with a defect with effective positive charge, the material becomes donor-doped, while doping with effective negative charged defects would make it acceptor-doped. For both cases the charge introduced has to be compensated by an effectively negative/positive charged defect to uphold the charge balance in the

material, which is ensured by the electroneutrality. The electroneutrality for an acceptor doped oxide with a doubly effective negative charge might look something like Eq. 10.

$$2[v_O^{\bullet\bullet}] + [OH_O^{\bullet}] + p = 2[Acc''] + 2[O_i''] + n \qquad \text{Eq. 10}$$

One can always include more defects, *e.g.* metal vacancies, in the electroneutrality, however it is generally assumed that some defects dominate in concentration and simplifications can be made.

In Figure 4 Brouwer diagrams for an acceptor doped oxide is shown, with pH_2O (left) and pO_2 (right) dependencies. As can be seen, the figures are sectioned into parts where some defects are the dominating species. In each section, the dependencies of the minority defects are shown as well.

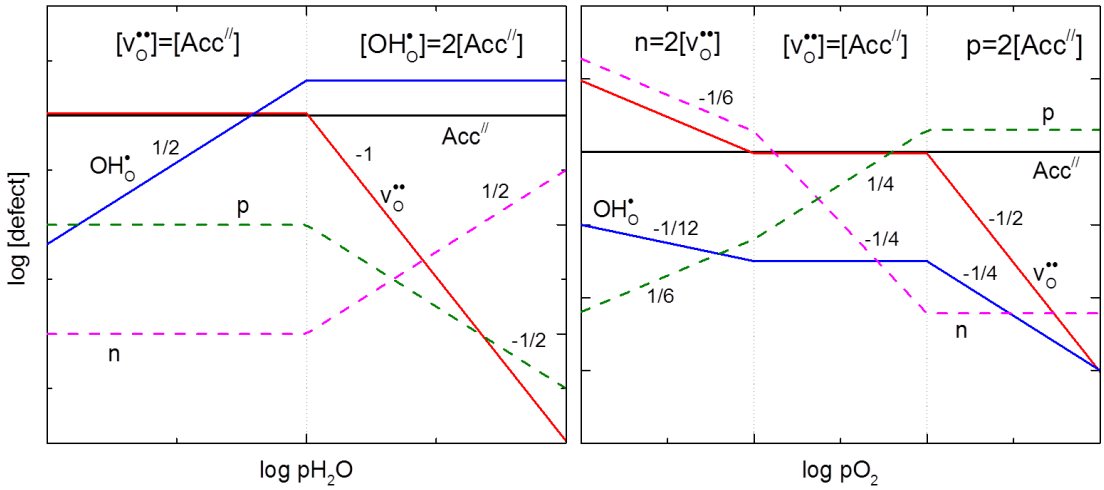

Figure 4 Brouwer diagrams of an acceptor doped oxide with pH_2O dependency (left) and pO_2 dependency (right).

At lower water vapour partial pressures, the oxygen vacancy concentration is locked by the acceptor content. Only the concentration of protons will be affected by the pH_2O at this range, which has the dependency $[OH_O^{\bullet}] \propto p_{H_2O}^{1/2}$. At higher water vapour partial pressure, the acceptor content will be fully compensated by protons, and the concentration of protons will thus be constant as a function of pH_2O. The concentration of oxygen vacancies and holes will vary with $p_{H_2O}^{-1}$ and $p_{H_2O}^{-1/2}$ dependency, respectively.

The pO_2 dependency is sectioned into three parts. At the lowest partial pressures oxygen vacancies dominate, compensated by electrons. In the middle part, the acceptor content is compensated by oxygen vacancies. In this region electrons and holes will have $p_{O_2}^{-1/4}$ and $p_{O_2}^{1/4}$ dependencies. At higher partial pressures, the acceptor content is compensated by electron holes.

2.2 Electrical conductivity

The transport properties of oxides are determined by transport of various electrical charge carriers. The charge carriers can be ionic species, such as protons and oxide ions, and electronic species. The total conductivity can be given by the sum of the ionic and electronic conductivities, as displayed on Eq. 11.

$$\sigma_{Tot} = \sigma_{Ionic} + \sigma_{Electronic} \quad \text{Eq. 11}$$

The partial conductivity of the individual defect species is given by Eq. 12.

$$\sigma_i = z_i e c_i u_i \quad \text{Eq. 12}$$

The charge is given by $z_i e$, where e is the elemental charge, c_i is the concentration given in mole fractions, and u_i the mobility of the species. By replacing the elemental charge by Faradays constant, F, and multiplying with the molar density of the oxide, we obtain charge per volume density times the mobility, giving conductivity.

Point defects diffuse through the oxide matrix by an activated hopping mechanism. The mechanism is expressed by the mobility. The point defects jump from their original site to another available site, either a vacant site or an interstitial site. This requires the ion to pass an energy barrier, the activation energy of the jump, ΔH_{mob}, which is attributed to the coulombic energy the ion experiences by pressing past nearby ions. This is expressed by the mobility. By using the Nernst-Einstein relation, the mobility of point defect can be expressed with the diffusivity, D_i, of that particular species.

$$u_i = z_i e \frac{D_i}{RT} \quad \text{Eq. 13}$$

The mobility of a defect which behaves with an activated hopping mechanism shows Arrhenius-type behaviour.

$$u_i = u_{0,i}\frac{1}{T}\exp\left(-\frac{\Delta H_{mob,i}}{RT}\right) \quad \text{Eq. 14}$$

This mechanism is also assigned to small polarons in oxides at temperatures above roughly 500 °C. A polaron is a fictitious particle; it's composed of the electron/hole and the entire deformation that is created when the electron/hole is moving through the lattice. A large polaron has relatively weak interactions between the electron/hole and the lattice and flows through the lattice almost in the same way as free gas, while a small polaron has a strong interaction with the lattice and the interaction is more localized. The dimension of a small polaron is smaller than the lattice parameter.

2.3 Electrical measurements and analysis

One of the ways to examine a materials electrical transport properties is through impedance spectroscopy. An impedance spectrometer measures the impedance of the sample by applying an alternating current (AC current). In contrast to direct current, the voltage, U, and current, I, oscillate as a sinusoidal wave with time, changing from its highest value, U_0 and I_0, to its lowest value, $-U_0$ and $-I_0$ with an angular frequency of ω, as given by Eq. 15 and Eq. 16, respectively.

$$U(t) = U_0 \sin(\omega t) \quad \text{Eq. 15}$$

$$I(t) = I_0 \sin(\omega t + \theta) \quad \text{Eq. 16}$$

The impedance, Z, is a measure of the opposition a flow of current in a circuit experiences, as a voltage is applied. The impedance consists of a real part, the resistance, R, and an imaginary part, the reactance, X.

$$Z = R + jX \quad \text{Eq. 17}$$

The admittance, Y, of the sample is a measure of how easily current flows through a circuit and is given by the inverse of the impedance. Like the impedance, admittance

consists of a real part, the conductance, G, and an imaginary part, the susceptance, B, given by Eq. 18.

$$Y = \frac{1}{Z} = G + jB \qquad \text{Eq. 18}$$

2.3.1 Passive circuit elements

There are three passive circuit elements considered in this thesis; resistors (R), capacitors (C) and inductors (L). A resistor is an element which has long-range transport of charge carriers. In an ideal resistor an AC voltage gives an instant rise in current, and vice versa, and thus the AC voltage and current are in phase. A capacitor is an element that can store charge. It consists of an ideal insulator sandwiched between two conductors. In the case of the capacitor, the current is phase-shifted by 90° ahead of the AC-voltage. The capacitance is given by Eq. 19, where ε_0 is the permittivity of free space, ε_r the relative dielectric constant, A the electrode surface area and t the thickness separating the electrodes.

$$C = \varepsilon_0 \varepsilon_r \frac{A}{t} \qquad \text{Eq. 19}$$

Finally, an inductor is ideally a conductor with no resistance (usually formed as a coil). When AC current is passed through it, a magnetic field is formed around it which in turn induces an AC voltage with opposite direction of the original applied voltage. In an inductor the current is 90° behind the voltage.

2.3.2 Constant frequency measurements

Constant frequency measurements, commonly called “ramps”, are measurements of total impedance, Z, where the frequency and voltage are held constant while the temperature is dropped at a constant rate. By correcting for geometry total conductivity σ is obtained (Eq. 20). The thickness of the sample is noted l, and A is the area of the electrode.

$$\sigma_{Tot} = \frac{1}{R}\frac{l}{A} = G\frac{l}{A} \qquad \text{Eq. 20}$$

The ramps are usually plotted with the logarithm of conductivity as a function of inverse temperature. Activation energies can be obtained by fitting the curve with an Arrhenius equation, Eq. 21.

$$\sigma_i = \frac{\sigma_0}{T}\exp\left(-\frac{E_a}{RT}\right) \qquad \text{Eq. 21}$$

2.3.3 Impedance spectroscopy

Impedance spectroscopy is impedance measurements where only the frequency is varied. The oscillation voltage is kept constant while the impedance measurement is run from high frequency to low frequency. The result is plotted in a Nyquist diagram, where the x-axis represents the real part of the impedance, resistance, and the y-axis represents the imaginary part, reactance. A typical impedance spectrum is shown in Figure 5. The frequency of the data points decreases as we move to the right.

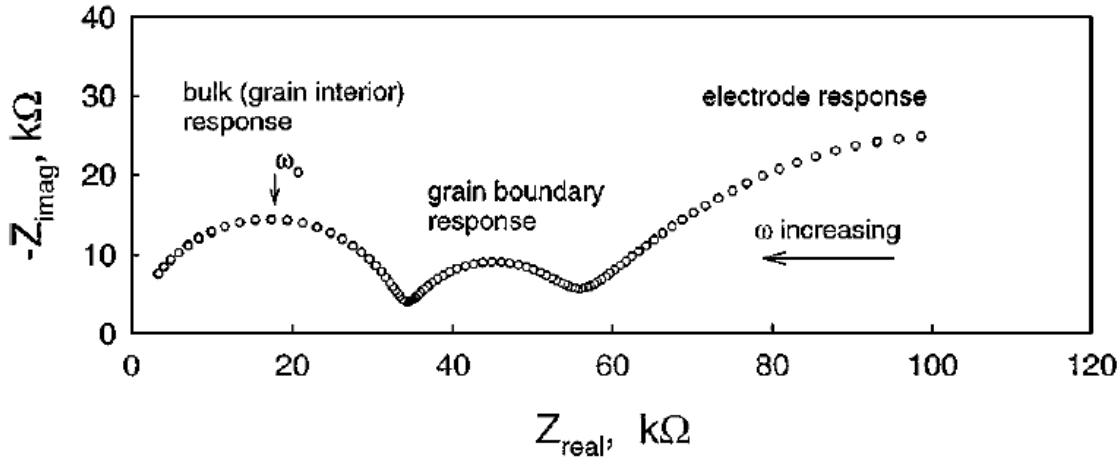

Figure 5 Nyquist diagram of the impedance of a polycrystalline sample. Figure from [7].

As seen on the figure, when performing impedance spectroscopy we can get impedance spectra consisting of several semicircles. These semicircles represent different parts of the sample, which depends on the peak frequency, ω_0 (Eq. 22). The peak frequency is the maxima of the semicircles as seen in Figure 5. The diameters of the semicircles represent roughly the resistance of the different parts of the sample.

$$\omega_0 = \frac{1}{RC} = \frac{\sigma}{\varepsilon_0 \varepsilon_r} \qquad \text{Eq. 22}$$

It is assumed that the dielectric constant in a material does not differ in bulk and grain boundary, thus the reason for getting separate semicircles is attributed to difference in conductivity. If the bulk conductivity is higher than the grain boundary conductivity, as is the case in Figure 5, the first semi-circle would then represent the bulk while the

second would represent serial grain boundary. It can be seen that the grain boundary resistance is much smaller than the bulk resistance; however, one must take into account the much smaller total thickness of the grain boundaries. This would in turn give a higher resistivity, and thus a lower conductivity [7]. From Eq. 19 it is given that the ratio of the capacitance of bulk and grain boundary is correlated to the ratio of their thicknesses, expressed in Eq. 23.

$$\frac{C_B}{C_{Gb}} = \frac{t_{Gb}}{t_B} \qquad \text{Eq. 23}$$

For each grain and grain boundary a resistance and a capacitance is assigned in parallel; (RC). The different semicircles represent the summation of these elements for the bulk and grain boundary. Since all the grains, or grain boundaries, are not equal, in size nor orientation, a perfect (RC) element is hardly obtained and we will not get a perfect semicircle. In reality, the semicircles of polycrystalline materials would seem flattened. Because of this a constant phase element (CPE) is used to model this imperfect capacitor. The admittance of this element is described in Eq. 24.

$$Y_{CPE} = Q_0 \omega^n e^{in\frac{\pi}{2}} \qquad n \in [-1,1] \qquad \text{Eq. 24}$$

Q_0 is a pseudo capacitance of the material. If n is equal to 1, we get an ideal capacitor while n equal to 0 gives a pure resistor.

The capacitance of an (RQ) element is given by Eq. 25.

$$C = Y^{\frac{1}{n}} R^{\frac{1}{n}-1} \qquad \text{Eq. 25}$$

2.3.4 The Brick Layer model

In the Brick Layer model a polycrystalline material is simplified to consist of cubic grains (bulk) of thickness G, separated by both parallel and serial grain boundaries (Gb) with thickness g. This gives three distinct ways for charge carriers to move through the crystal; through the bulk, through the serial grain boundaries (⊥) and along the parallel grain boundaries (∥), see Figure 6. The charge carriers can move through the bulk or the parallel grain boundaries, but has to pass the serial grain boundary. This can be described by the circuit described in the same figure.

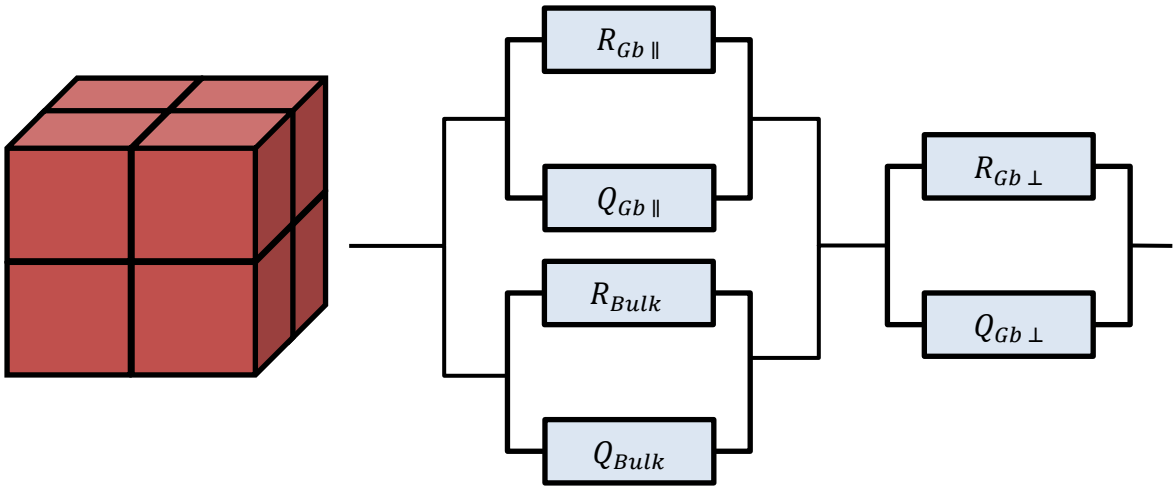

Figure 6 The Brick Layer model for a polycrystalline material on the right and the corresponding equivalent circuit on the left.

The circuit element in Figure 6 can be divided into two parts, expressed by the following equations:

$$\frac{1}{R_1} = \left(\frac{1}{R_{Bulk}} + \frac{1}{R_{Gb\parallel}}\right) = \frac{A}{L}\left(\sigma_{Bulk} + \frac{2g}{G}\sigma_{Gb\parallel}\right) \quad \text{Eq. 26}$$

$$\frac{1}{R_2} = \frac{1}{R_{Gb\perp}} = \frac{A}{L}\left(\frac{G}{g}\sigma_{Gb\perp}\right) \quad \text{Eq. 27}$$

A is the area of the sample and L is the length. If the conductivity in the bulk is much larger than the conductivity in the grain boundaries ($\sigma_{Bulk} \gg \sigma_{Gb\parallel}$) and the thickness of the bulk is much larger than the grain boundary ($G \gg g$), Eq. 26 can be simplified, and the total conductivity will be given by Eq. 28.

$$\sigma_{Tot} = \frac{1}{R_1} + \frac{1}{R_2} = \frac{1}{R_{Bulk}} + \frac{1}{R_{Gb\perp}} = \frac{A}{L}\left(\sigma_{Bulk} + \frac{g}{G}\sigma_{Gb\perp}\right) \quad \text{Eq. 28}$$

By fitting the semicircles acquired in the Nyquist-diagram, the resistances of the different parts of the sample can be determined. However, to observe two distinct semicircle, R_1 and R_2 has to be of the same order, and the characteristic frequencies has to differ.

2.4 Quantum mechanical modelling

Density functional theory (DFT) is a highly relevant method to investigate many-particle systems theoretically through first-principle calculations. Theoreticians have

used DFT to support their experimental studies, and today there are tens of thousands of scientific papers published each year. Many-particle systems can be expressed by the time-independent Schrödinger equation (Eq. 29) iteratively. [15]

$$\widehat{H}^{en}\Psi^{en}(\boldsymbol{r},\boldsymbol{R}) = E^{en}\Psi^{en}(\boldsymbol{r},\boldsymbol{R}) \qquad \text{Eq. 29}$$

$\widehat{H}^{en}$ is the Hamiltonian operator of the many-particle equation, E^{en} is the total energy of the system, $\Psi^{en}(\boldsymbol{r},\boldsymbol{R})$ is the wavefunction of the electrons and nuclei. The **r** and **R** are the coordinates of the electrons and nuclei, respectively. By applying the Born-Oppenheimer approximation, the full wavefunction is divided into an electronic part and a nuclear part:

$$\Psi^{en}(\boldsymbol{r},\boldsymbol{R}) \approx \Psi(\boldsymbol{r}) \cdot \Theta(\boldsymbol{R}) \qquad \text{Eq. 30}$$

The two mathematical theorems that set the fundamentals for density functional theory were proven by Kohn and Hohenberg. They are as follows: 1) The ground-state energy from Schrödinger's equation is a unique functional of the electron density, and 2) the electron density that minimizes the energy of the overall functional is the true electron density corresponding to the full solution of the Schrödinger equation. As a result of these theorems, we can find the ground-state energy by iteratively minimizing the energy with respect to the density with DFT. The electron density is given by Eq. 31.

$$n(\boldsymbol{r}) = 2\sum_i \psi_i^*(\boldsymbol{r})\,\psi_i(\boldsymbol{r}) \qquad \text{Eq. 31}$$

By using the Kohn-Sham equations (Eq. 32) we can express the electron density by solving a set of equations involving only single electrons.

$$\left[-\frac{\hbar^2}{2m}\nabla^2 + V(\boldsymbol{r}) + V_H(\boldsymbol{r}) + V_{XC}(\boldsymbol{r})\right]\psi_i(\boldsymbol{r}) = \varepsilon_i\psi_i(\boldsymbol{r}) \qquad \text{Eq. 32}$$

The first term on the left-hand side is the kinetic energy, the second term is the interaction potential between the collection of atomic nuclei and the electron, V_H is the Hartree potential and describes the electron-electron interaction, V_{XC} is the "functional derivative" of the exchange-correlation energy with respect to electron density. The exchange-correlation energy term include all the quantum mechanical effects that are not included in the former terms. $\psi_i(\boldsymbol{r})$ is the single-electron wave

functions, and in a periodical structures, this wavefunction can be expressed by using Bloch's theorem as a product of $u_i(\mathbf{r})$, which has the same periodicity as the supercell, and a plane wave, $e^{i\mathbf{kr}}$.

$$\psi_i(\boldsymbol{r}) = u_i(\boldsymbol{r})e^{i\boldsymbol{kr}} = \left(\sum_{\boldsymbol{G}} c_{i,\boldsymbol{G}}\, e^{i\boldsymbol{Gr}}\right)e^{i\boldsymbol{kr}} = \sum_{\boldsymbol{G}} c_{i,\boldsymbol{G}}\, e^{i(\boldsymbol{k}+\boldsymbol{G})\boldsymbol{r}} \quad \text{Eq. 33}$$

As seen in Eq. 33, $u_i(\mathbf{r})$ has been expressed by a set of plane waves where **G** is all sets of vectors in reciprocal space. By exploiting the fact that wave functions at k-points in close proximity are rather similar, one needs only to consider a finite number of k-points in the first Brillouin zone. The wave functions expressed in Eq. 33 are solutions of the Schrödinger equation with the following kinetic energy:

$$E = \frac{\hbar^2}{2m}|\boldsymbol{k} + \boldsymbol{G}|^2 \quad \text{Eq. 34}$$

Solutions with lower energies are more physically important, thus only solutions with kinetic energy below a chosen value, E_{cut}, the cut-of energy, are included:

$$E_{cut} = \frac{\hbar^2}{2m}G_{cut}^2 \quad \text{Eq. 35}$$

DFT works by defining an initial electron density $n(\mathbf{r})$ and using this to find the single-electron wave functions, $\psi_i(\boldsymbol{r})$, by solving the Kohn-Sham equations. With the single-electron wave functions, a new electron density is calculated using the Kohn-Sham equations. If the two densities are similar, the ground-state electron density is found. If the densities are dissimilar, the trial density is updated.

2.4.1 Exchange-correlation functional

One of the major obstacles with DFT is that the exchange and correlation interactions cannot be expressed as exact functionals, with the exception of free electron gas. Hence, approximations and simplifications are made. The exchange and correlation part are often expressed together in an exchange-correlation part, E_{XC}. However, using these approximations will not solve the true Schrödinger equation.

The local density approximation (LDA) and GGA are the most basic of the exchange-correlation functionals. In LDA the electron density is constant at all points in space and the exchange-correlation is a functional of this electron density. However, in a

solid the electron density is never constant, as chemical bonds are essentially variations in electron density. GGA uses information about the local electron density as well as the local gradient. Within GGA there are a lot of different functionals, *e.g.* the Perdew-Wang functional (PW91) and the Perdew-Burke-Ernzerhof functional (PBE), which is used in this thesis. [15]

These functionals are quite useful at comparing different structures. However they are known to underestimate the band gap in insulators and semi-conductors and they do not take into account van der Waals forces.

3. Literature

Langatate is a fairly new material and there has been some work done to investigate its properties. The most relevant results will be presented in this chapter. In literature both the terms 'LGT' and 'LTG' are used as abbreviations for langatate. In this thesis, only LGT will be used to describe langatate.

3.1 Crystal structure and composition

The structural parameters of langatate have been studied in some extent. PDF data from Pavlovska *et al.* [16] reports values of a = 8.213 Å and c = 5.167 Å with the space group P321.

Kaurova *et al.* studied two single crystals of langatate grown by the Czochralski process, pulled along the Z-axis, with X-ray (XRD) and neutron diffraction (ND). The crystals were examined before and after post-growth annealing in air and vacuum. Values of a and c in the range of 8.227 – 8.236 Å and 5.123 – 5.129 Å, respectively, were reported. They investigated the relationship of structural parameters and composition and have shown that the cell parameters show a slight dependency on both the level of vacancies on the cation and anion sites and the ratio of Ga and Ta on the 1a site [3]. As can be seen from Figure 7 (left) the cell parameter, a, increases as the Ga/Ta ratio decreases. From refinement of their XRD and ND data they showed that cation vacancies occur at the 3e lanthanum site. Lanthanum vacancies were shown in other papers as well, in both gallium rich and tantalum rich samples [17]. Gallium vacancies in site 2d were reported as well in tantalum rich samples.

Kuzmicheva *et al.* also came to the conclusion the growth conditions influence the composition of the crystal. According to their XRD data, crystals treated in vacuum had tantalum ions occupying both the 2d gallium site (as Ta^{3+}) as well as the 1a octahedral site (Ta^{5+}) [18]. For the crystal treated in air tantalum ions only occupied the 1a site. Tantalum existing in the charge state of 3+ in langatate was not confirmed by any other publications however.

Both Kaurova and Kuzmicheva examined the relationship of the colour of the single crystals and their composition [3, 17]. They observed that the colour of the crystal

depended on the growth atmosphere and the post growth treatment, and this was attributed to the concentration of oxygen vacancies. On the right of Figure 7 this relationship is shown. Kaurova discusses this in his paper that the cause of this might be similar to the colouration of langasite. This was attributed to the association of an oxygen vacancy and localized electron(s); $(v_O^{n\bullet}, ne')^x$. The crystals grown by Kuzmicheva in argon and air atmospheres were almost colourless while the crystals grown in atmospheres with higher oxygen partial pressures were bright orange. According to ND data the coloured crystal had vacancies at the 3e lanthanum site and a smaller Ga/Ta ratio compared with the colourless crystal. The coloured crystal had less oxygen vacancies as well. It was concluded that the colorization was related to the oxygen vacancy content. However the exact mechanism was not reported. Georgescu *et al.* synthesized Eu-doped langatate, $(La_{0.97}Eu_{0.03})_3Ga_{5.5}Ta_{0.5}O_{14}$, which was coloured slightly red. It was reported that the colourization was related to oxygen defects (vacancies and interstitials) influenced by the growth atmospheres. [19]

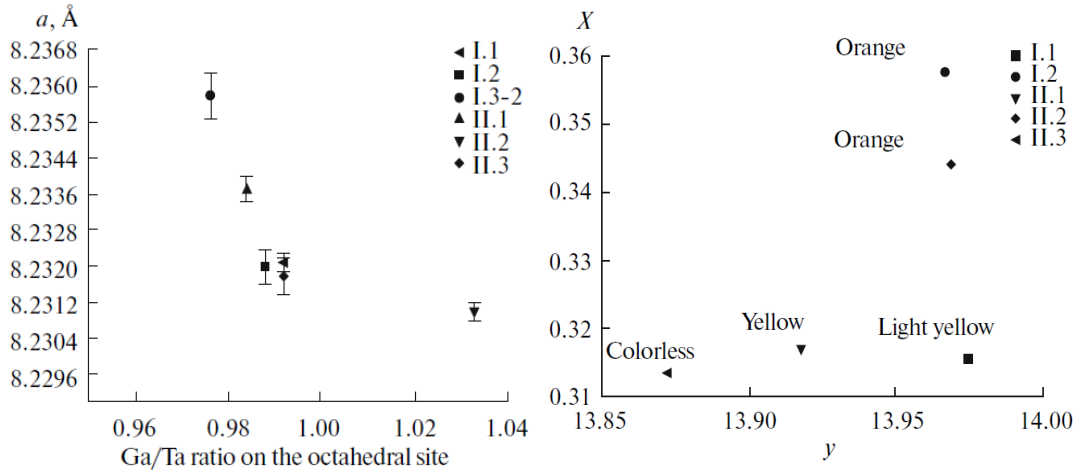

Figure 7 On the right figure the cell parameter, a, as a function of the Ga/Ta ratio on the 1a site is displayed. On the left the relationship of the colour, here displayed as the red component X, and oxygen content in langatate, $La_3Ta_{0.5}Ga_{5.5}O_y$, from neutron diffraction. The points mark the different samples Kaurova *et al.* measured on. [3]

3.2 Materials properties

Sehirlioglu *et al.* reported that the dielectric constant of langatate along x- and y-axis (which is 30° off the crystallographic y/x-axis) did not show any significant temperature dependencies up to 600 °C. They measured this value at two different

temperatures and at 30 °C they got $K_{33} \approx 21$ and 27 while at 600 °C they got $K_{33} \approx 23$ and 31, respectively. [1] However along the z-axis the dielectric constant was $K_{33} \approx 84$ and this had a greater temperature dependency This is approximately the same value reported by Axtal; $K_{33} \approx 80$ at 1MHz. [20]

3.3 Electrical transport properties

Sehirlioglu *et al.* investigated the electrical transport properties of single crystals of langatate cut in different directions; in the crystallographic x and z directions, and in a direction 30° of the crystallographic y direction in the xy-plane. [1] They measured the resistivity of the crystal from room temperature up to 600 °C, and reported activation energies for the different directions; 0.35 eV in the x and z directions, and 0.43 eV for the "30° of the y" direction. Figure 8 shows the constant frequency measurements performed in the different directions on the LGT single crystal. The frequency is not reported. On the right side of Figure 8, a picture of the crystal is displayed. Note that the crystal is colourless. They could not conclude the exact mechanism of conductivity.

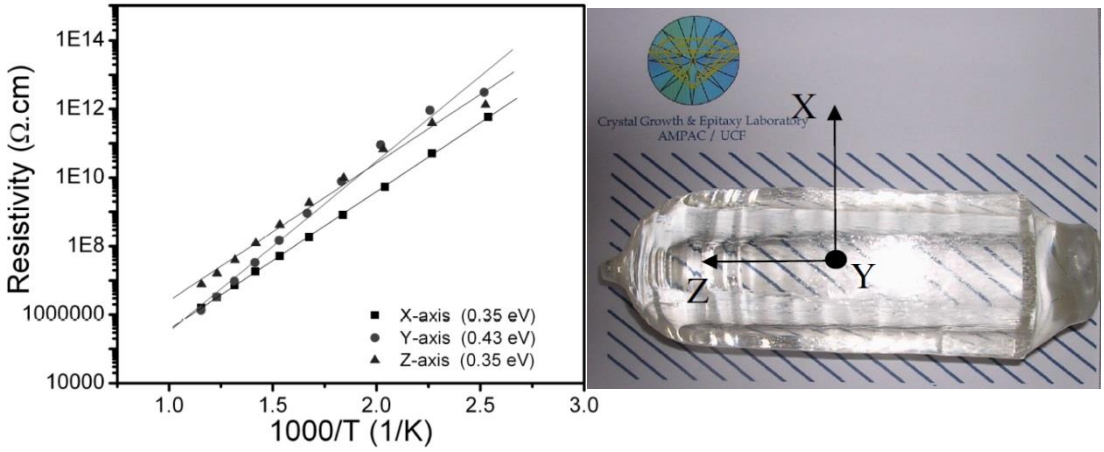

Figure 8 Constant frequency measurements by Alp Sehirlioglu *et al.* [1] of LGT single crystal measured along the different directions. Note that the graph labelled as the "Y-axis" is not equal to the crystallographic y-axis, but has a 30° offset from the y-axis in the xy-plane. On the right, the measured sample.

Electrical measurements were also performed by Davulis and Pereira da Cunha, from room temperature up to 900 °C, who reported significantly higher activation energies of 1.02 and 0.97 eV in the x and z directions, respectively. Frequency of the

measurements is not reported [21]. In another paper, they reported values of 1.04 and 0.95 eV, respectively for frequencies below 100 MHz [22].

There has been no work on the presence of protons in langatate. However there has been some work on langasite. Fritze *et al.* performed impedance measurements with varying pH_2O and reported a significant contribution from protons to the conductivity. [2] Figure 9 displays the pH_2O dependency on single crystalline langasite cut in z- and y-directions at both 800 °C and 600 °C. A dependency of approximately $p_{H_2O}^{1/2}$ is observed for the z-cut single crystal at 800 °C.

Bjørheim *et al.* [5] did electrical measurements on nominally undoped Y-cut single crystalline langasite, as well as polycrystalline 1 and 6 mol% Sr doped langasite. Standard hydration enthalpy and entropy of -120±8 kJ/mol and -148±12 J/molK, respectively, were reported for the Y-cut langasite. For the 6 mol% Sr doped polycrystalline values of -112±5 kJ/mol and -140±8 J/molK were reported for standard hydration enthalpy and entropy, respectively. Enthalpy of mobility for the oxide ion was calculated to be 100±2 kJ/mol for all of the samples, while for the proton this was 78±4 kJ/mol. It was concluded that all these samples were effectively acceptor doped and dominated by protons and oxygen vacancies, and that langasite was a modest proton conductor.

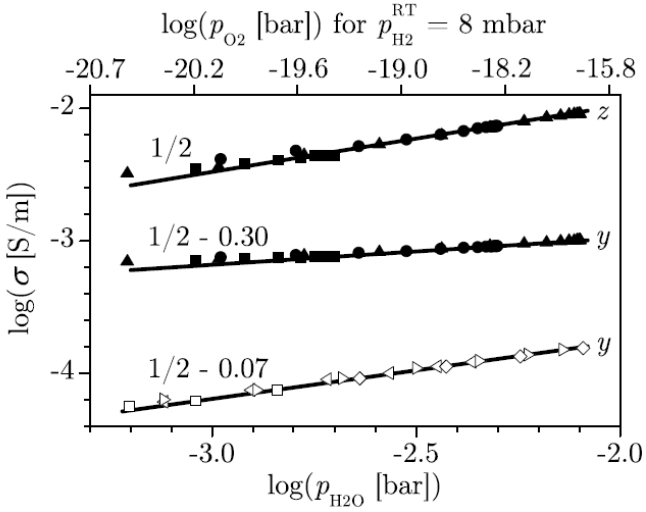

Figure 9 Impedance measurements with varying pH_2O performed on single crystal langasite cut in z- and y-directions at 800 °C (solid points) and 600 °C (open points). Figure from [2]

3.4 DFT calculations

Chung *et al.* did comprehensive work with DFT on langatate. They obtained optimal cell parameters of a=8.222 Å and 2c= 10.273 Å working with a 1x1x2 supercell with the Ta-atoms in the corners of the supercell in the 1a site. [23] The band gap was calculated using different potentials, and they got values of 3.64 eV with (PBE) GGA and 5.28 eV with the HSE06 hybrid functional.

According to their calculations of the partial density of states, the valence band maxima (VBM) originates from the 2p orbitals of the oxygen atoms while the conduction band minima (CBM) has its origin from the orbitals of both the gallium 5s and the tantalum 5d. Different acceptor-like defects were examined in their work in a 2x2x1 supercell, and it was concluded that under oxygen rich atmosphere the most energetically stable defects were Ga''_{Ta} and $v^{5\prime}_{Ta}$ at low and high Fermi level, respectively. DFT calculations on oxygen vacancies using the GW approximation were also done. It was concluded that the oxygen vacancy located at the 6g site was the most stable and this could determine the properties of langatate. [24] Formation energies of oxygen vacancies at the 6g and 2d site as a function of Fermi level are shown in Figure 10, and it can be seen that the singly charged oxygen vacancy is never stable.

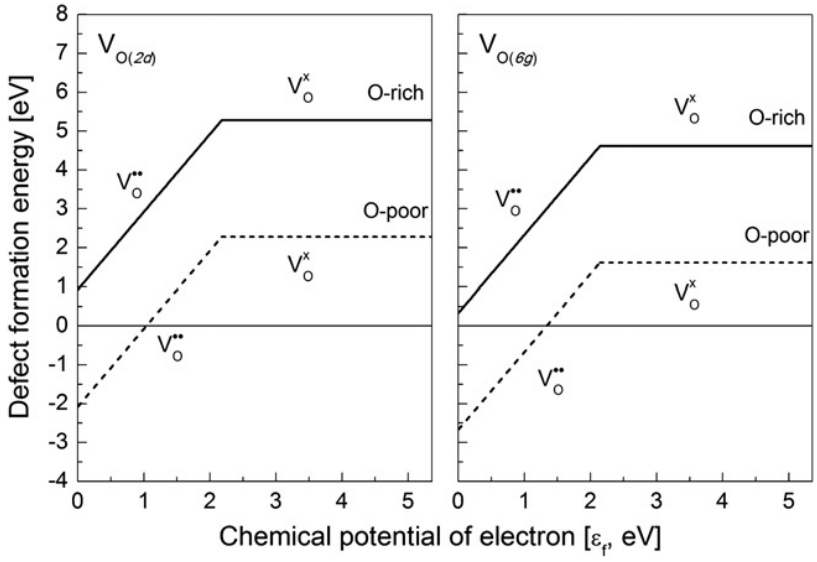

Figure 10 Formation energies of oxygen vacancy at the 2d and 6g sites in oxygen rich and poor conditions. Figure from [24].

Chung *et al.* also investigated the piezoelectric effect with density functional perturbation theory (DFPT) using both GGA-PBE and HSE06 XC-functionals. It was reported that the piezoelectric coefficients, e_{11} and e_{14}, increased with increasing bond lengths to oxygen with the 1a and 3e cation sites and decreasing bond lengths with the 2d and 3f cation sites. [25] It was proposed in their paper to substitute a larger ion for the La^{3+} and substitute a smaller ion for the two tetrahedral Ga^{3+} ions for an increase of the piezoelectric coefficients.

There has been no DFT study on protons in langatate, however, Bjørheim *et al.* [5] have done calculations on protons in langasite. Hydration enthalpy for the absorption of protons from water was calculated to 0.87 eV for the following reaction:

$$H_2O(g) + 2O_O^x = OH_O^\bullet + OH_i' \qquad \text{Eq. 36}$$

Mobility enthalpy of 0.7 eV was calculated for oxygen interstitial in langasite in the same study through the Nudged Elastic Band (NEB) method, which is used in DFT calculations to find the minimum energy path of diffusing species.

4. Experimental

This chapter describes the details of the synthesis of the polycrystalline langatate and the subsequent structural, compositional and electrical characterization. A short introduction of the equipment used and the methods will be given.

4.1 Synthesis

In this thesis polycrystalline langatate of two different compositions were made; undoped and acceptor-doped langatate with the nominal compositions $La_3Ta_{0.5}Ga_5O_{14}$ and $La_3Ta_{0.475}Ga_{5.525}O_{14-y}$. The gallium will substitute for the tantalum ions and form effectively negative acceptor defects, Ga''_{Ta}. In this thesis an acceptor concentration of 2.5 mol% was chosen. This gives a Ga/Ta ratio of approximately 1.1 on the 1a site. All the samples were made through solid state synthesis. In Table 2 the different compounds used in the synthesis of the undoped and acceptor-doped langatate are displayed.

Table 2 Components for synthesis of undoped and acceptor-doped langatate.

Name	**Chemical formula**	**Purity**	**Distributor**
Lanthanum(III)oxide	La_2O_3	99.99%	Sigma-Aldrich
Gallium(III)oxide	Ga_2O_3	99.999%	Alfa Aesar
Tantalum(V)oxide	Ta_2O_5	99.99%	Sigma-Aldrich

4.1.1 Undoped langatate

The first step of the synthesis process was drying lanthanum oxide since the substance is known to be very hygroscopic, *i.e.* absorbs water. The furnace was heated up from room temperature to 900 °C with a gradient of 400 °C/hour. It was kept at 900 °C for half an hour then cooled down to 600 °C. The oxide was taken out at this temperature and immediately weighed to get the relative amount.

Following the drying, stoichiometric amounts of the oxides were weighed and mixed by ball milling using an agate crucible and balls for 1 hour with 250 rpm with isopropanol as solvent. After the milling the powders where dried in a heating cabinet.

The dried powders were cold-pressed to 13 mm pellets under a uniaxial pressure of 74 MPa. The pellets were subsequently calcinated in air according to the temperature profile shown in Figure 11.

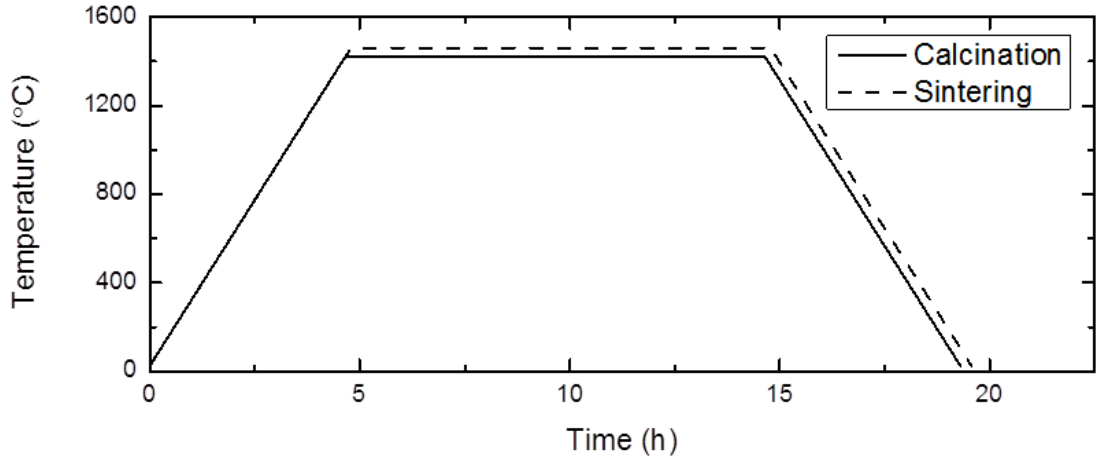

Figure 11 Calcination and sintering of the undoped langatate with a peak temperature of 1420 °C and 1460 °C, respectively, and gradient of 300 °C/hour.

From room temperature the furnace was heated up to 1420 °C with a gradient of 300 °C/hour. It dwelled at that temperature for 10 hours then cooled down with the same cooling rate back to room temperature. The pellet was crushed to a powder and repressed with a uniaxial pressure of 151 MPa. The new pellet was sintered in air with the temperature profile shown in Figure 11. The densities of the pellet before and after sintering are shown in the Table 3.

Table 3 Dimensions and densities of the pellet before and after sintering with the theoretical densities of langatate listed as well. [26]

	h (mm)	**d (mm)**	**m (g)**	ρ_e (g/cm^3)	ρ_t (g/cm^3)	ρ_e/ρ_t
Before	3.23	13.0	1.816	4.24	6.15	69 %
After	3.11	11.9	1.811	5.21	6.15	85 %

X-ray diffraction was performed on this pellet after it had been polished on the surfaces to get rid of impurities.

Platinum paint with flux (Metalor Technologies Ltd, 8082 Pt paste) was painted on in a circular shape with several layers on both sides of the pellet. A drying phase of 20

minutes followed after each layer. Platinum net was attached (see Figure 12). After these procedures the pellet was heated up in the oven to 850 °C with a gradient of 200 °C/hour. It was dwelled at the peak temperature for 2 hours before cooling down with the same, but negative, gradient back to room temperature.

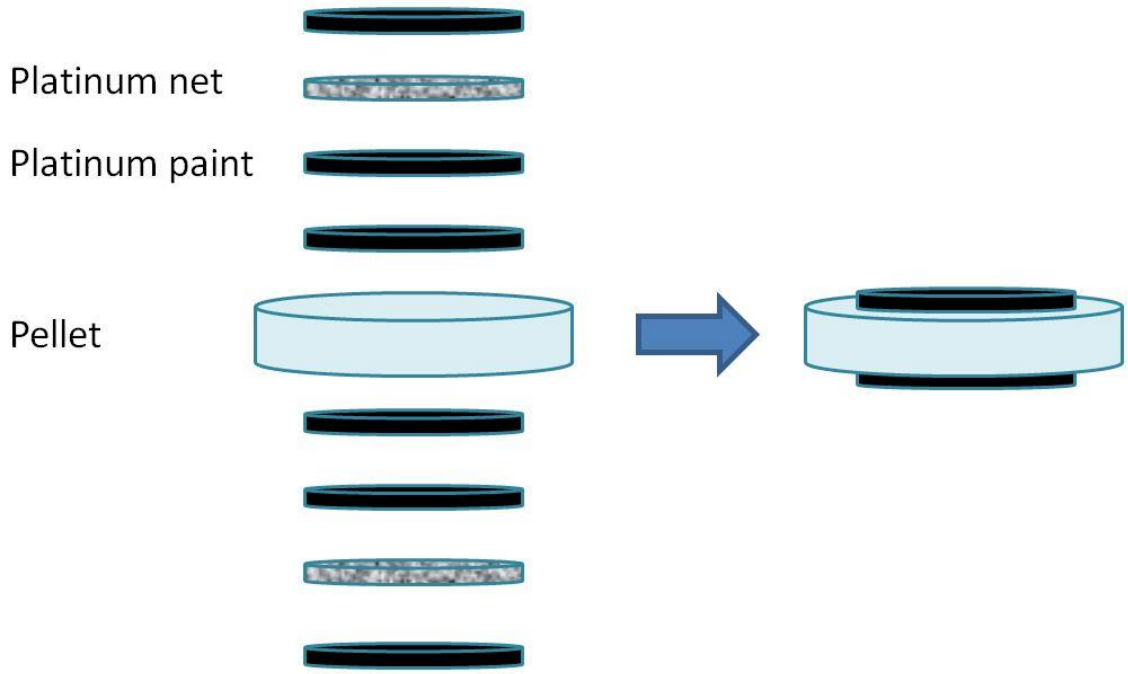

Figure 12 The different layers on the pellet that was prepared to be measured with impedance spectroscopy.

4.1.2 Acceptor-doped langatate

An acceptor-doped langatate sample was made. This material was doped with 2.5 mol% gallium. The same synthesis route as for the undoped langatate was followed.

Chemical formula: $La_3Ta_{0.5-x}Ga_{5.5+x}O_{14-x}$ $x = 0.025$

Table 4 Dimensions and densities of the pellet after calcination and sintering with the experimental and theoretical densities of (undoped) langatate listed as well. [26]

	h (mm)	**d (mm)**	**m (g)**	ρ_e (g/cm^3)	ρ_t (g/cm^3)	ρ_e/ρ_t
Calc.	2.56	10.3	1.271	5.97	6.15	97 %
Sint.	2.76	11.7	1.664	5.65	6.15	92 %

Platinum paint was painted on the sintered pellet and platinum net was added following the same procedures as those done on the undoped pellet with the same temperature profile for drying and burning.

4.1.3 Single crystal langatate

Six pieces of single crystal langatate were obtained from Axtal GmbH & Co. The dimensions of all pieces were 10x10x0.25 mm. There were 3 pairs of pieces, where each pair was labeled X-, Y- and Z-cut. XRD was performed on these samples to confirm the directions. The weight of each piece was 0.1543 g which gives a density of 6.17 g/cm^3.

These crystals were grown by Czochralski method using Ir crucible under an atmosphere of nitrogen with 1 volume% O_2.[1]

Platinum paint was painted on and platinum net was attached. The same procedures as described in the section above on polycrystalline langatate were followed.

4.2 Characterization

The methods of characterization of the samples will be looked upon. There are two main methods that are used in this work; X-ray diffraction (XRD) to see the crystal structure of the samples and scanning electron microscope (SEM) to look at the microstructure. Ultraviolet-visible-near infrared spectrophotometer (UV-VIS-NIR) is utilized as well to investigate the bandgap. A short introduction to the apparatus will be given.

4.2.1 X-ray diffraction

The X-ray diffractometer used was of the model D8 by Bruker. It has a Cu-K-α X-ray source. The software EVA by the same manufacturers was used to analyse the X-ray diffraction (XRD) spectrum. XRD was performed on the various samples at different stages of synthesis.

1 This information was inquired by Axtal as it was not specified in the documents following the acquisition.

4.2.2 Scanning Electron Microscopy

To investigate the compositions of the samples a tabletop scanning electron microscope (SEM) was used of the model Hitachi TM3000 Tabletop Microscope. It has two main image modes; topographical and compositional mode. The last mode takes use of the built in Energy-dispersive X-ray spectroscopy (EDS) of the model Quantax70. The software used was the corresponding software which followed with the SEM, TM3000.

4.2.3 Ultraviolet-visible-near infrared spectrophotometry

By using the UV-VIS-NIR spectrophotometer, light at various wavelengths is directed toward the sample, and we can measure both the light that goes through the sample, the transmittance, T, and the light that reflects of the surfaces, the reflectance, R. By measuring both, the absorbance of the material, A, can be calculated through Eq. 37.

$$1 = T + R + A \qquad \text{Eq. 37}$$

In this experiment a Shimadzu UV-3600 spectrophotometer was used with the UV Probe 2.33 software package. Electromagnetic waves of the length 850 – 200 nm were used to analyse the sample. The single crystal Y-cut sample was measured on.

This method allows for qualitative determination of the bandgap of the material. However this is only the case if the dominant mechanism of absorption is bandgap excitation.

4.3 Impedance measurements

All electrical characterizations were performed in a ProboStat measurement (Figure 13) manufactured by NorECs. The Probostat consists of an alumina support tube and a spring-loaded alumina ring. The cell is sealed by an outer quartz tube and O-ring, which allows accurate atmosphere control. There are two gas tube inlets, inner and outer, which purpose is to create an atmospheric gradient. This was however not used in this thesis. There are also two gas tube outlets. Electrodes are connected to the sample, through the inside or outside of the support tube, and finally a thermoelement

is located outside the support tube, at the same height of the sample. All electrical contacts are made of Pt.

The Probostat is connected via a switch to an impedance spectrometer; in this case a Solartron SI 1260 Impedance/ Gain-phase analyser. This impedance meter has a frequency range of 10 μHz to 32 MHz, and can measure resistance and capacitance in the range of 10 mΩ to 100 MΩ and 1 pF to 10 MF, respectively, with a 5 digit resolution.

Both of the polycrystalline samples were measured with a "2 point – 4 wires"-setup, while the single crystals were measured in a "sandwich", *i.e.* at the same time, with a "2 point - 2 wires"- setup. The advantage of this is that we can measure on two samples at a time, but the downside is that "2 point – 2 wires"-setup introduces the resistance of the electrode as well, as opposed to "2 point – 4 wires" –setup.

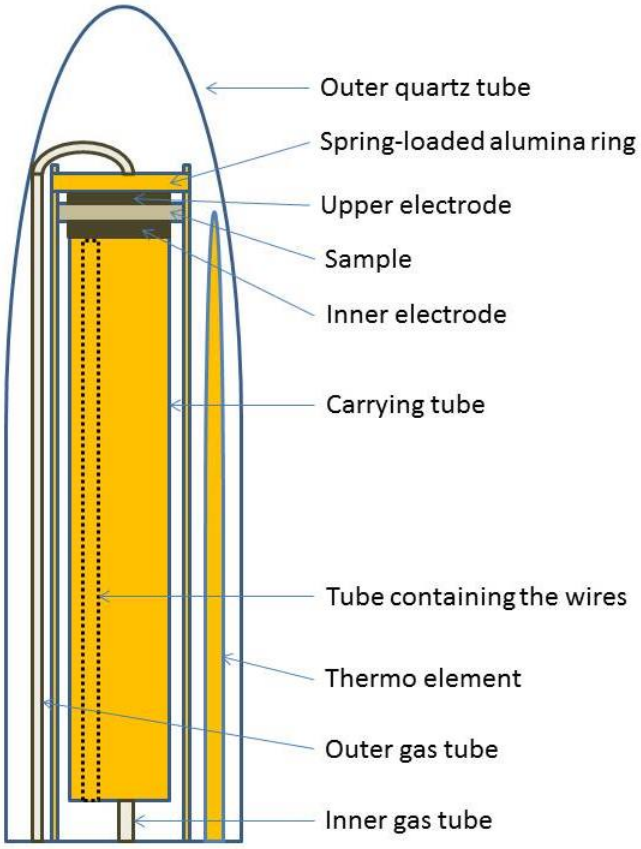

Figure 13 The ProboStat with the different parts displayed schematically.

4.3.1 Impedance spectroscopy

Impedance spectroscopy were done on all of the samples used in this thesis; the undoped LGT, the 2.5 mol% Ga-doped LGT (LGT2.5) and the X- and Z-cut single crystals. A frequency range of 1 MHz to 1 Hz was used. These measurements were done at constant temperature and atmosphere, and started after equilibrium was reached.

For the deconvolution of the impedance spectra the Windows-based program "Equivalent Circuit" (EQC, version 1.2) was used written by Bernard A. Boukamp from the Faculty of Chemical Technology, University of Twente.

All the impedance spectra were deconvoluted by subtracting a parallel stray capacitance of $1 \cdot 10^{-12}$ F/cm due to the experimental setup.

4.3.2 Constant frequency measurement

Constant frequency measurements (ramps) were performed on all the samples used in this thesis with the exception of the Y-cut single crystal langatate. The frequency and oscillation voltage differs from the samples; 32 kHz and 0.5 V was used for the undoped LGT; 10 kHz and 0.1 V for the acceptor doped LGT and the single crystals. The frequencies were chosen according to the impedance spectra; the measured frequencies were in the bulk region at most temperatures for both materials. Ramps were performed in varying atmospheres in the temperature range 1200 – 400 °C with a cooling rate of -0.2 °C / min.

Tablecurve 2D version 5.01 by Systat was used to fit the curves obtained from the constant frequency measurements.

4.3.3 Gas mixer

Figure 14 displays the gas mixer used in this thesis. The main purpose of using this device is to have different mixtures of gas in the measuring cell in a controlled manner. By mixing two gases in different ratios, one can easily control the partial pressures of the gases. As can be seen from the figure, there are three mixing stages (M1 – M3) which allows multiple levels of thinning the gas.

By mixing oxygen gas with argon and adjusting the flows of the two gases and the flow of the mixtures, the partial pressure of oxygen can be controlled. This allowed measurements in oxygen partial pressures of 1 to 10^{-5} atm (pO_2 measurements). By using hydrogen gas instead of oxygen, measurements were done in reducing atmospheres as well.

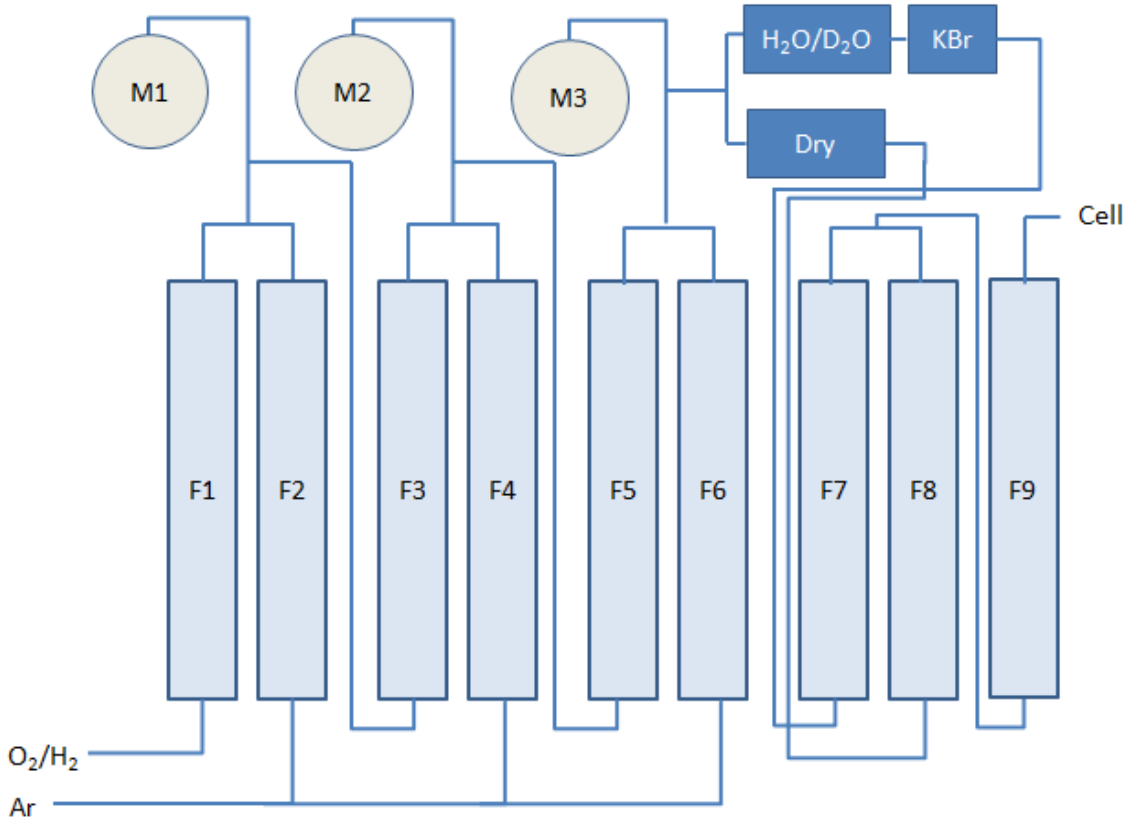

Figure 14 The gas mixer used in this thesis. F1-F9 are the flow meters, M1-M3 designates the bubbling element for the different mixes.

pH_2O measurements were done by adjusting the flow of the gas passing through the wetting stage and the drying stage. This made it possible to do measurements in water vapour pressure from approximately $2.7 \cdot 10^{-2}$ (only passing it through the wetting stage) to $3 \cdot 10^{-5}$ atm (only passing it through the drying stage). The drying stage consists of P_2O_5. The gas passing through the wetting stage is passed through KBr. The reason for this is to inhibit the condensation of water in the pipes before it reaches the measuring cell.

In Table 5 the partial pressures for oxygen and water vapour for the different terms used in this thesis. These values were calculated from the "Gasmix" program (version 0.5) developed by Truls Norby (University of Oslo) and NorECs. The differences in partial pressures at different temperatures are insignificant.

Table 5 The partial pressure of oxygen and water vapour at the different atmospheres in a Probostat cell.

Partial pressure	pO_2	pH_2O
Wet oxygen	9.73E-01	2.66E-02
Dry oxygen	1.00E+00	3.00E-05
Wet argon	~E-05	~E-02
Dry argon	~E-05	~E-05

4.4 Errors and uncertainties

The uncertainties associated with the measuring setup have not been calculated. However uncertainties are to be expected in the various stages. The most significant areas of errors are mentioned in this subchapter.

The measured dimensions of the pellets differ in their uncertainty for the two polycrystalline samples. While the thickness of the samples are quite accurate, since the samples are simple pellets, the electrode diameters are not quite so. The platinum electrode was painted on with a brush with the aim of a circle shape. However the shape was not a perfect circle, and therefore the true resistivity calculated from the resistance will have a small uncertainty.

Other factors that give a slightly different material resistivity are the amount of pores in the sample. Since the measured densities of the pellets are not equal to the theoretical density, pores are expected. Secondary phases in the samples can also give an incorrect material resistivity for langatate as well as an incorrect density if the amount is high. This will in turn affect the amount of dopants in the material.

From the impedance setup, there is expected to be some leakage of gas in the joints of the copper piping. Although this has somewhat been corrected for in the calculations of the partial pressures, this would lead to some small uncertainties in the pO_2 and pH_2O measurements, especially in the lower regions of these partial pressures. We have to remember that in dry atmospheres and in argon, the pH_2O and pO_2, respectively, are not well defined.

5. Computational methodology

From the ICSD crystal database a langatate crystal structure was chosen with the ICSD number 94710. All supercells used in these calculations are derived from this structural data, *i.e.* the initial cell parameters for the supercells before relaxation are multiples of the parameters listed in Table 6.

Table 6 Structural parameters of the input langatate cell for the DFT calculations. [16]

Formula	$La_3Ta_{0.5}Ga_{5.5}O_{14}$		
Origin	ICSD-94710		
Authors	Pavlovska, A.; Werber, S.; Maximov, B.; Mill, B.		
Publication title	Pressure-induced phase transitions of piezoelectric single crystals from the langasite family		
Space group	P 3 2 1 (150) - trigonal		
Cell	a = 8.213(4) Å	c = 5.167(3) Å	c/a = 0.6291

A single formula unit of langatate has a fractional number of atoms (0.5 Ta and 5.5 Ga), and for the DFT-calculations one can only work with integer numbers of atoms in the cell. Thus, a supercell was defined so whole atoms could be used. In this thesis two supercell sizes were used; a 1x1x2 and a 2x2x4 supercell (see Table 7 and Figure 15). A large supercell is beneficial in the calculations of defects. The reason for this is to minimize the defect-defect interactions in the periodically repeated cell. Introducing one point defect in the 1x1x2 and the 2x2x4 supercells defect concentrations of ½ and 1/16, respectively, per oxide is obtained. Ideally we want the supercell as large as possible to get infinite dilution and a big periodic separation of the defect, and thus minimizing the contribution to the total energy from the defect-defect interaction. Due to limited computational resources larger supercells were avoided in this thesis.

Table 7 The two different supercell sizes used in the DFT calculations with the number of formula units, Z, in the cell and total number of atoms, N.

	1x1x1	**1x1x2**	**2x2x4**
	$\boldsymbol{La_3Ta_{0.5}Ga_{5.5}O_{14}}$	$\boldsymbol{La_6TaGa_{11}O_{28}}$	$\boldsymbol{La_{48}Ta_8Ga_{88}O_{224}}$
Z	1	2	16
N	23	46	368

Prior to any defect calculations, convergence tests with respect to various computational parameters were performed in order to reduce the error from the method itself. A convergence test was done with respect to the k-point density and the energy cut-of. In addition, two different exchange-correlation functionals, LDA and (PBE) GGA were utilized.

An initial supercell configuration was defined with the disordered cations on site 1a defined to specific positions as seen on the right hand side of Figure 15. This 1x1x2 supercell along with the corresponding 2x2x4 supercell was used for the calculations in this chapter.

Pseudo potentials were used for La, Ta and Ga, with valence electrons of 11, 5 and 3, respectively. For unit cells with odd numbers of electrons, *e.g.* calculations of OH_O^x and $v_O^\bullet$, spin polarization were accounted for in the calculations.

All calculations were relaxed with the following criteria; electronic relaxation with total energy difference less than 10^{-6} eV from the previous iteration and ionic relaxation with forces on each atom less than 0.02 eV/Å. For all of the calculations the (PBE) GGA exchange-correlation functional was used, with the exception of the XC-functional test.

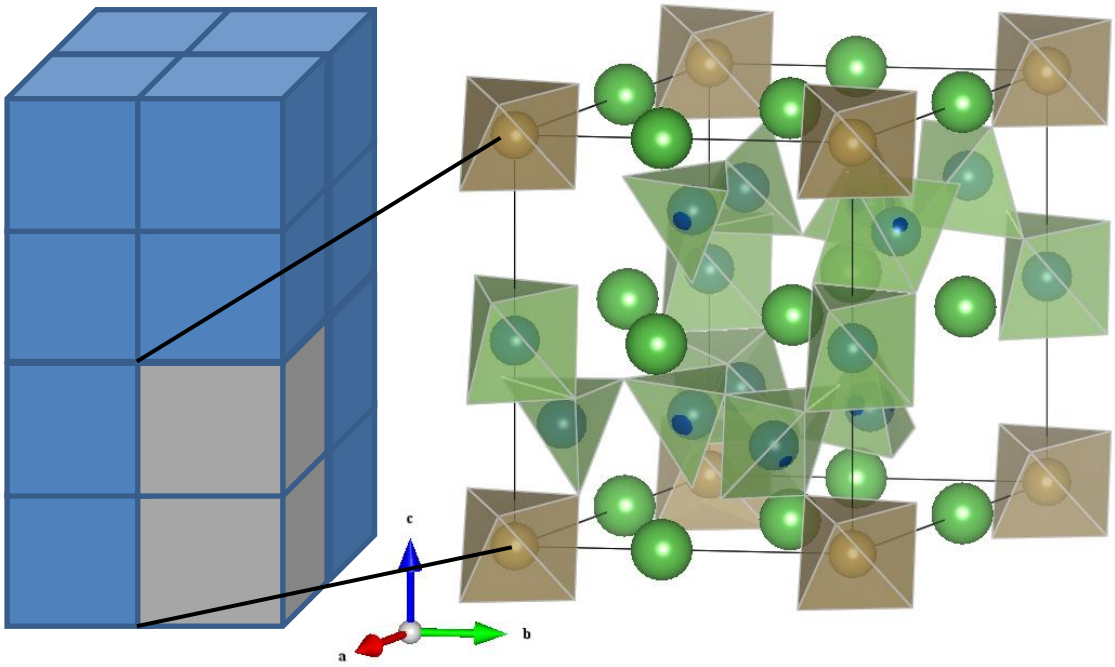

Figure 15 On the left we see the construction of the 2x2x4 supercell. Each cube represents a unit cell langatate. The grey section represents the 1x1x2 supercell. On the right, we see the 1x1x2 supercell with tantalum (brown) in the 1a sites in the corners, gallium (blue) in the remaining 1a sites and in the 2d and 3f sites, and lanthanum (green) in the 3e sites.

5.1 Vienna Ab initio Simulation Package

The Vienna Ab initio Simulation Package (VASP) is a computer software package which is used to model materials on an atomic level from first principles. Only a rough description of the most essential VASP-files is given. For further detailed information, the reader is referred to literature. [27]

Input files

- **POSCAR** This file contains all the information about the crystal structure and the contained atoms. Basically, it contains a unit cell (supercell).
- **INCAR** This file has all the parameters for the calculation itself, mainly for the electronic and ionic relaxation steps. Here it is specified how many iterations there will be done, what type of algorithm to use, and what value satisfies the energy minimization needs. A lot of tweaking can be done in this file.
- **POTCAR** The potentials of the atoms defined in POSCAR is specified in this file.
- **KPOINTS** This file specifies the number of k-point to be used for the calculations, in x-, y- and z-directions.

Output files

- **CONTCAR** This file is like POSCAR; however it contains the new positions of the atoms after the calculations have ended. It also contains forces in all directions on all of the atoms.
- **OUTCAR** This file contains all the important information about our system; all the parameters used from the input files, potentials, k-point density, and the total energy as the most important.
- **DOSCAR** The density of states (DOS) and the integrated DOS are contained in this file in units of "number of states/unit cell". From DOSCAR, the partial DOS of each atoms in the unit cell can be derived, which in turn contains the DOS of the atoms s-, p- and d-orbitals.

5.2 Method of calculation

In this thesis, the calculations on defects will be on isolated defects, *i.e.* supercells with only one defect at a time. This leads to the charge balance not being upheld. AS a result, a compensating background charge is introduced which leads to electrostatic interactions with the defects in the supercell. However the potential of ions in the perfect defect free supercell was compared with the potential of ions in a supercell containing defects. The difference was insignificant.

5.3 Convergence

Figure 16 (left) displays the total energy per formula unit Z of the 1x1x2 supercell as a function of the plane wave cut-off energy. At 500 eV, the total energy is converged within 30 meV with respect to cut-off energy of 550 eV. All further calculations are performed with cut-off energy of 500 eV.

In Figure 16 (right) the total energies per formula unit Z of both the 1x1x2 and 2x2x4 supercells as a function of k-points are displayed. The 1x1x2 supercell was examined for a bigger k-point range. Only k-points of 1x1x1 and 2x2x2 were tested for the bigger supercell due to limited computational resources.

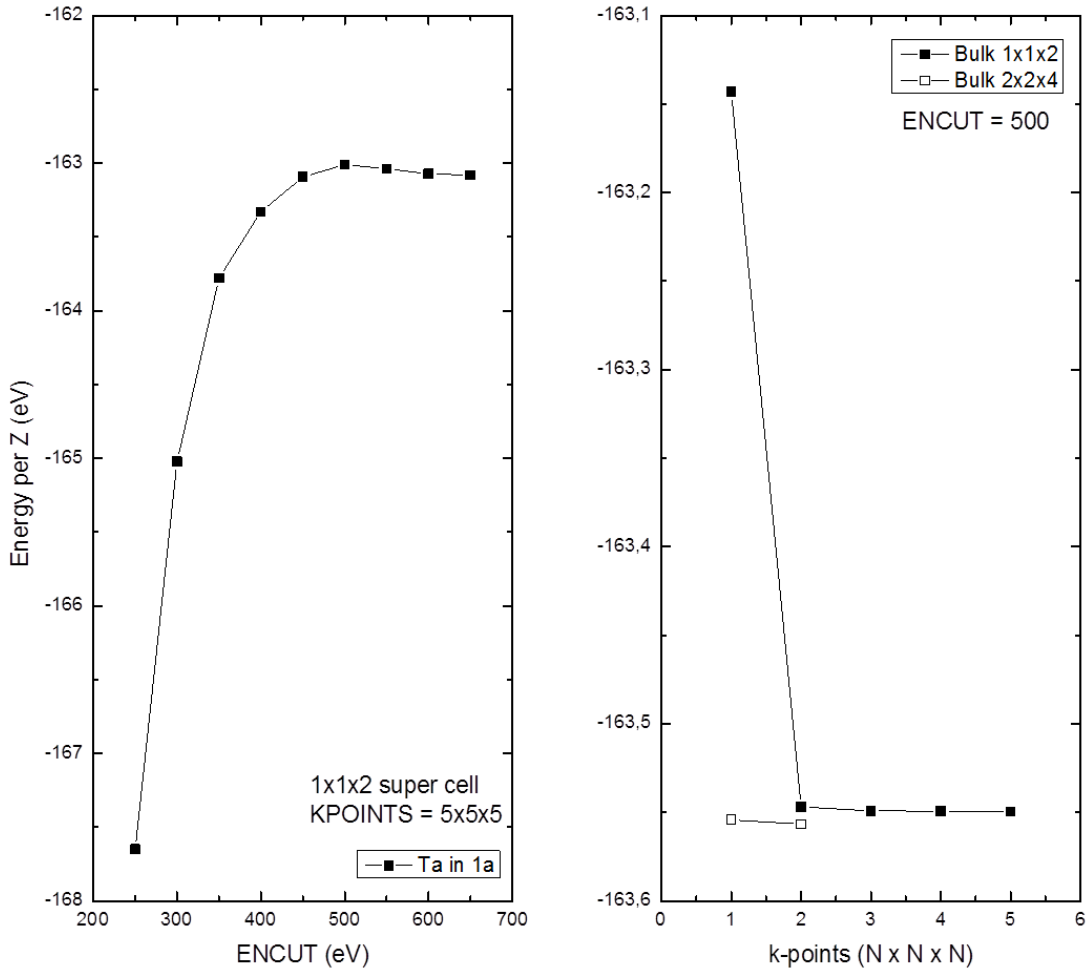

Figure 16 The total energy per formula unit, Z, langatate as a function of the cut-of energy (right figure) and total energy per Z with respect to k-points (left figure). In this last plot, both 1x1x2 and 2x2x4 supercells are displayed.

It is observed that the 1x1x2 supercell reaches a satisfying convergence at 3x3x3 k-points while the 2x2x4 supercell only needs the gamma point. The reason for this is the reciprocal relationship of the k-vector and cell parameter. The bigger the cell, the smaller the first Brillouin zone, and thus, less k-points are needed.

5.4 Supercell convergence

The 1x1x2 and the 2x2x4 supercells from the langatate structure were relaxed with the volume and shape of the cell as a variable. The parameters of the structurally optimized 2x2x4 supercell and the difference from experimental values [16] are shown in Table 8.

Table 8 Lattice parameters from DFT calculations after structural optimization of the 2x2x4 supercell.

Cell parameter	DFT values	Experimental values	Diff. experimental
a (Å)	8.318	8.213	1.3 %
c (Å)	5.215	5.167	0.9 %
c/a	0.627	0.629	0.3 %

This optimized lattice parameters are in good agreement with experimental values [16], and the deviation is within the range usually observed for the GGA-PBE functional. It is a known fact that GGA overestimates cell parameters. The ratio of 'c to a' is quite close to experimental values from powder diffraction data, c/a = 0.629. The optimization stabilized the structure with 0.2 eV per formula unit.

Comparing the structurally optimized 1x1x2 and 2x2x4 supercell, a difference in cell parameters of 0.006 % and 0.01 % for a and c are obtained. The total energy differs by only 0.0005 % meaning the supercell convergence is quite good, at least for the perfect, defect-free structure.

5.5 Exchange-correlation functionals

As the choice of exchange-correlation functional can have large effects on material properties, comparative calculations with the LDA and the GGA-PBE were performed on the 1x1x2 supercell. The calculations were performed with 5x5x5 k-mesh, cut-off energy of 500 eV and full structural relaxation. Cell parameters were extracted (Table 9), in addition to total energies and band structure (Table 10).

Table 9 Cell parameters of relaxed 1x1x2 supercell langatate using LDA and GGA exchange-correlation functionals.

	a (Å)	c (Å)	c/a	V (Å^3)
LDA	8.128	5.121	0.630	293.0
GGA	8.318	5.215	0.627	312.5
Exp.	8.213	5.167	0.629	301.8

Table 10 The energy and band parameters of the volume relaxed LDA and GGA are compared for the 1x1x2 supercell.

	Energy per Z (eV)	Valence band (eV)	Conduction band (eV)	Band gap (eV)
LDA	-182.6	3.20	6.79	3.60
GGA	-163.7	2.84	6.19	3.36

In general LDA underestimates cell parameters while GGA overestimates it, and there is no exception for langatate if we look at the experimental values listed in Table 9.

5.6 Chemical potential of gaseous species

The chemical potential of oxygen gas, hydrogen gas and water vapour are used for the calculations of formation energies of the different defect species in langatate. However, only the chemical potentials of hydrogen gas and water vapour have been calculated through DFT calculations. The chemical potential of oxygen gas has been derived from the two former calculations, through Eq. 38 and Eq. 39.

$$\frac{1}{2}O_2(g) + H_2(g) = H_2O(g) \qquad \text{Eq. 38}$$

$$\mu_{O_2}^{DFT} = 2\left(\mu_{H_2O}^{DFT} - \mu_{H_2}^{DFT}\right) \qquad \text{Eq. 39}$$

It is known that GGA does not compute the bonding energy of the oxygen molecule very well. In Table 11 the calculated chemical potential of the different gaseous species are displayed.

Table 11 The chemical potential of the different gaseous species used in this thesis. The chemical potential of oxygen gas is derived from the chemical potential of water vapour and hydrogen gas.

$\mu_{O_2}^{DFT}$ (eV)	$\mu_{H_2O}^{DFT}$ (eV)	$\mu_{H_2}^{DFT}$ (eV)
-14.90	-14.22	-6.77

6. Density Functional Theory Results

In this chapter structural configuration of langatate, formation energies of the different defects and reaction enthalpies will be addressed.

The first calculation will be on the site preference of the tantalum ion to observe which cation site it prefers in the structure. Secondly, since langatate has a disordered cation site (1a site), defining the initial unit cell is not straight forward. The question is how to distribute the tantalum and gallium ions on the 1a sites in the supercell. Since a single unit cell only contains one 1a site, a 2x2x4 supercell was used to test different Ga/Ta configurations. In Figure 15 we see the construction of the 2x2x4 supercell. It consists of 16 cubes, where each cube represents a unit cell langatate (NB: langatate is not cubic). Each corner of the cube is a 1a disordered cation site, giving a total of 16 1a sites. Four different configurations were made and tested where Ta occupy half of these sites.

The main defects that will be that will be investigated are oxygen and hydrogen defects. For these calculations the structurally optimized 2x2x4 supercell was used with tantalum atoms in 1a sites with configuration A, as seen in Figure 18. Finally, from these data, the hydration enthalpies will be calculated.

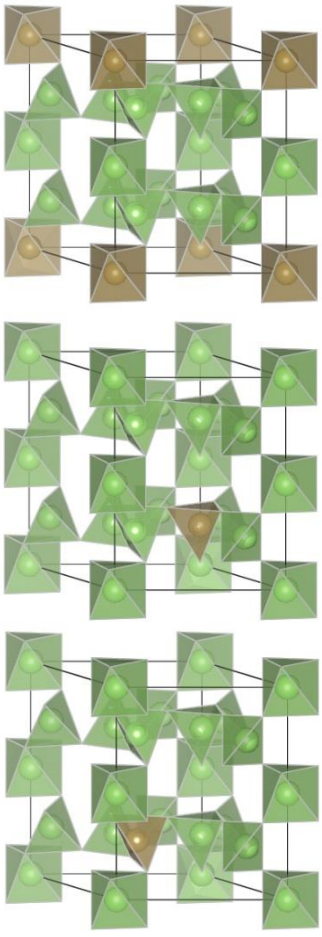

Figure 17 A 1x1x2 supercell of langatate before relaxation. In the top image we see Ta in the 1a site, in the middle we see Ta in the 2d site and at the bottom we see Ta in the 3f site. La atoms are hidden for better view.

6.1 Tantalum ordering

Tantalum can have an oxidation state of +3 to +5 and coordination between 6 and 8. Gallium can only have an oxidation state of +3, but can have coordination from 4 to 6. Ta ions with an oxidation state +5 and coordination of 6, which is the case in langatate, have a crystal radius of 0.78 Å. The 4-coordinated gallium ion has a crystal radius of 0.61 Å, while the 6-coordinated

gallium ion has a crystal radius of 0.76 Å [28]. As we can see the two ions are quite similar in size and this opens up the possibility of substitution.

Ta atom was placed in three different crystallographic cation sites in the lattice; the 1a octahedral site and the 2d and 3f tetrahedral sites, see Figure 17. Occupation of the 3e lanthanum site was not considered due to large radii mismatch between the lanthanum and tantalum. The calculated relative stabilities of the structures with Ta in 1a, 2d and 3f sites are 0 eV (the most stable), 1.7 eV and 0.7 eV. This indicates that Ta prefer the 1a site where it is 6-coordinated, in good agreement with experimental studies [3] [17]. In Table 12 the coordination and average tantalum-oxygen bond length is displayed.

Table 12 Energy per formula unit Z, coordination and the average tantalum-oxygen bond length of the three structures.

	Ta in 1a site	Ta in 2d site	Ta in 3f site
Rel. energy per Z (eV)	0	1.7	0.7
Coordination of Ta	6	4	6
Average Ta-O (Å)	2.00	1.87	2.02

The second most stable of the three structures, Ta in 3f site, is distorted after relaxation so that the tantalum ion becomes six-coordinated. The structure with Ta in the 2d site, which is the least stable of the three, forms a tetrahedron. Tantalum has indeed a preference to be six-coordinated.

Only the structure with Ta in the 1a octahedral site will be used in the remaining calculations.

6.2 Configuration of the disordered cation sites

Four different configurations of tantalum and gallium atoms on cation site 1a were examined (see Figure 18). Configuration A has tantalum atoms distributed on every other horizontal plane, configuration B has tantalum atoms distributed on every other vertical plane, configuration C has a the tantalum atoms distributed on every other

diagonal plane while the last configuration, D, has the tantalum atoms distributed practically on every second 1a site in all directions.

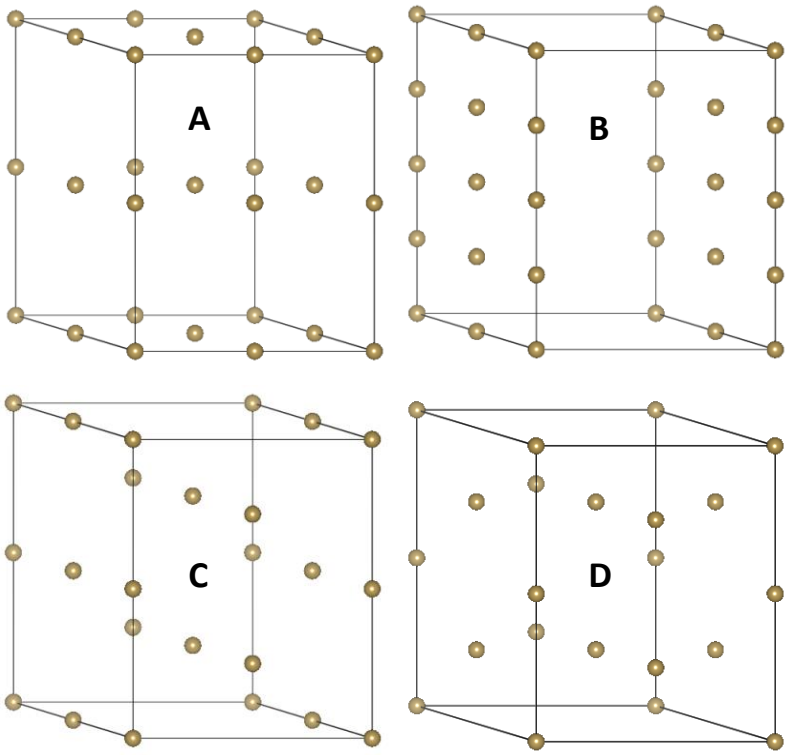

Figure 18 The four configurations, A, B, C & D, of the 2x2x4 supercell. Only the tantalum atoms are shown, which occupy half the 1a sites in this supercell.

Table 13 Cell parameters and relative energies per formula unit langatate of the four different configurations calculated for the 2x2x4 supercell.

Configuration	a' (Å)	c' (Å)	a/c	Rel. energy per Z (eV)
A	16.64	20.86	0.798	0.01
B	16.69	20.83	0.801	0.21
C	16.64	20.86	0.798	0
D	16.63	20.86	0.797	0

The lattice parameters and total energies of configuration A, C and D are nearly identical (Table 13). Structure B on the other hand differs somewhat in both the cell parameters and the energy per formula unit langatate with a difference of roughly 0.2 eV. These results indicate that langatate is a mix of structure A, C & D and is disordered at cation site 1a.

In Figure 19, the density of states (DOS) of the defect-free langatate structure is displayed. This is the DOS for structure A with Ta on the 1a sites (as seen in Figure 18). In the figure, the total DOS is displayed as well as DOS of the ions on the topmost plot. On the rest of the plots, the DOS of the ions are shown, split up into contributions from the different orbitals; s, p, d and f. As we can see from the total DOS, lanthanum ions contribute to the conduction band, specifically the f-states, while it is mostly the oxygen ions p-orbitals that contribute to the valence band. The valence band edge (VBE) was calculated to be 2.83 eV in the defect-free structure. This is the highest occupied molecular orbital (HOMO). However, it is not always the case that the valence band edge is the HOMO. For supercells containing point defects, new states introduced might be in the band gap or conduction band, and if these states are occupied HOMO is not equal to VBE. The conduction band edge (CBE) was calculated to be 6.18 eV giving a band gap of 3.35 eV.

In the DOS-figures in this thesis the states are smeared over some distance. Note that for instance in Figure 19 there seems to be some states just above the valence band edge. This is not the case; it is the result of the smearing of the states, an effect of the calculations itself.

Only structure A will be used in the remaining calculations.

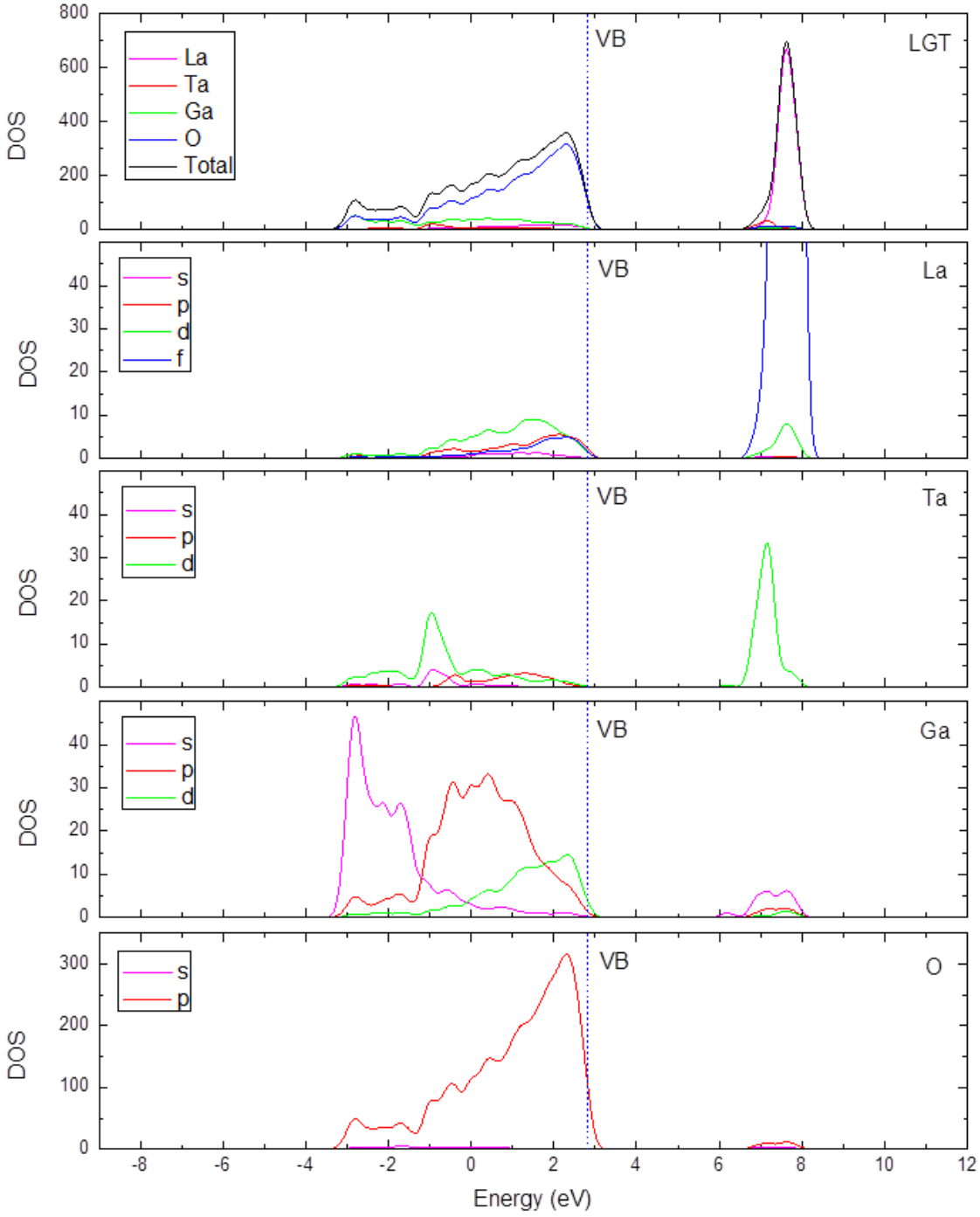

Figure 19 The density of states of the perfect bulk structure of langatate (structure A, Ta on 1a site). In the top plot, the total DOS for langatate (black) and DOS for the ions are displayed. The lower panes show the band s, p, d and f decomposed DOS for each of ion type. The valence band edge is marked with a blue dotted line.

6.3 Oxygen defects

In this section the different defect oxygen species will be investigated; oxygen vacancies and oxygen interstitial.

There are 3 different oxygen sites in langatate. However since this material has one disordered cation site (1a), it complicates the matter, and this creates different oxygen sites near the two different cations occupying the 1a sites. In this thesis four different sites will be investigated. Figure 20 displays the different oxygen positions, while Table 14 lists the corresponding Wyckoff positions and fractional coordinates.

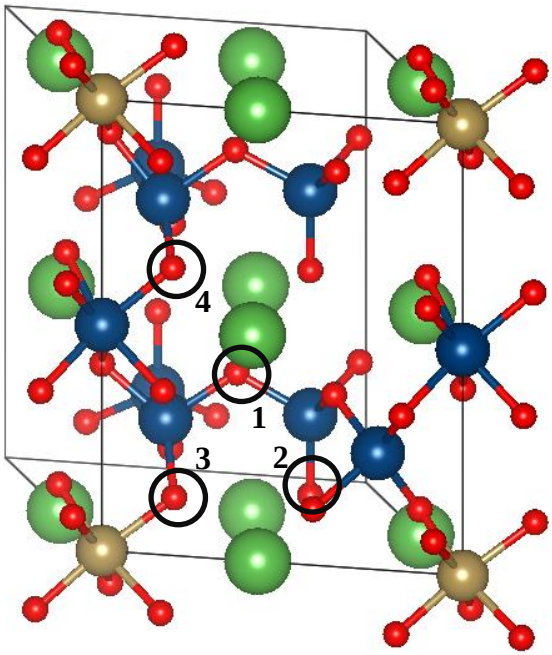

Figure 20 The four different oxygen sites in langatate marked with a circle. Here shown on a 1x1x2 supercell where some atoms have been hidden for better visualization. See **Table 14** for details on oxygen numbering.

Table 14 The coordinate of the different oxygen ions in the 2x2x4 supercell.

	Wyckoff position	**Fractional coordinates**	**Comment**
O1	6g	(0.229 0.157 0.178)	Oxygen shared between Ga in site 2d and Ga in site 3f
O2	2d	(0.333 0.167 0.045)	Oxygen bonded only to one Ga in site 2d
O3	6g	(0.111 0.041 0.056)	Oxygen shared between Ta in site 1a and Ga in site 3f
O4	6g	(0.105 0.028 0.314)	Oxygen shared between Ga in site 1a and Ga in site 3f

Oxygen vacancies can have an effective charge from zero to two. The reaction of the formation of oxygen vacancies in different charge states is shown in Eq. 40.

$$O_O^{\times} = v_O^q + q \cdot e' + \frac{1}{2} O_2(g) \qquad q = [0,1,2] \qquad \text{Eq. 40}$$

For the single-charged oxygen vacancy, spin polarization has been taken into account since the calculations include odd number of electrons. Eq. 41 displays the calculation of formation energies for the different charge states of oxygen vacancy. The calculated values are displayed in Table 15 for the 2x2x4 supercell.

$$\Delta G_{v_O^q}^f = E_{v_O^q}^{DFT} + q \cdot \mu_e^{DFT} + \frac{1}{2}\mu_{O_2}^{DFT} - E_{Perf}^{DFT} \qquad q = [0,1,2] \qquad \text{Eq. 41}$$

Table 15 The formation energy of oxygen vacancy on the different sites. The valence band edge has been used as the chemical potential of electrons.

		$\Delta G_{v_O^q}^f$ **(eV) 2x2x4 (c=1/16)**		
	Site	$v_O^{\bullet\bullet}$	$v_O^{\bullet}$	v_O^{x}
O2	**2d**	-2.38	0.87	1.41
O1	**6g**	-2.56	-0.33	0.89
O3	**6g**	-3.14	-0.64	2.26
O4	**6g**	-3.13		

The doubly-charged oxygen vacancy (6g site) near the tantalum ion (1a) has formation energy of -3.14 eV. This is the most stable of the doubly charged oxygen vacancies on the different oxygen sites. However compared to the oxygen vacancy near the gallium ion at the 1a site, there is only a small difference of 0.01 eV. Kuzmicheva *et al.* reports oxygen vacancies in all oxygen sites (O2, O3, O4) except the oxygen shared between two gallium ions in site 2d and 3f (O1). [17]

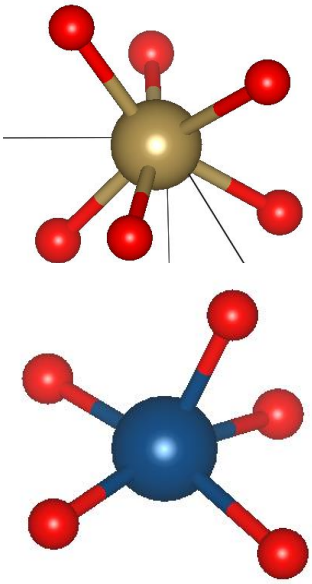

Figure 21 The 1a site cations (Ta in the top, Ga in the bottom) after relaxation with the removal of one doubly charged oxygen ion.

In Figure 21 we see the 1a cations after relaxation with the doubly charged oxygen vacancy. It is observed that the tantalum ion (top of the figure) is distorted, and attracts a nearby oxygen ion to replace the vacancy, *i.e.* seeks being

6-coordinated as a TaO_6. However the gallium ion (bottom of the figure) is stable with the loss of an oxygen ion and exists as a GaO_5 polyhedra.

The formation energy of an oxygen interstitial, O_i'', was also calculated following Eq. 42. It was placed between two La-ions parallel to the z-axis and in the centre of five Ta-ions in the xy-plane.

$$\frac{1}{2}O_2(g) + v_i^x + 2e' = O_i'' \qquad \text{Eq. 42}$$

The formation energy of the doubly charged interstitial oxygen ion in the 2x2x4 supercell is 5.65 eV with the Fermi energy of electrons set to the calculated valence band edge. At Fermi level near the calculated conduction band, however, the formation energy becomes -1.05 eV.

The oxygen ion relaxed into a position with two gallium and two lanthanum ions as its closest cations (Figure 22). The two closest gallium atoms had a bond length of 2.06 Å and 2.07 Å, respectively, with the oxygen interstitial. In comparison the average Ga-O bond length in the gallium polyhedron is 1.95 Å, which is quite similar to the bond with the oxygen interstitial. The two lanthanum ions above and below the oxygen interstitial had a La-O bond length of 2.59 Å and 2.33 Å, respectively. This bond length is shorter than the bond lanthanum makes with its other oxygen ions.

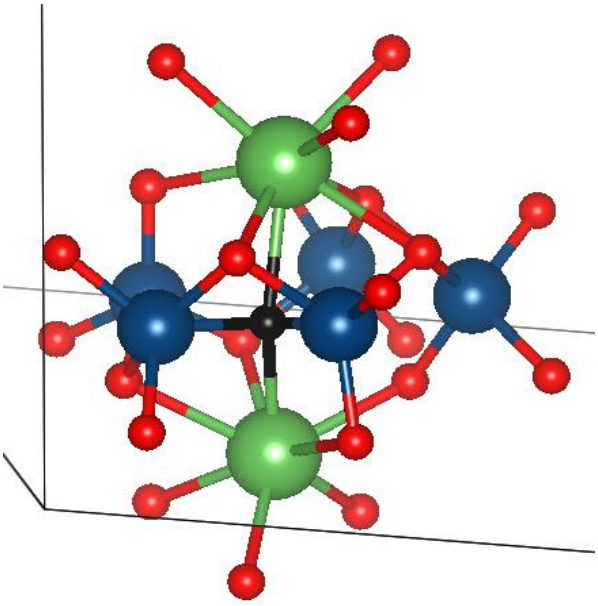

Figure 22 The oxygen interstitial ion displayed (black in this case) after relaxation. The bonds to the two gallium ions (blue) and the two lanthanum ions are shown.

In Figure 23 we see the DOS of the interstitial oxygen. New p states are observed around 3.3 eV (which is the HOMO) for the interstitial oxygen. This overlaps with the p, d and f states of the closest lanthanum ion and the p and d states of the closest gallium ion indicating bonding of the oxygen interstitial with these cations.

Also there are overlapping states just below the VBE with the lanthanum ion.

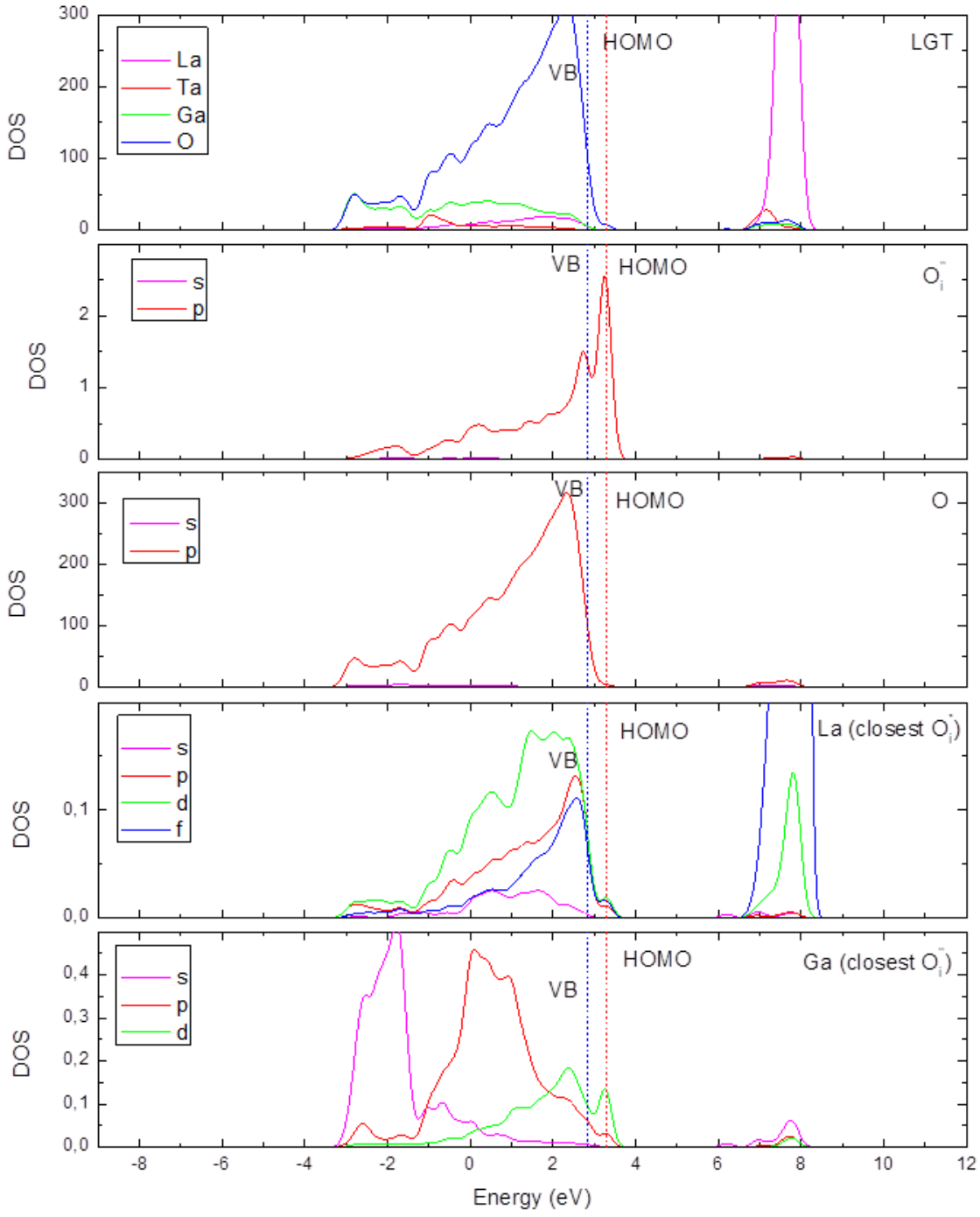

Figure 23 From the top, the DOS of the entire system, the interstitial oxygen, the other oxygen ions, the lanthanum ion closest to the interstitial oxygen and finally the closest gallium ion. The valence band edge and the highest occupied molecular orbital are marked with blue and red dotted lines, respectively.

6.4 Hydrogen defects

The three most important hydrogen defects that will be looked upon in this thesis, is the neutrally charged hydrogen atom, the positively charged proton and the negatively charged hydride ion. All of these calculations were done with the same parameters, except the position of the hydrogen species and the total number of electrons in the supercell.

$$\frac{1}{2}H_2(g) + O_O^x = OH_O^q + q \cdot e' \qquad q = [0,1] \qquad \text{Eq. 43}$$

Eq. 44 displays the calculation of formation energies for the hydrogen atom (q=0) and proton (q=1).

$$\Delta G^f_{OH_O^q} = E^{DFT}_{OH_O^q} + q \cdot \mu_e^{DFT} - \frac{1}{2}\mu^{DFT}_{H_2} - E^{DFT}_{Perf} \qquad q = [0,1] \qquad \text{Eq. 44}$$

To find the most stable hydrogen defects in the structure, a potential energy surface (PES) calculation was done. The 1x1x2 supercell was used to do the calculations. The supercell was divided into a grid consisting of 16x16x10 points where a hydrogen atom/ proton was placed in each point, and the total energy was calculated without any ionic relaxation (ENCUT = 500, KPOINTS = 2x2x2). The ten most stable configurations were used as starting points for full structural optimization of the defects in a 2x2x4 supercell.

Figure 24 displays a histogram of the relative energies of the systems with protons. The energy of the most stable supercell containing a proton was used as reference and set to 0. The histogram displays the energy difference of all of the different protons from the most stable one. We observe that a majority of the protons, 1590 of the 2560 in total, are in the range of 5 eV of the most stable position. In the range of 1 eV however there are a total of 66 protons. This gives us an indication on the number of stable positions in langatate. Note that these energies are all obtained without ionic relaxation.

The 66 most stable protons are displayed in Figure 25 plotted together in one cell. It is observed that these protons are distributed in the xy-plane between the two planes of gallium ions. Note that the supercell used in this case has been predefined with

gallium and tantalum ions in every other plane, which is not the case in practise. It can be concluded that the protons prefer being in close proximity to the oxygen bonded to the gallium ions.

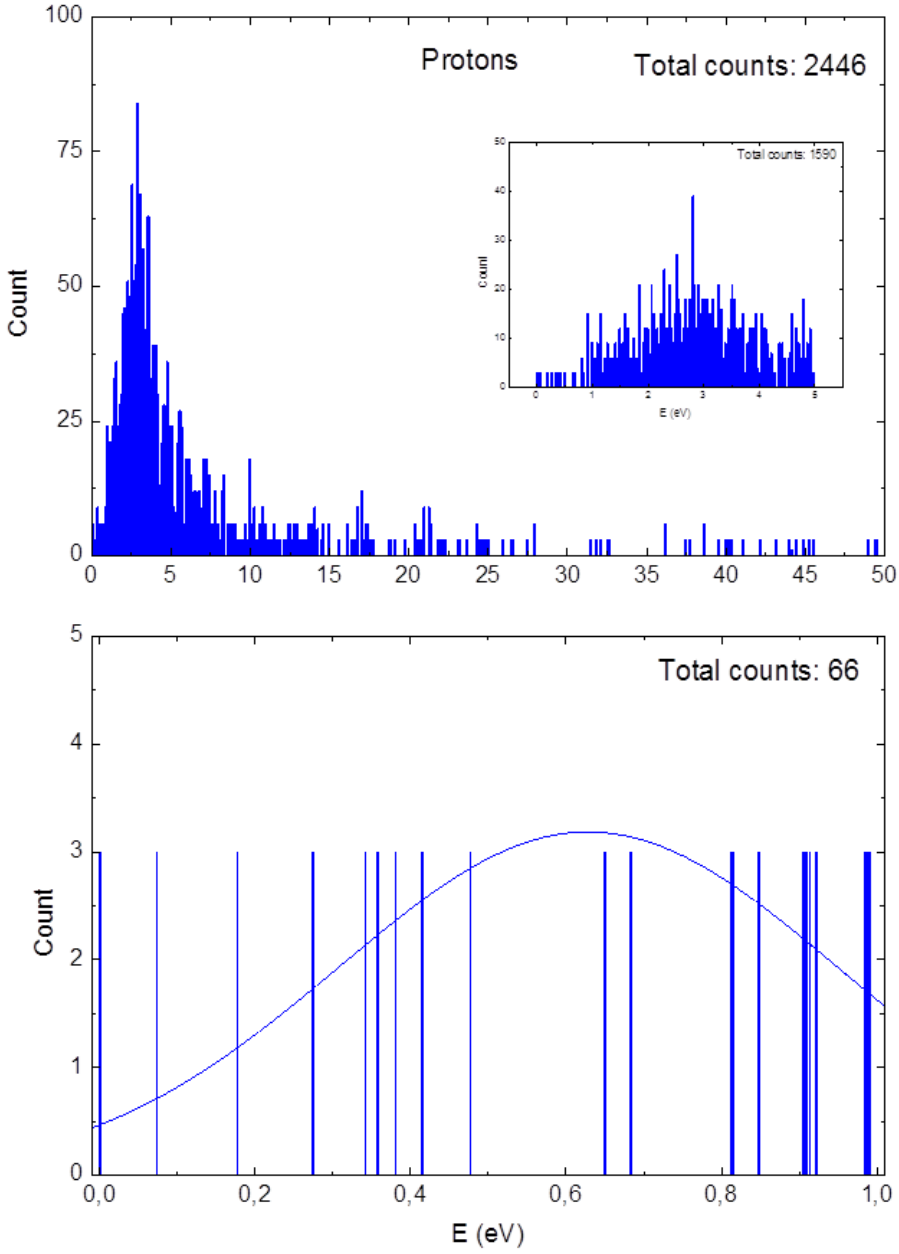

Figure 24 The distribution of the relative energies of the protons in 1x1x2 supercells. The energy of the most stable proton is used as reference (set to 0).

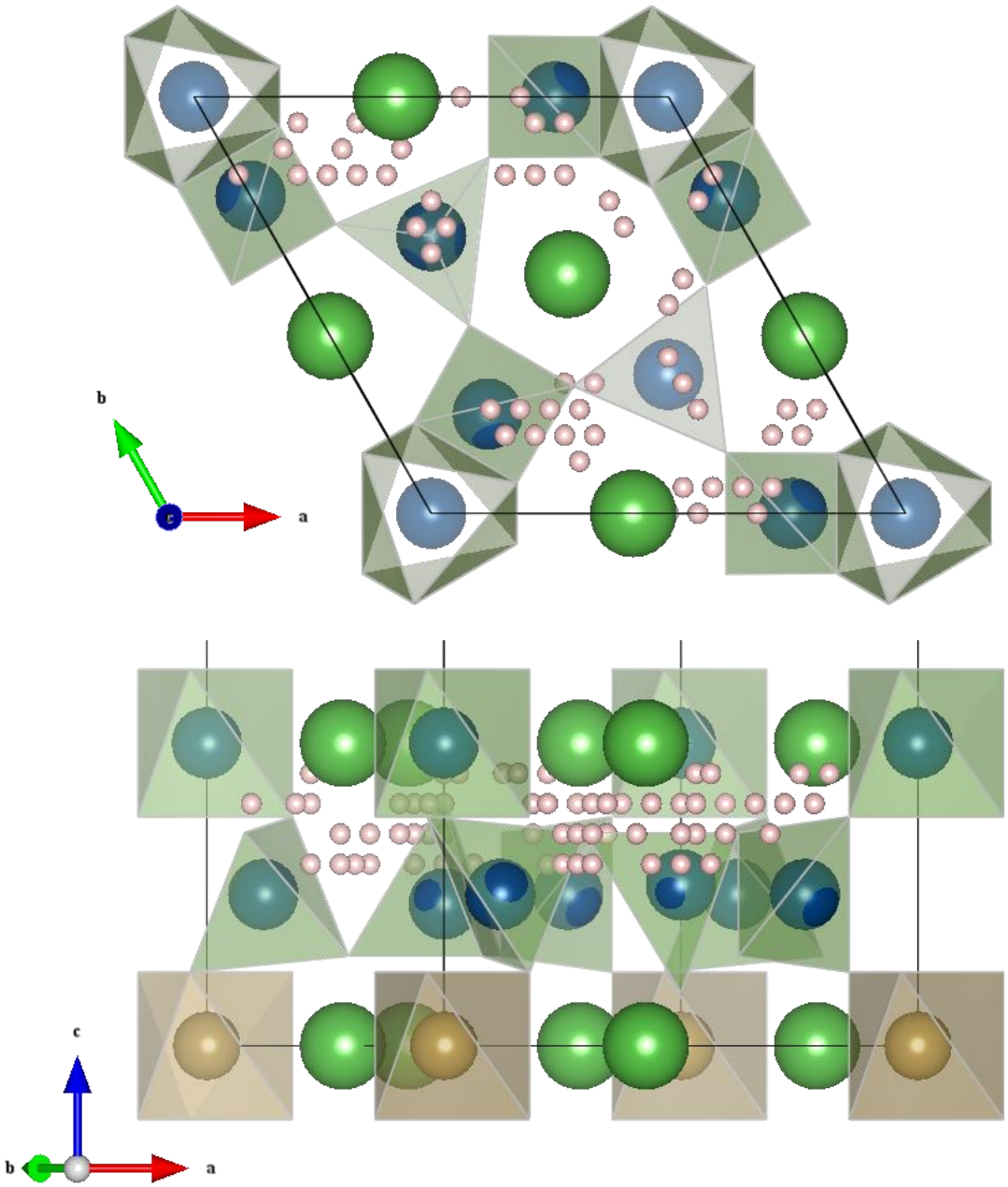

Figure 25 The distribution of the 66 most stable protons (pink) found through PES, here displayed on half the 1x1x2 supercell (*i.e.* 1x1x1 cell). All these proton positions are within 1 eV from the most stable one.

In Table 16 the formation energies of the most stable hydrogen defects are displayed. The calculations done on the 1x1x2 supercell is shown for comparison.

Table 16 The formation energy of neutral and effective positive charged hydroxide defect have been calculated, which correspond to a hydrogen atom and a proton, respectively. The valence band edge has been used as the chemical potential of the electrons.

	$\Delta G^{f}_{OH^{q}_{O}}$ (eV) 1x1x2 (c = ½)	$\Delta G^{f}_{OH^{q}_{O}}$ (eV) 2x2x4 (c=1/16)
$OH^{\bullet}_{O}$	-2.09	-2.04
OH^{x}_{O}	1.68	1.24

The most stable of the hydrogen atom and proton is clearly the latter which has formation energy of -2.04 eV with the VBE as the electron reservoir. We can observe that there are little differences in formation energy of the proton between the supercells, but bigger differences for the hydrogen atom. This might be due to the fact that protons have much smaller ionic radii than a hydrogen atom, and thus the defect-defect interaction is much less pronounced.

The proton has a distance of 0.99 Å from the closest oxygen ion (Figure 27, left). This hydroxide is bonded to two gallium ions with a bond length of 1.94 Å and 2.26 Å. In Figure 26 we see the DOS of the proton compared with the entire supercell. The HOMO in this case is 2.84 eV, which differs only slightly from the VBE (calculated from the perfect bulk structure, 2.83 eV). It is observed that the DOS of the s and p states of the proton are quite similar to the p states of the oxygen closest to the proton, in contrary to the rest of the oxygen ions. This indicates that the orbitals overlap and that the species are bonded to each other as a hydroxide. The overlap of states is significant at around -4 eV.

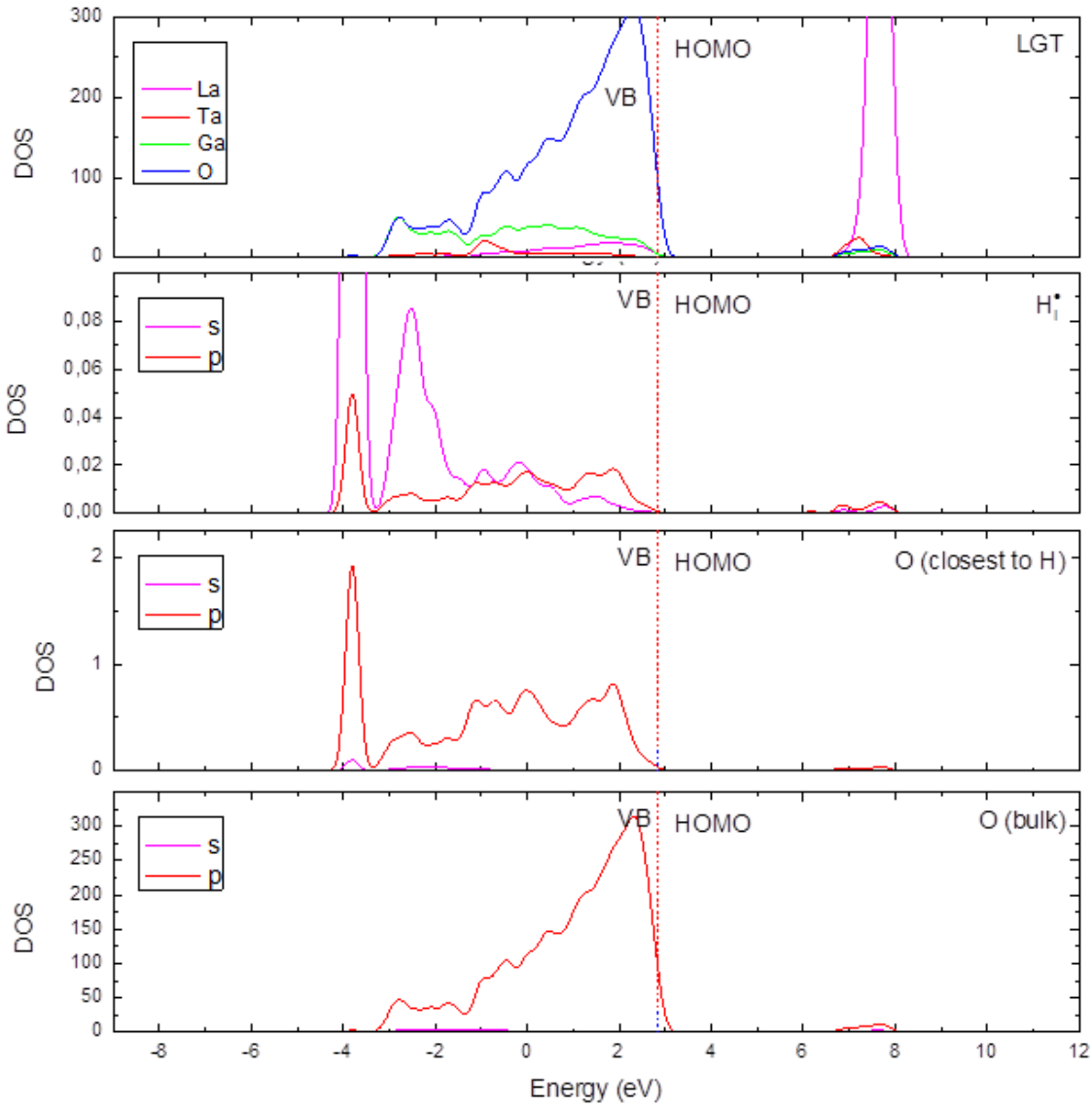

Figure 26 From the top to the bottom, the total DOS (without the DOS of the proton), DOS of the proton, the oxygen ion closest to the proton and finally the DOS of all the oxygen ions.

The hydrogen atom is closest to an oxygen ion with a distance of 0.99 Å (Figure 27, middle). This indicates that the "hydrogen atom" is not a hydrogen atom at all, but is bonded to the oxygen ion as a proton. The extra electron must be located somewhere else and not with the hydrogen species. We can see that the formation energy is 1.235 eV and much higher than the formation energy of the proton. That is a difference of 3.27 eV which is almost the as big as the calculated bandgap. This indicates that the electron is in fact excited to the conduction band, and not located with the hydrogen species. The hydroxide is bonded to two gallium ions with a bond length of 1.95 Å

and 2.22 Å. The DOS of the hydrogen species is quite similar to the proton in Figure 26, and there is quite an overlap of states with its closest oxygen ion.

The hydride was placed between two lanthanum atoms parallel to the x-axis before relaxation. Eq. 45 shows the formation of an interstitial hydride ion.

$$\frac{1}{2}H_2(g) + v_i^x + e' = H_i' \qquad \text{Eq. 45}$$

Eq. 46 shows the calculation of the formation energy of a hydride ion.

$$\Delta G_{H_i'}^f = E_{H_i'}^{DFT} - \mu_e^{DFT} - \frac{1}{2}\mu_{H_2}^{DFT} - E_{Perf}^{DFT} \qquad \text{Eq. 46}$$

The formation energy of the interstitial hydrogen species was calculated to 3.75 eV at Fermi level near the valence band edge. However the formation energy at Fermi level near the conduction band edge was calculated to be 0.403 eV. The closest cations were tantalum ion (1.82 Å away) and two gallium ions (both at 2.69 Å). The closest oxygen atom to the hydrogen species was about 2.18 Å away. This indicates that this hydrogen species is in fact a hydride ion. A closer look at the nearest tantalum ion and its surrounding anions (Figure 27, right) show that the closest anion is in fact the hydride while the six oxygen ions are bonded with an average bond length of 2.07 Å indicating that the tantalum ion is 7-coordinated in the form of a TaO_6H polyhedra unit. This is supported by the DOS (Figure 28); the s-states of the hydrogen interstitial overlap with the d states of tantalum. However this system does not have favourable formation energy.

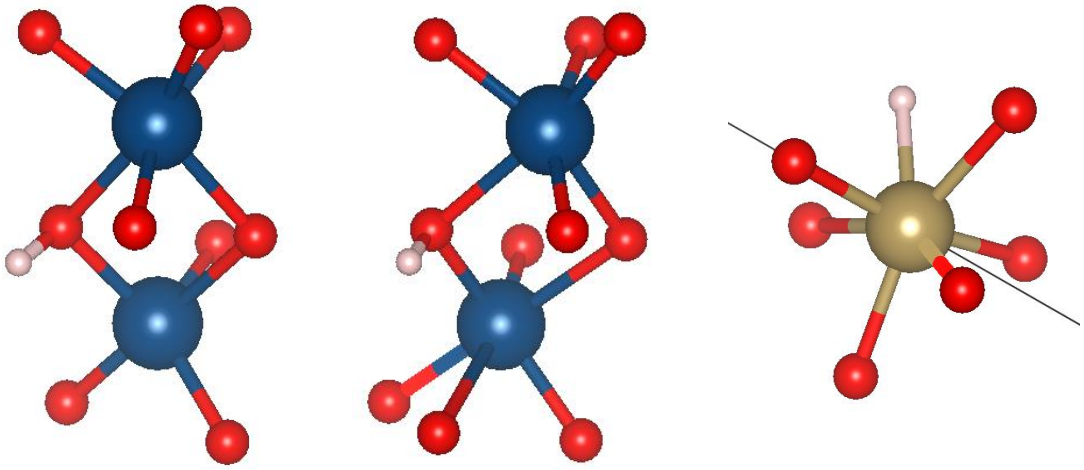

Figure 27 In this figure the hydrogen species are displayed after relaxation. On the left, a proton (pink) bonded to an oxygen ion (red), which in turn is bonded to two gallium ions (blue). In the middle we got the "hydrogen atom" (pink), and on the right we got the hydride ion bonded to a tantalum ion (brown).

As we can see from Figure 27 the protons seem to have a preference to be bonded to oxygen which in turn was bonded to octahedral gallium. This was the case with all of the ten most stable protons found using PES and relaxed with ionic relaxation.

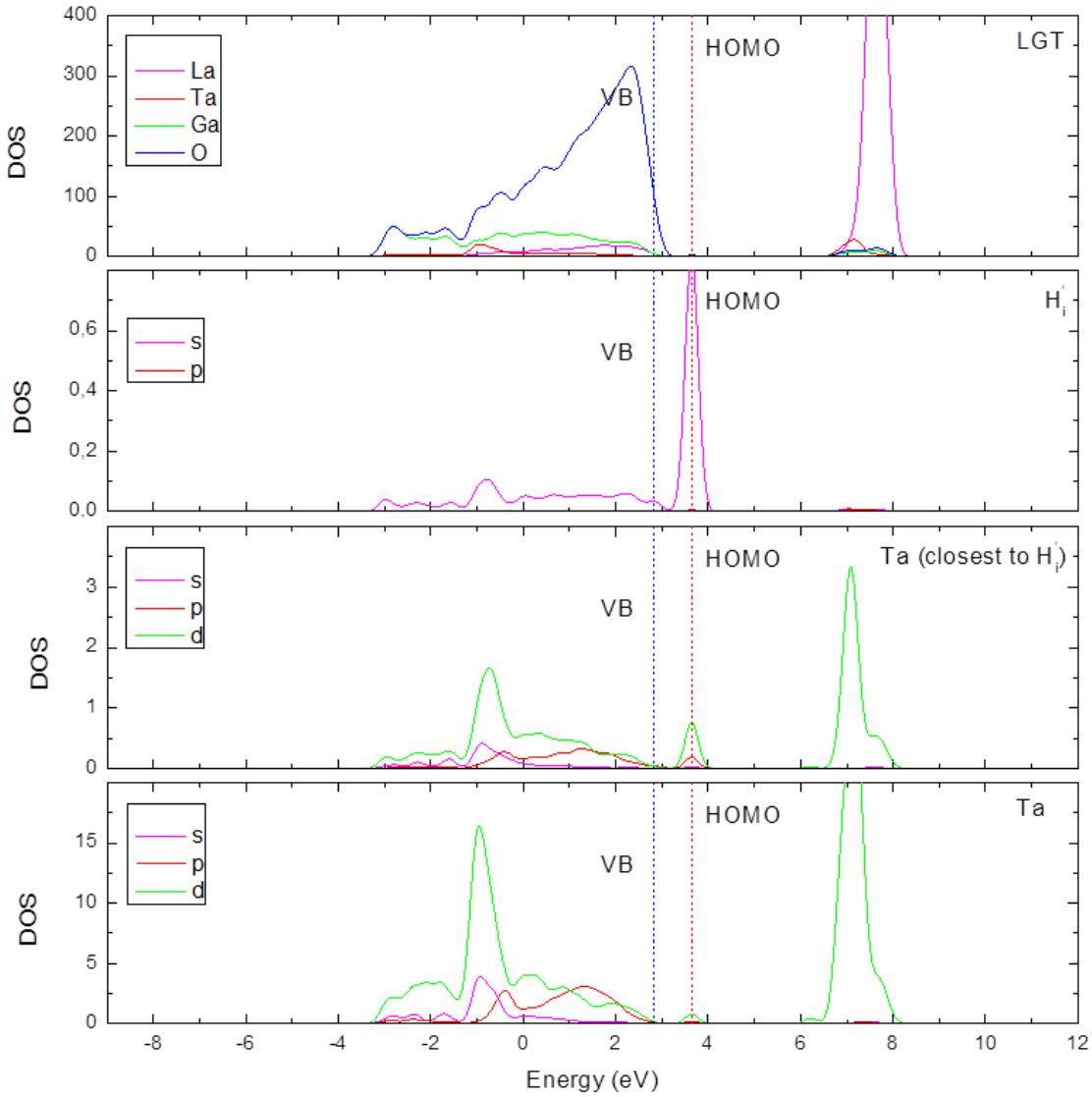

Figure 28 From the top, the total DOS, the DOS of the hydrogen interstitial, the tantalum ion closest to the hydrogen interstitial and the DOS of all tantalum ions.

6.5 Hydration enthalpy

The hydration of an oxide can be seen as the net of two individual reactions; the uptake of protons from water vapour (Eq. 47) and the creation of oxygen vacancies (Eq. 48).

$$2O_O^x + H_2O(g) = 2OH_O^\bullet + 2e' + \frac{1}{2}O_2(g) \qquad \text{Eq. 47}$$

$$O_O^x = v_O^{\bullet\bullet} + 2e' + \frac{1}{2}O_2(g) \qquad \text{Eq. 48}$$

Combination of the two above reactions yields the hydration reaction (Eq. 49).

$$O_O^x + H_2O(g) + v_O^{\bullet\bullet} = 2OH_O^{\bullet} \quad \text{Eq. 49}$$

The Gibbs energy of hydration is given by Eq. 50. At absolute zero, the Gibbs energy of hydration is equal to the hydration enthalpy.

$$\Delta G_{Hydr} = \Delta H_{Hydr} - T\Delta S_{Hydr} = \Delta H_{Hydr}^{T=0} = 2E_{OH_O^{\bullet}}^{DFT} - E_{Perf}^{DFT} - \mu_{H_2O}^{DFT} - E_{v_O^{\bullet\bullet}}^{DFT} \quad \text{Eq. 50}$$

Table 17 displays the hydration enthalpies. The calculations on the 1x1x2 supercell are shown for comparison. The formation energy of the most stable proton was used for the calculation along with the formation energies of the four different oxygen vacancies.

Table 17 The hydration enthalpy of langatate with the most stable proton position, and the four different oxygen vacancy sites. See **Table 14** for oxygen numbering.

			1x1x2		**2x2x4**	
		Site	ΔH_{Hydr} **(eV)**	ΔH_{Hydr} **(kJ/mol)**	ΔH_{Hydr} **(eV)**	ΔH_{Hydr} **(kJ/mol)**
$v_O^{\bullet\bullet}$	**O2**	**2d**	-2.50	-240	-1.70	-163
	O1	**6g**	-1.65	-159	-1.51	-145
	O3	**6g**	-1.17	-113	-0.933	-89.6
	O4	**6g**			-0.942	-90.6

Looking at the most stable oxygen vacancy (6g site), we get a hydration enthalpy of -0.94 and -0.93 eV when hydrating the oxygen vacancy near gallium and tantalum, respectively. The hydration enthalpies of the other oxygen sites are more favorable, with -1.7 eV at the 2d site as the most stable.

6.6 Defects in langatate

In Figure 29 the formation energies of the various oxygen vacancies and defect hydrogen species are displayed as a function of Fermi level. Only the most stable defects are presented. The valence band edge has been set to 0 eV while the conduction band edge is derived from the experimental band gap calculated from DFT. In the top left figure, formation energies at 0 K are presented.

By combining the experimental values obtained from DFT calculations and table values of thermodynamics data, it is possible to extrapolate the formation energies of different defects species in langatate to higher temperatures and different atmospheres using Eq. 51. Figures of the formation energies in different temperatures and atmosphere are presented in Figure 29.

$$\mu_i = \mu_i^o + G(T) + RTln\left(\frac{p_i}{p_i^o}\right) \qquad \text{Eq. 51}$$

In the following figures the terms wet and dry represent a water vapour partial pressure of $2.66 \cdot 10^{-2}$ and $1.00 \cdot 10^{-5}$, respectively, and the terms "oxygen" and "argon" represents oxygen partial pressure of 1.0 and $1.0 \cdot 10^{-5}$ bar, respectively.

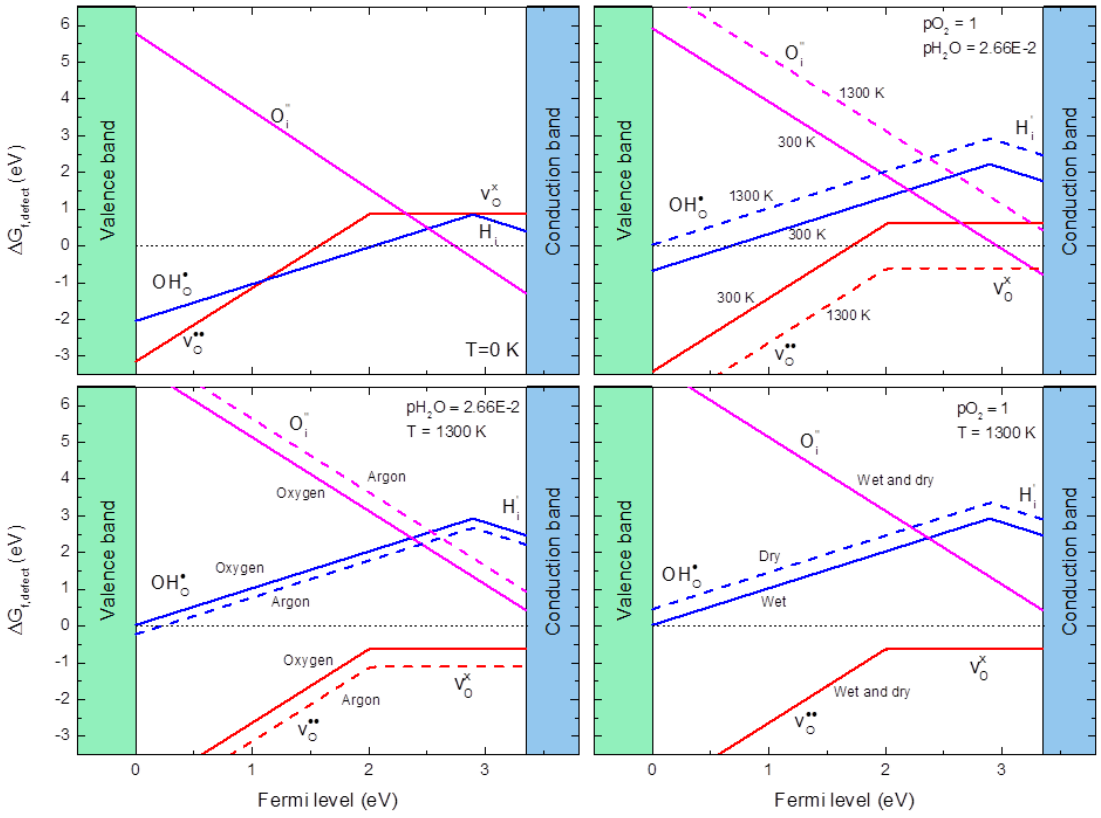

Figure 29 The formation energies of the different defect species as a function of the electron potential. From the top left going clockwise; the formation energy at T = 0 K, the formation energy at 300 K and 1300 K, the formation energy at different partial pressure of oxygen gas, and finally the formation energy in wet and dry conditions. The different defects are oxygen interstitial (purple), hydrogen (blue) and oxygen vacancy (red) with various charge states.

We see from Figure 29 that the singly charged oxygen vacancy, $v_O^{\bullet}$, is never stable, as well as the neutral hydroxide, OH_O^x. Oxygen interstitial becomes favourable at higher Fermi level as well as the hydride. The Gibbs formation energy never becomes negative, however it is known that the bandgap calculated with (PBE) GGA is not accurate. It was shown by Chung *et al.* that the correct bandgap is likely around 5 eV. Nevertheless, it cannot be known if it is the valence band that is lowered, the conduction band that is raised, or both that moves from each other.

7. Experimental results

This chapter presents the results of the compositional and electrical characterisation of and single polycrystalline.

7.1 Synthesis

Figure 30 displays the nominally undoped (left) and acceptor doped (centre) polycrystalline and the Y-cut single crystal. The nominally undoped langatate had a light blue colour, while both the acceptor-doped and all of the single crystals were yellow.

Figure 30 From left to right, the undoped polycrystalline, the acceptor-doped polycrystalline and the Y-cut single crystal langatate.

In Table 18 the sample thickness, electrode area and sample densities are displayed for all of the samples measured with impedance spectroscopy.

Table 18 Key values of the samples used for the impedance measurements.

	Thickness l (cm)	**Electrode area A (cm^2)**	**Sample density**
LGT	0.26	0.42	85 %
LGT2.5	0.27	0.47 / 0.51[2]	92 %
SC LGT X-cut	0.025	0.30	100 %
SC LGT Z-cut	0.025	0.30	100 %

2 The pellet was taken down after some measurements and a new platinum electrode was repainted.

7.2 Compositional and morphological characterization

XRD analyses were performed at all stages throughout the synthesis of the undoped and acceptor doped langatate as well as the X-cut single crystal. These data are displayed in Figure 31, along with powder diffraction data of langatate and lanthanum gallate. It is observed that the sintered acceptor-doped sample has some secondary phases of $LaGaO_3$.

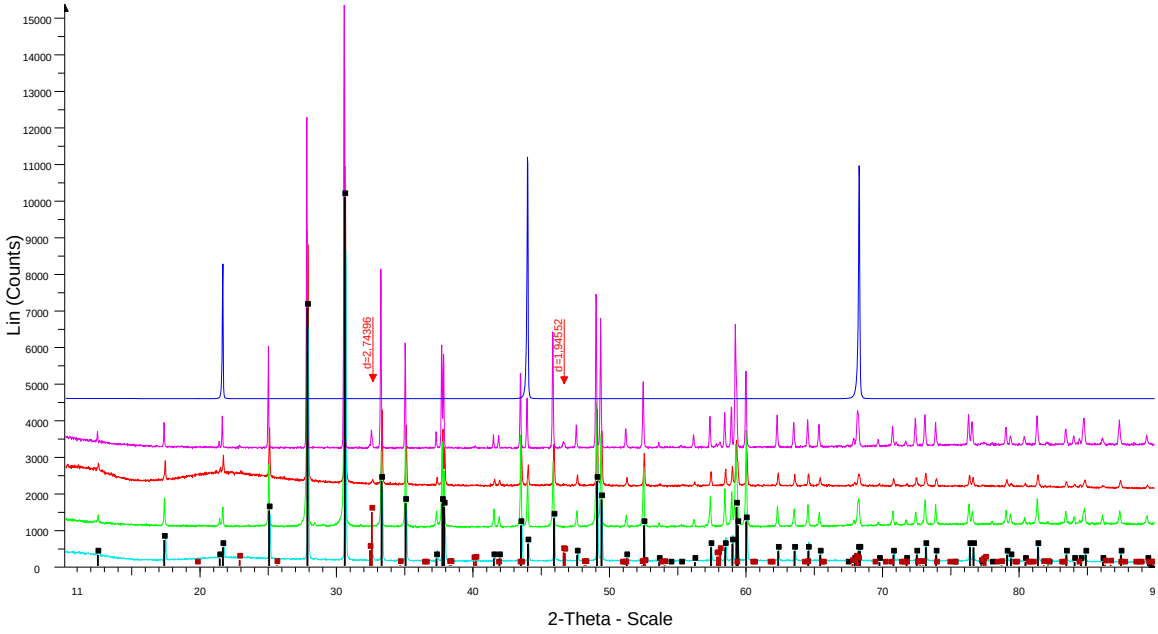

Figure 31 X-ray diffraction spectrum of a) undoped calcinated LGT (light blue), b) undoped sintered LGT (green), c) calcinated 2.5 mol% Ga-doped LGT (red), d) sintered 2.5 mol% Ga-doped LGT (purple), e) single crystal X-cut LGT (blue), f) Powder Diffraction Data (PDF) of LGT (black) and g) PDF of $LaGaO_3$ (brown).

In Figure 32 XRD-data of all the single crystals (X-, Y- and Z-cut) are shown. The peaks were indexed as shown in Table 19.

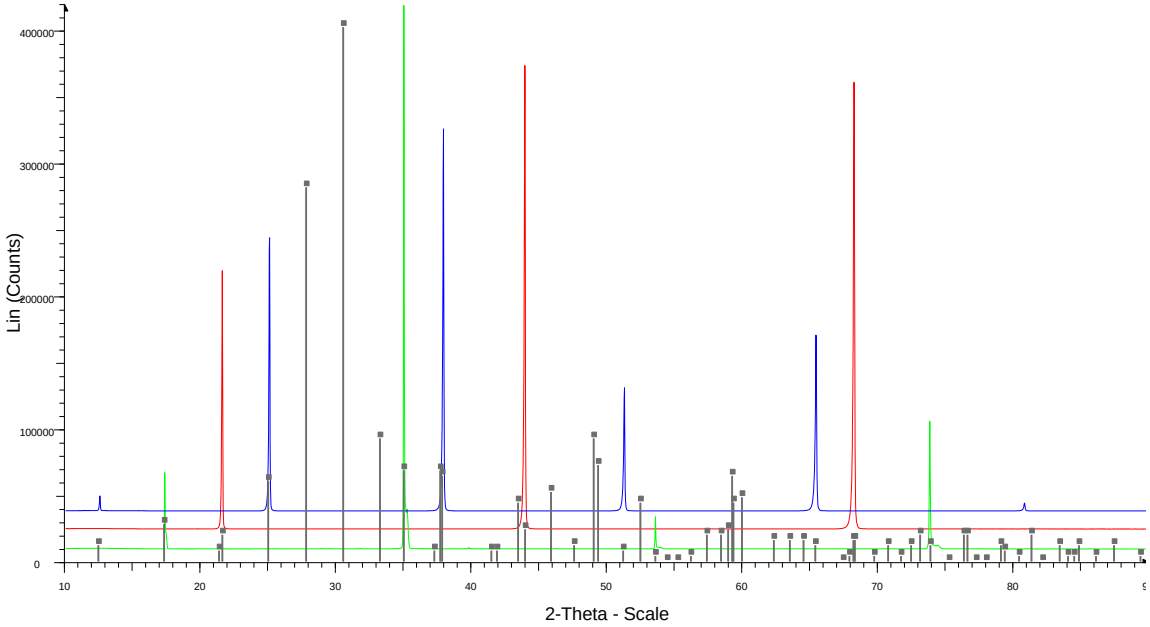

Figure 32 X-ray diffraction spectrum of single crystal LGT a) X-cut (red), b) Y-cut (blue) and c) Z-cut (green). d) PDF of LGT (grey) is shown for comparison.

Table 19 The different peaks from XRD of the X-cut, Y-cut and Z-cut single crystals were indexed.

X-cut (red)		**Y-cut (blue)**		**Z-cut (green)**	
2θ	**h k l**	**2θ**	**h k l**	**2θ**	**h k l**
21.587	1 1 0	12.541	1 0 0	17.348	0 0 1
43.95	2 2 0	25.071	2 0 0	35.036	0 0 2
68.294	3 3 0	37.934	3 0 0	53.621	0 0 3
		51.314	4 0 0	73.906	0 0 4
		65.485	5 0 0		
		80.911	?		

According to the crystallographic data (Table 19) the X-cut LGT has its surface as the (1 1 0) plane, the Y-cut LGT as the (1 0 0) plane and, the Z-cut as the (0 0 1) plane. In other words both the Y-cut and Z-cut crystals are cut in their actual crystallographic directions while the X-cut crystal is not cut in the crystallographic x-axis (which for the P321 point group is equivalent to the y-axis). The X-cut LGT is in fact cut diagonally in the xy-plane as seen in Figure 33. This sample will however be denoted "X-cut LGT" in the rest of the thesis.

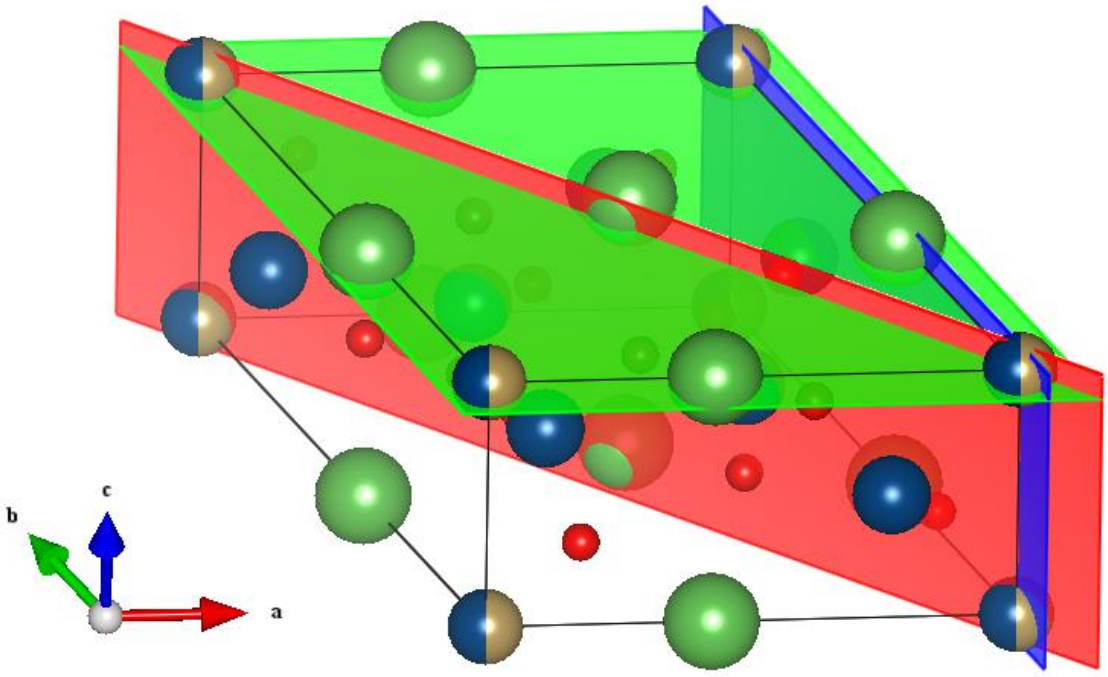

Figure 33 Here we see the different planes of the single crystals. The red plane is the (1 1 0) which corresponds to the X-cut LGT, the blue plane is the (1 0 0) which corresponds to the Y-cut LGT and lastly, the green plane is the (0 0 1) which corresponds to the Z-cut LGT.

The scanning electron microscope was used to examine the undoped langatate and the X- and Y-cut single crystals and both compositional and topographical images were captured. In Figure 34 only the X-cut LGT is shown; there were not much difference between the different single crystals. In the compositional image for the single crystals we see a lot of dark spots. EDS was performed, and according to the data, the dark spots seem to be rich in silicon (Figure 35). This impurity might have its origin from the cutting of the single crystal, and this might be the reason for the low transmittance of the single crystal samples.

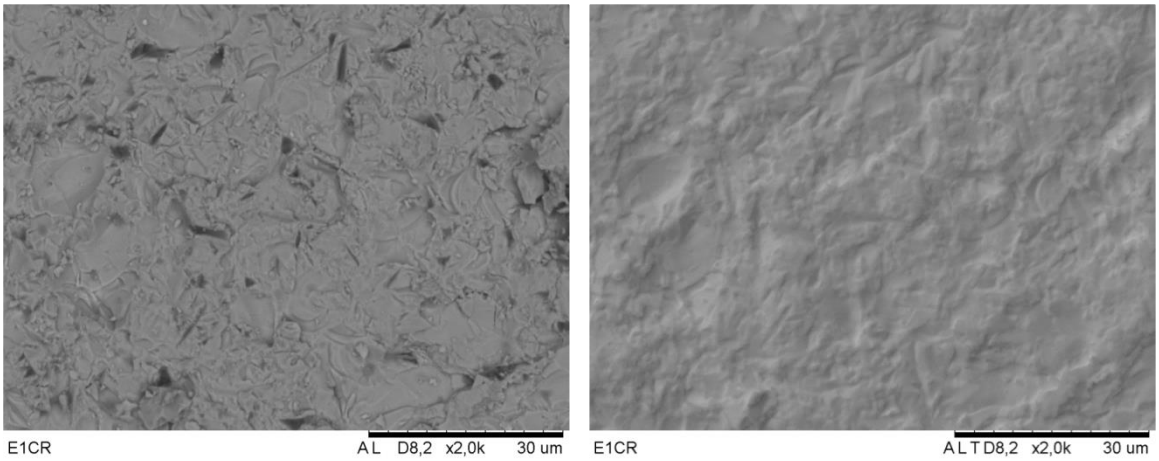

Figure 34 Compositional (left) and topographical (right) SEM-image of X-cut single crystal LGT.

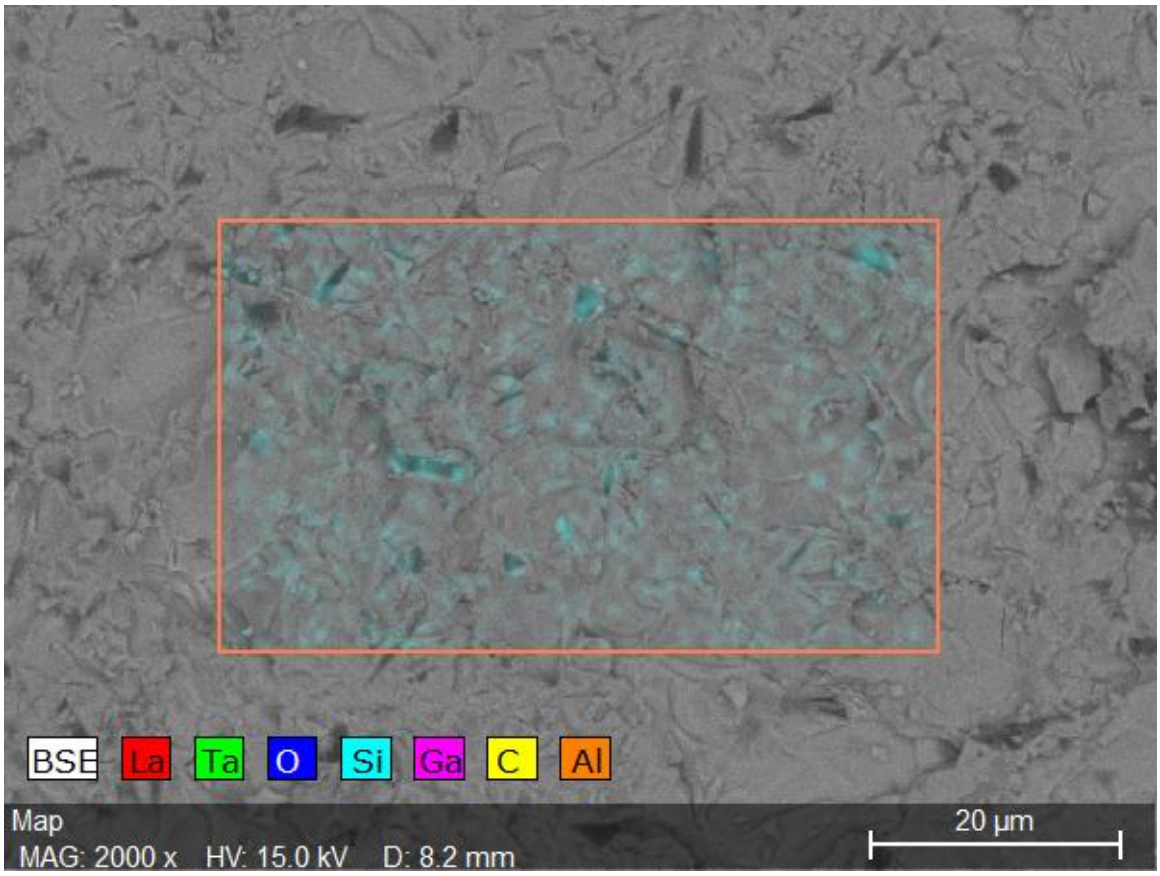

Figure 35 Compositional SEM-image of X-cut single crystal LGT with EDS scan showing silicon (highlighted). The dark parts of the sample seem to have high concentration of Si-impurities.

EDS scans were made in "representative" areas in the various samples. The results are displayed in Figure 36.

It can be seen from these figures that the trend for these samples is that single crystals are more gallium rich and have tantalum deficiency compared with the undoped langatate. Ideally undoped langatate should have 13 % lanthanum, 24 % gallium, 2 % tantalum and 61 % oxygen.

However EDS has a poor accuracy toward lighter elements, like oxygen. In addition the representative areas chosen are quite subjective and may not be as representative for the material as we would like to think.

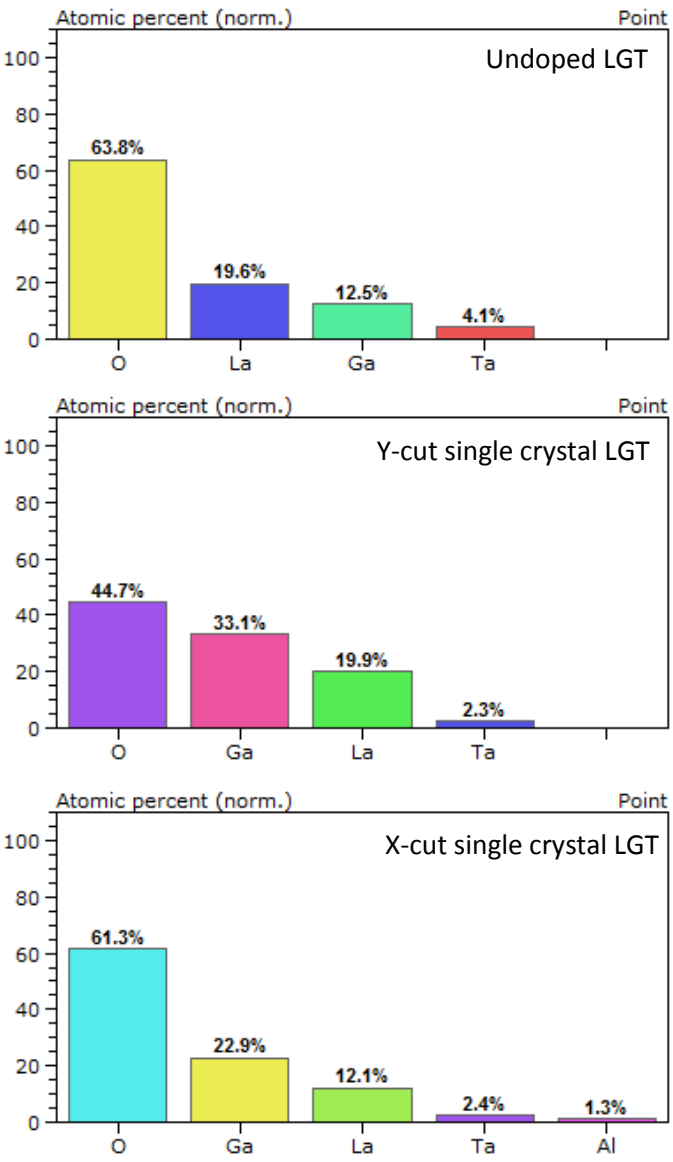

Figure 36 EDS of the various samples with atomic percentage of the various components in langatate.

7.3 UV-VIS-NIR spectrophotometry

Figure 37 shows the transmittance and reflectance of a Y-cut single crystal. There is drop in the transmittance at around 250 nm, which correspond to approximately 5 eV. This could indicate a bandgap of that magnitude, which is in accordance with DFT calculations by Chung *et al.* (chapter 3), where they reported a bandgap of 5.3 eV with the hybrid functional HSE06.[29]

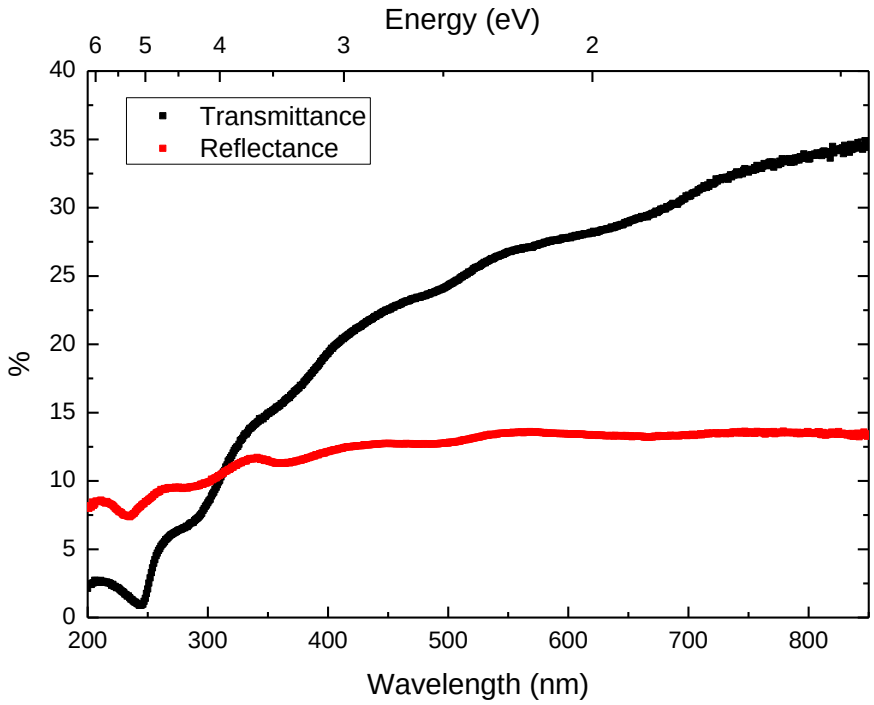

Figure 37 Transmittance and reflectance (in percentage) of the single crystal Y-cut langatate as a function of wavelength.

Because small samples were used, not all incident light hit the sample. Therefore Eq. 37 is not completely true for this particular case, and the reflectance, R, is somewhat underestimated.

7.4 Impedance Spectroscopy

This chapter presents the results from electrical characterization of undoped and acceptor-doped polycrystalline langatate, as well as the X- and Z-cut langatate single crystals.

7.4.1 Undoped langatate

Figure 38 displays the total conductivity of undoped langatate vs. inverse temperature, measured at 32 kHz. On the left of the figure measurements performed in wet and dry oxygen is displayed, while on the right measurements in oxygen and argon are presented. Total conductivity increases with temperature, and it can be seen that the effect of both oxygen partial pressure and water vapour are insignificant.

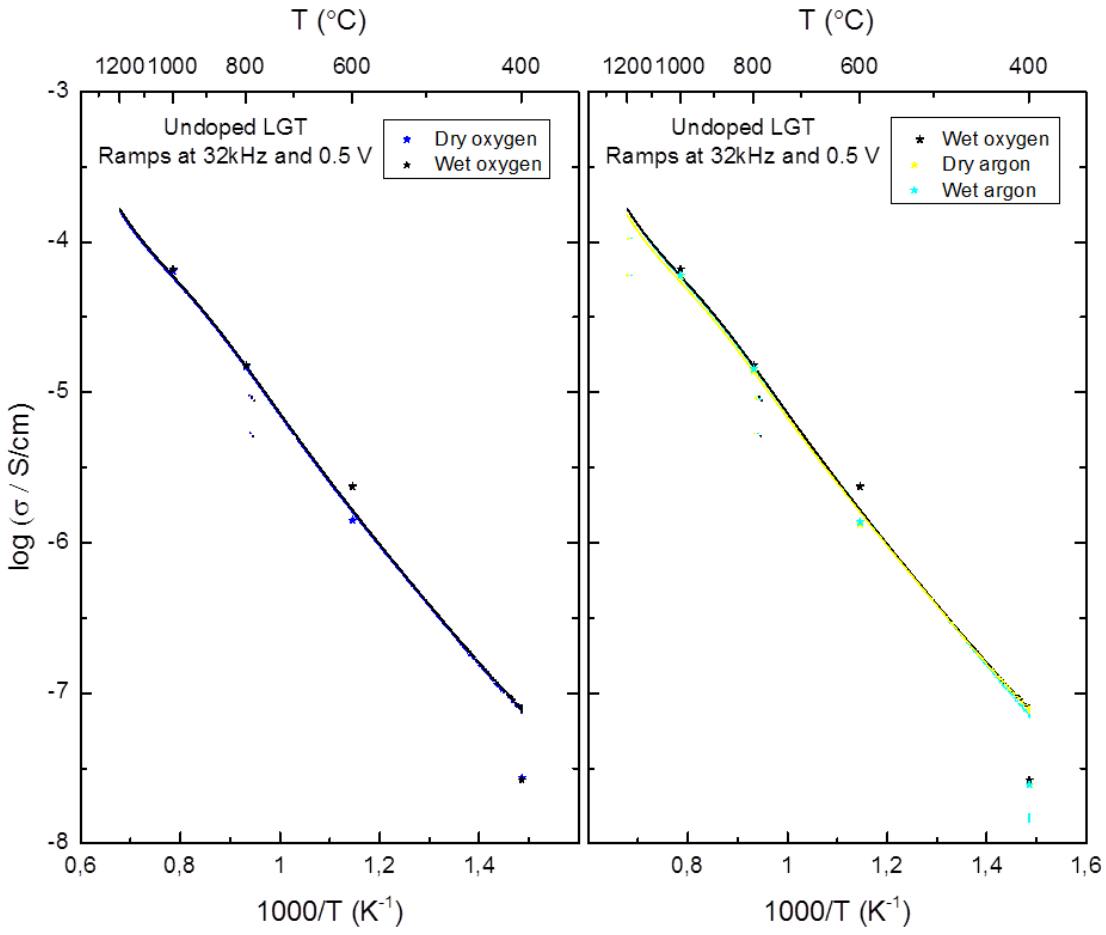

Figure 38 Total conductivity of undoped LGT as a function of inverse temperature in different atmospheres. The solid points show the bulk conductivity as obtained from deconvolution of impedance spectra.

The curves from the constant frequency measurements are all quite linear and overlapping. The curves were fitted with a linear plot, which give activation energy of 89±4 kJ/mol (0.92±0.04 eV) in the entire temperature range.

To investigate which region of the sample the 32 kHz frequency point was in, impedance spectra were performed at 600, 800 and 1000 °C in wet conditions, as displayed in Figure 39. The 32 kHz point is marked in red in each case. This point stays in the first semicircle at all of these temperatures, though it moves more outward at increasing temperatures. This is attributed to the peak frequency's dependency on the conductivity (Eq. 22).

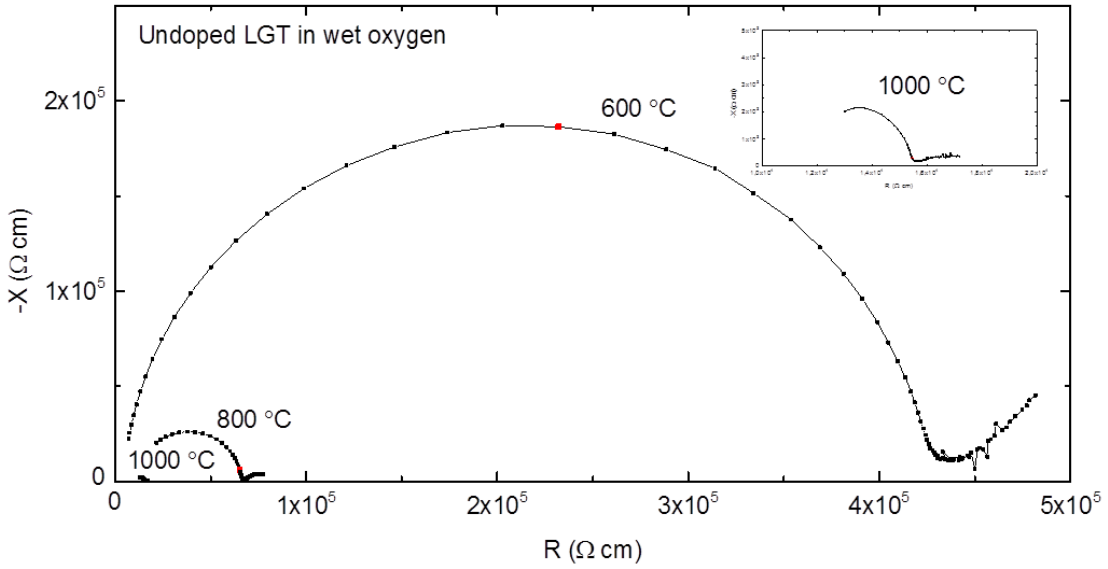

Figure 39 The evolution of the impedance spectra of the undoped LGT with temperature. The red points mark the point closest to 32 kHz. The impedance spectra performed at 1000 °C is displayed magnified in the top right corner.

Figure 40 displays impedance spectra done at the different atmospheres for the temperatures 600 °C, 800 °C and 1000 °C. In each pane the impedance spectra for wet oxygen, dry oxygen and wet argon is shown (see Table 5 for details on the atmospheres). It should be noted that these impedance spectra were not done isothermally.

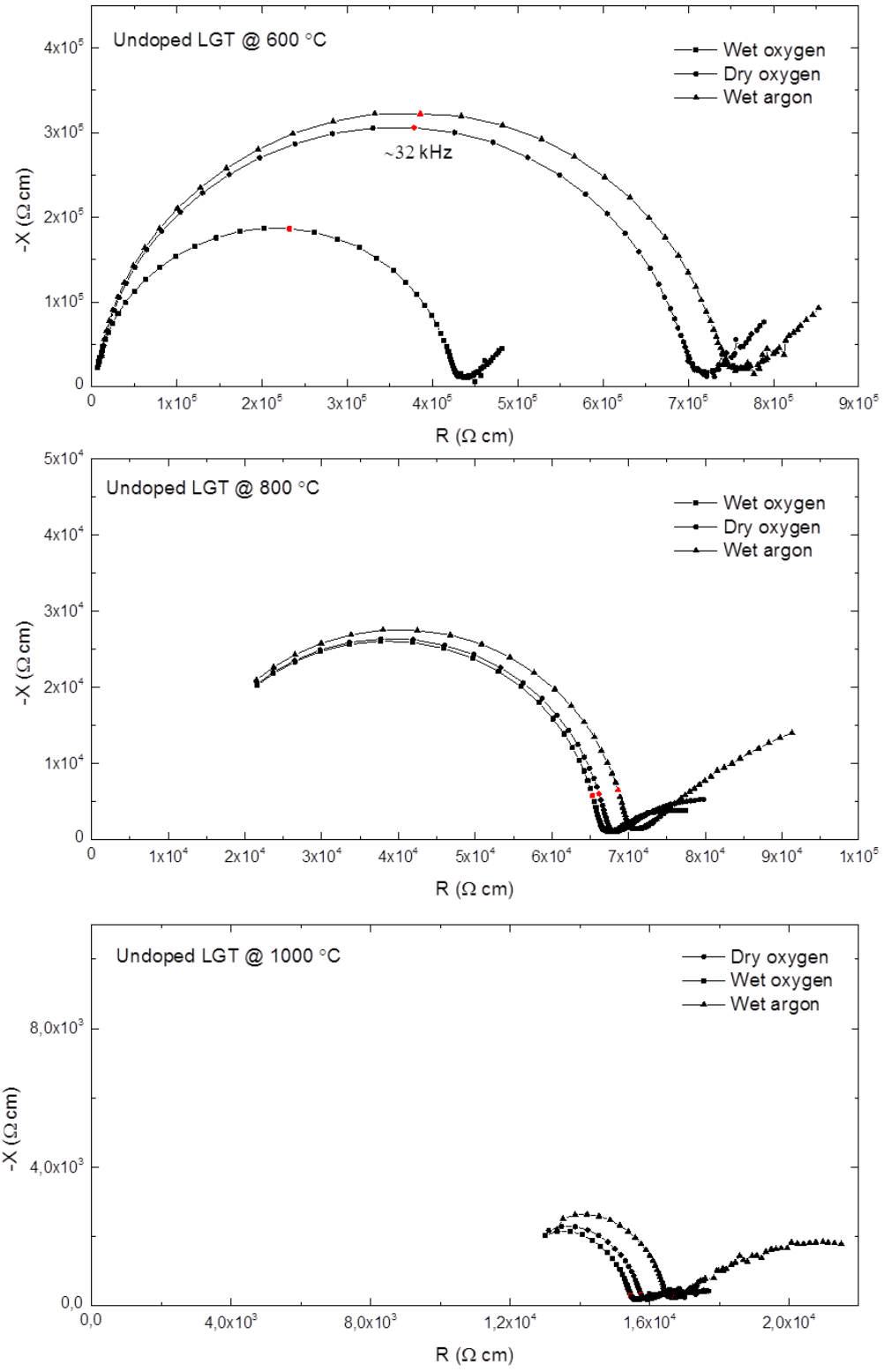

Figure 40 Impedance spectra for undoped LGT in wet and dry oxygen, as well as wet argon, in the temperatures 600 °C, 800 °C and 1000 °C. The red points mark the point closest to 32 kHz. These impedance spectra were not done isothermally.

It is seen from these figures that there is only two semicircles. These impedance spectra were fitted with a $(C[(R_1Q_1)R_2Q_2])$ or a $(C[(R_1Q_1)(R_2Q_2)])$ circuit. In Table 20 the values for resistivity and specific capacitance obtained for the first circuit element pair, R_1Q_1, is displayed (geometry has been corrected for). It is observed that the specific capacitance for this semicircle after correcting for the bulk geometry is between $[1 \cdot 10^{-12}\, F/cm, 6 \cdot 10^{-12}\, F/cm]$ which gives a dielectric constant of $[11.3\,, 67.8]$. This is of the same order of value reported by Sehirlioglu *et al.* and Axtal (Chapter 3.2) for langatate.

Table 20 The fitted values of the resistivity and specific capacitance of the first semicircle (R_1Q_1) of undoped langatate at the different atmospheric conditions and temperature.

	Wet argon		**Dry oxygen**		**Wet oxygen**	
T (°C)	**ρ (Ω cm)**	**C (F/cm)**	**ρ (Ω cm)**	**C (F/cm)**	**ρ (Ω cm)**	**C (F/cm)**
400	4.06E+07	5.19E-12	3.66E+07	5.23E-12	3.78E+07	5.29E-12
600	7.30E+05	5.53E-12	7.10E+05	5.51E-12	4.24E+05	9.50E-12
800	7.00E+04	4.43E-12	6.73E+04	4.46E-12	6.62E+04	4.44E-12
1000	1.66E+04	7.95E-13	1.56E+04	1.85E-12	1.52E+04	2.22E-12

The second circuit element R_2Q_2 is not included in Table 20 due to the uncertainty of the fitted values being too high. Nevertheless, these values gave specific capacitance of the order 10^{-5} to 10^{-9} F/cm. The former values are in the range of electrode while the latter values are in the order of grain boundaries.

As can be seen from these impedance spectra there is only a small difference between the different atmospheres, except at 600 °C, where we see a somewhat bigger difference in bulk resistivity of wet oxygen and the other two impedance spectra; dry oxygen and wet argon. This can be due to the fact that the impedance spectra were not done isothermally; "600 °C wet oxygen" was done first, "600 °C dry oxygen" three days later, and "600 °C wet argon" twelve days later. This might lead to some cation diffusion which in turn increases the resistance in the material.

The deconvoluted bulk conductivities obtained from the impedance spectra fit quite well to the total conductivity as seen in Figure 38, indicating that the bulk is dominating the total conductivity. At 400 °C the bulk conductivity values seem to be

quite off. This could mean that the bulk is not dominating the total conductivity. However, we have to take into account the limit of the impedance meter, which becomes less accurate at conductivities below 10^{-7} S/cm. Other factors are the deconvolution of the impedance spectra at 400 °C and how well the fitting is. This will not be further investigated.

7.4.2 2.5 mol% Ga-doped langatate

Figure 41 displays the total conductivity of acceptor doped langatate vs. inverse temperature, measured at 10 kHz. On the left hand side measurements performed in wet and dry oxygen are displayed, and on the right measurements done in wet oxygen and argon are displayed. It is observed that total conductivity increases with temperature and, in the lower temperature region, with increasing pH_2O (Figure 41, left). At the higher temperature range, conductivity increases with increasing pO_2 (Figure 41, right). Between 700 °C and 1100 °C, there seem to be a "bump" in the curves of the ramps, and it is observed that the effect of pH_2O is greater below this area, while the effect of pO_2 is higher above.

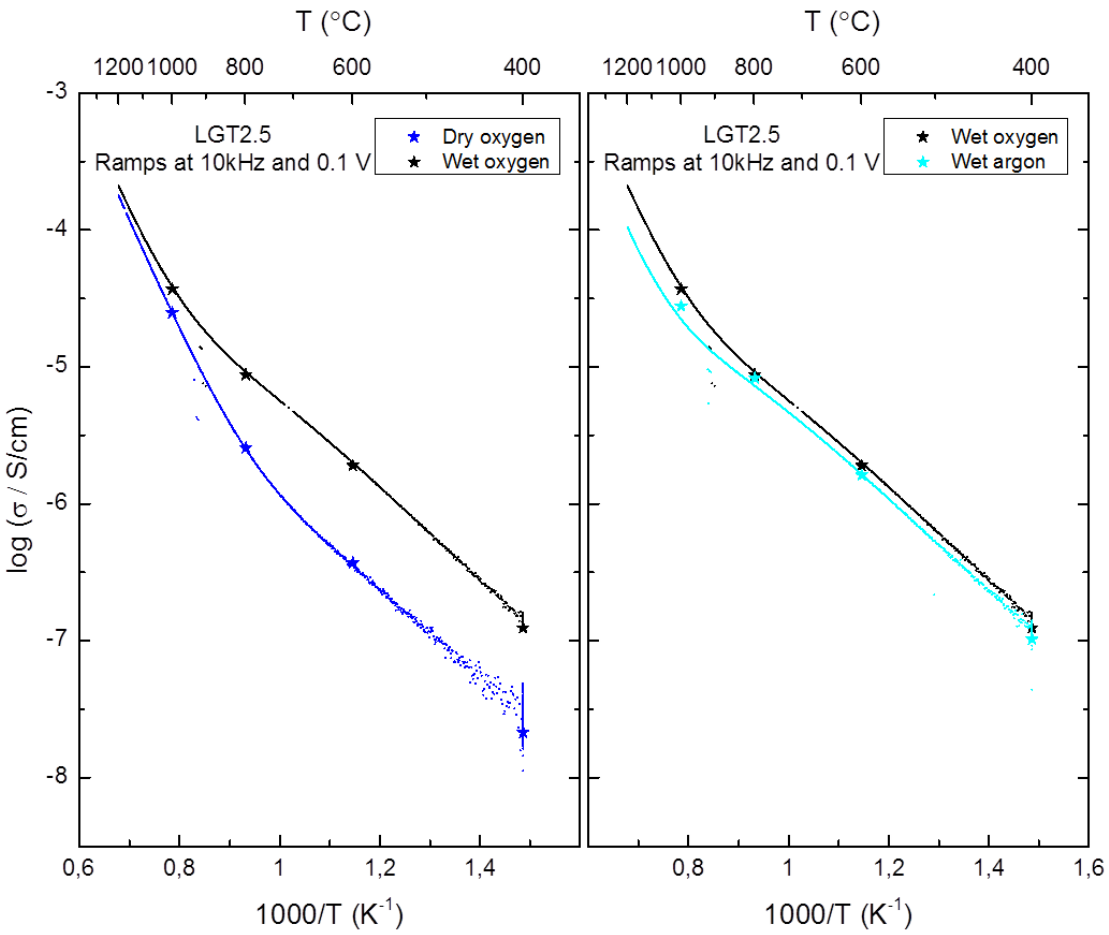

Figure 41 Total conductivity of acceptor doped langatate as a function of inverse temperature in different atmospheres. The solid points show the bulk conductivity as obtained from deconvolution of impedance spectra.

Figure 42 shows that the 10 kHz frequency is in the first semicircle at temperatures from 400 °C up to 1000 °C. It is observed that this frequency moves toward the outskirts of the first semicircle at increasing temperatures, like the case for the undoped sample. At 400 °C only the high frequency part of the first semicircle is seen, while at 1000 °C only the lower frequency part is seen. At 1200 °C the 10 kHz frequency is in the centre of the semicircle. It is logical to assume that this frequency has moved to the second semicircle, and we no longer see the first semicircle. As can be observed there is a lot of noise at this temperature so deconvolution was not possible.

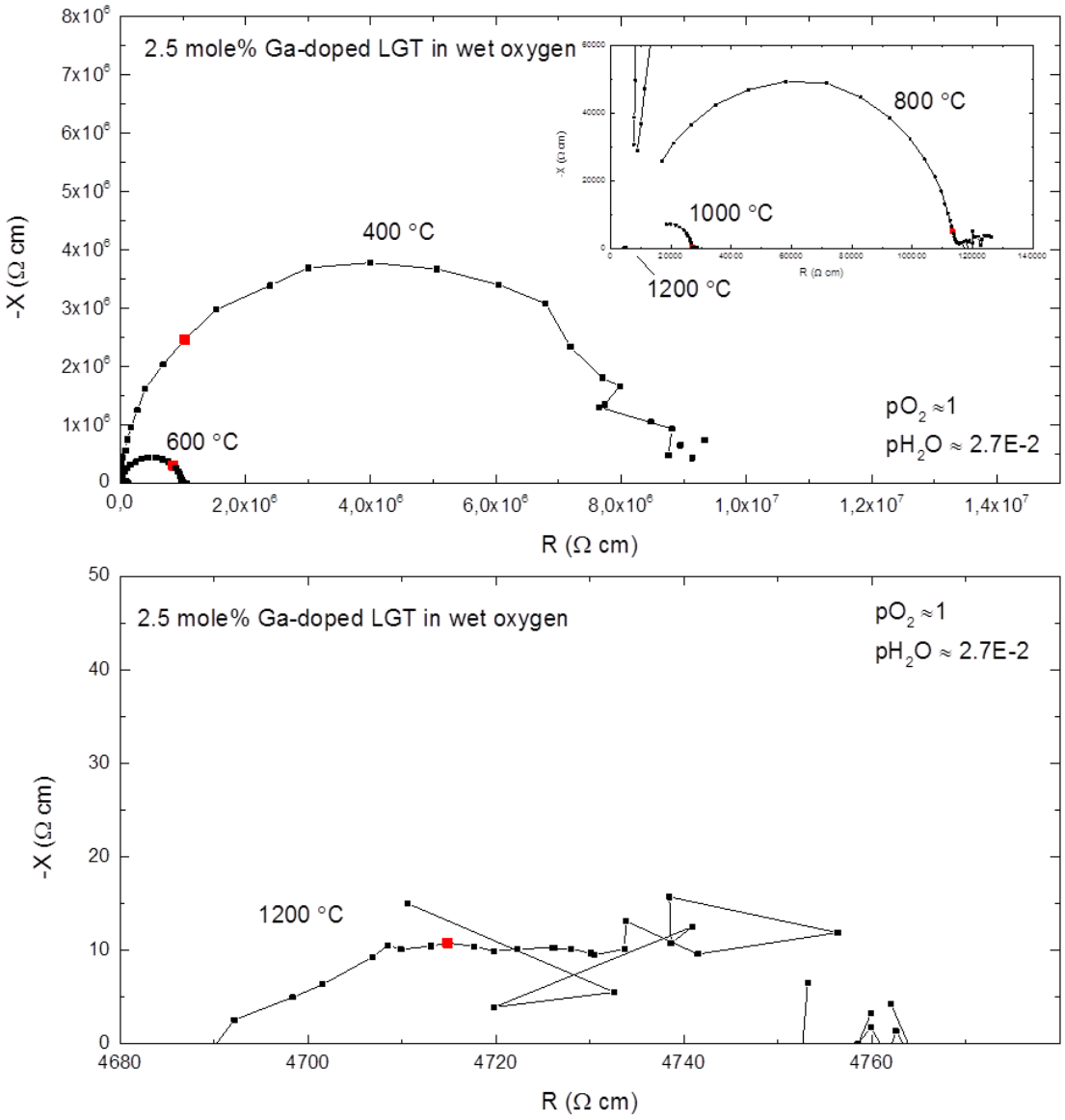

Figure 42 Impedance spectra of the acceptor-doped langatate at 400, 600, 800, 1000 °C and 1200 °C in wet oxygen. The 10 kHz frequency is shown in red. A magnified image of the 800 and 1000 °C impedance spectra are shown as well in the top pane.

In Table 21 fitted values from EQC of the first semicircle is shown. These impedance spectra were fitted with a $(C[(R_1Q_1)R_2Q_2])$ or a $(C[(R_1Q_1)(R_2Q_2)])$ circuit. A specific capacitance similar to the undoped langatate is obtained, indicating that the first semicircle is in fact representing bulk. The deconvoluted values of the bulk conductivities are plotted in Figure 41, and it is seen that the total conductivity is dominated by bulk, as the overlap is quite good.

Table 21 The fitted values of the resistivity and specific capacitance of the first semicircle (R_1Q_1) of the acceptor-doped langatate at different temperatures in wet oxygen.

	Wet oxygen	
T (°C)	**ρ (Ω cm)**	**C (F/cm)**
400	8.08E+06	5.23E-12
600	5.27E+05	5.05E-12
800	1.14E+05	4.26E-12
1000	2.71E+04	2.24E-12

In Figure 43 impedance spectra done at 800 °C with varying pO_2 at pH_2O = 0.027 atm (top) and varying pH_2O at pO_2 = 1 atm (bottom) is displayed. Only a minor effect of pO_2 is observed; the resistance of the first semicircle (bulk) is in-line with the constant frequency measurements. On the other hand, there is a significant effect of changing pH_2O; the bulk resistance decreases with increasing pH_2O.

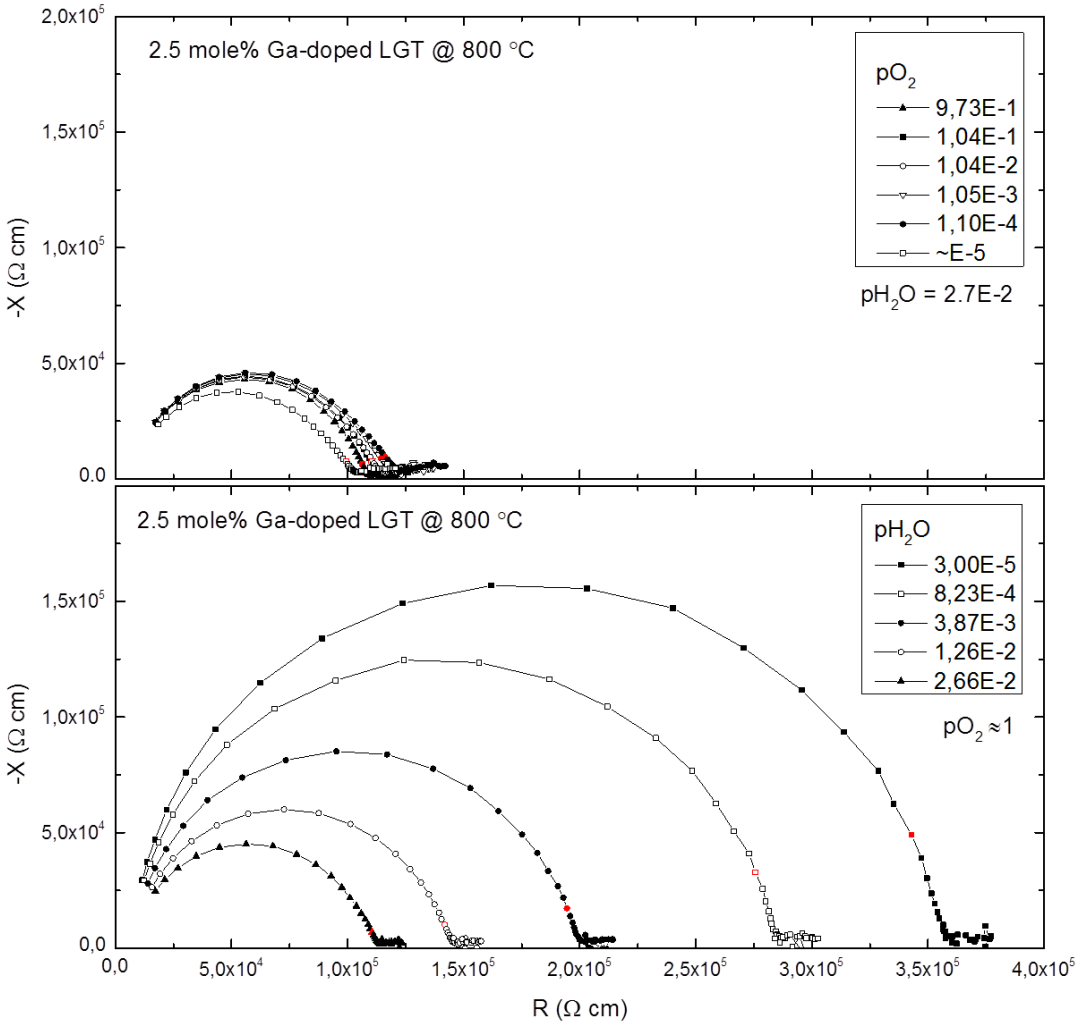

Figure 43 Impedance spectra of acceptor-doped langatate performed at 800 °C at various pO_2 with pH_2O = 0.027 atm (top) and at various pH_2O with pO_2 = 1 atm (bottom). The red points mark the point closest to 10 kHz.

Figure 44 displays the pH_2O (left) dependency on the bulk conductivity at temperatures 700, 800 and 1000 °C. The points are derived from deconvolution of impedance spectra. The effect of the water vapour partial pressure is highest at 700 °C and decreases with increasing temperature. In all cases the slope seems to flatten out at lower partial pressures, however, at higher partial pressures, there is no sign of the curves flattening out. At these partial pressures, the slope is at its highest at 700 °C and decreases at higher temperature. The theoretical slope of protons as minority charge carriers of ½ is displayed in the figure for comparison (see Brouwer diagram, Figure 4, right).

Figure 44 displays the pO_2 (right) dependency at temperatures 800 and 1000 °C. The effect of pO_2 on the bulk conductivity increases with temperature. The slope at 800 °C is quite linear and does not seem to flatten out at either end of the pO_2 scale displayed. At 1000 °C the slope increases some at higher partial pressures. The theoretical slope of holes as minority charge carriers of ¼ is displayed for comparison in the figure (see Brouwer diagram, Figure 4, left). Impedance spectroscopy was not performed at lower temperatures since the dependency on pO_2 was quite weak.

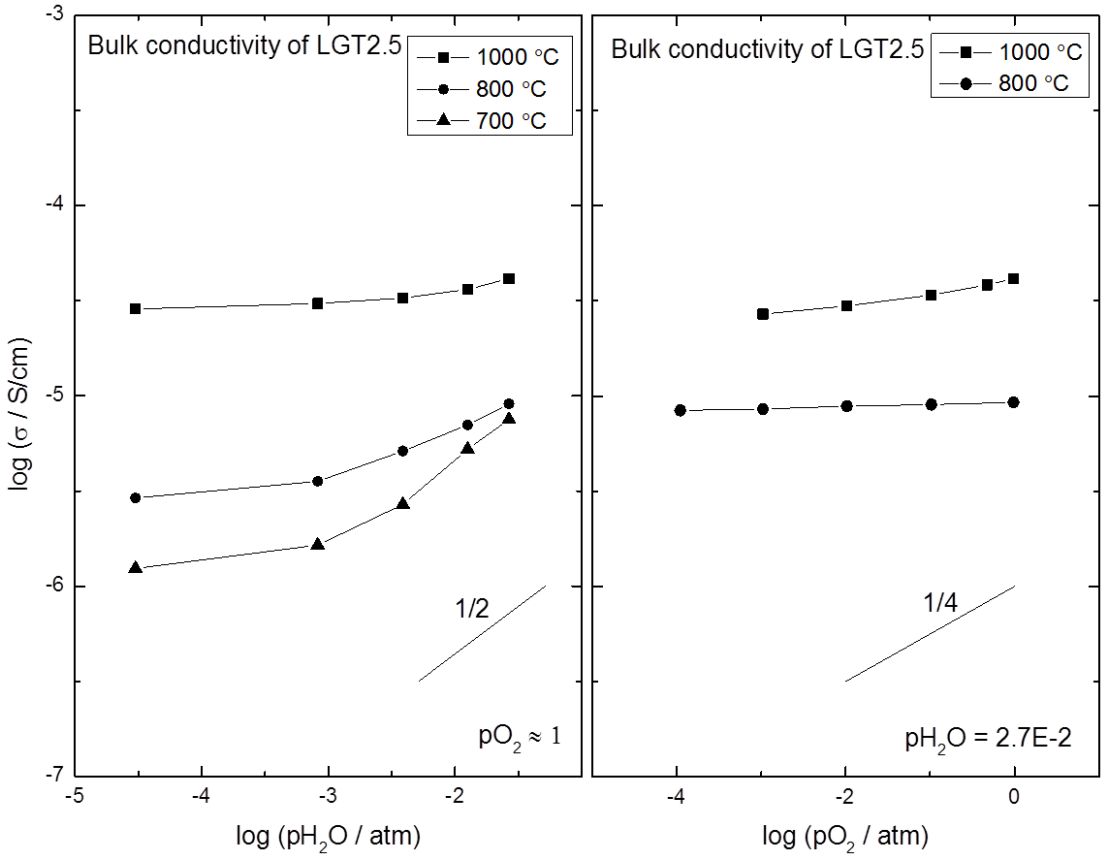

Figure 44 Bulk conductivity as a function of pH_2O (left) and pO_2 (right) of acceptor doped polycrystalline langatate. The points are derived from deconvolution of impedance spectra.

7.4.3 Effects of reducing conditions

Figure 45 displays the bulk conductivity obtained from deconvolution of impedance spectra at 800 °C as a function of pO_2. The measurements were done in hydrogen gas under a water vapour partial pressure of 0.027 atm. The conductivity seems to flatten out at higher pO_2 while at the lowest values it is not easy to determine.

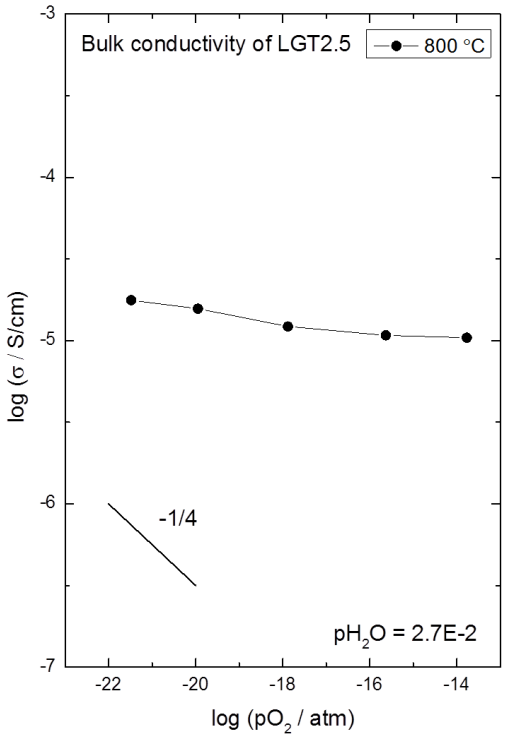

Figure 45 Bulk conductivity as a function of pO_2 of acceptor doped polycrystalline langatate in wet reducing conditions at 800 °C. The points are derived from deconvolution of impedance spectra.

The acceptor-doped langatate was heated up to 1000 °C in the Probostat while the sample was subjected to hydrogen gas. Impedance spectra were done at 800 °C in wet oxidizing conditions both before and after this process, see Figure 46.

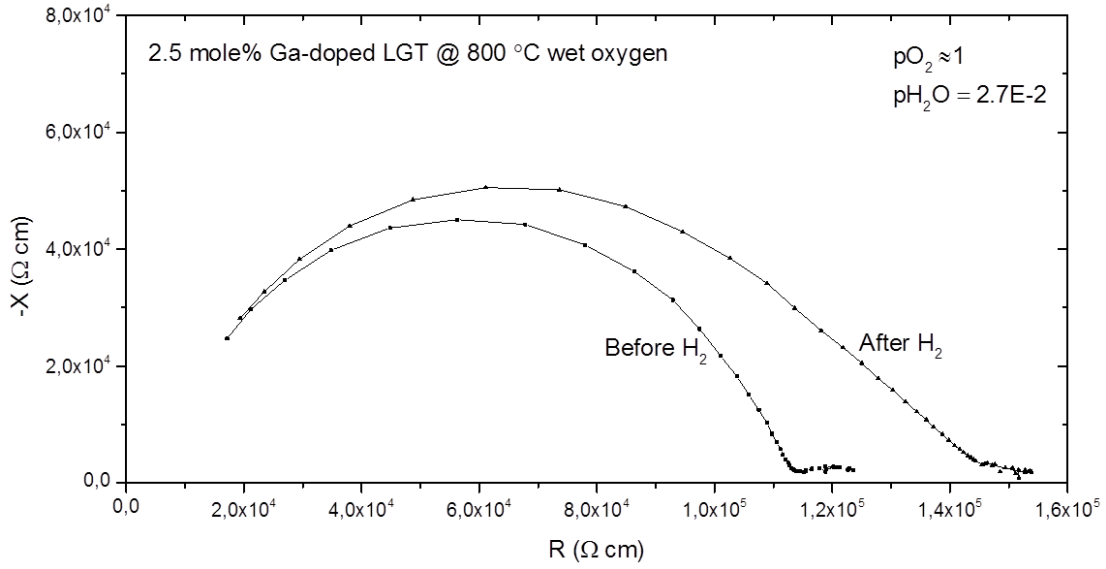

Figure 46 Impedance spectra at 800 °C of the acceptor-doped langatate pellet before and after set in reducing atmosphere at 1000 °C.

As we can observe from the figure, the bulk resistance has increased slightly after the sample has been in reducing conditions at higher temperatures.

7.4.4 Single crystal langatate

Figure 47 displays the constant frequency (10 kHz) measurements (ramps) of the Z-cut (left) and X-cut (right) single crystalline langatate. These curves showed little difference from each other and resembled the ramp of the acceptor doped langatate. Similar to the acceptor-doped langatate, these curves show a change of slope at around 700 °C, indicating a change of the dominating charge carrier. At temperatures below 700 °C, there is no difference in oxygen and argon, as the curves are overlapping. In wet and dry conditions, however, there is a substantial difference. Above this temperature, the curves for wet and dry conditions seem to converge and the difference in conductivity between them diminishes. The curves for oxygen and argon move apart and the difference get bigger.

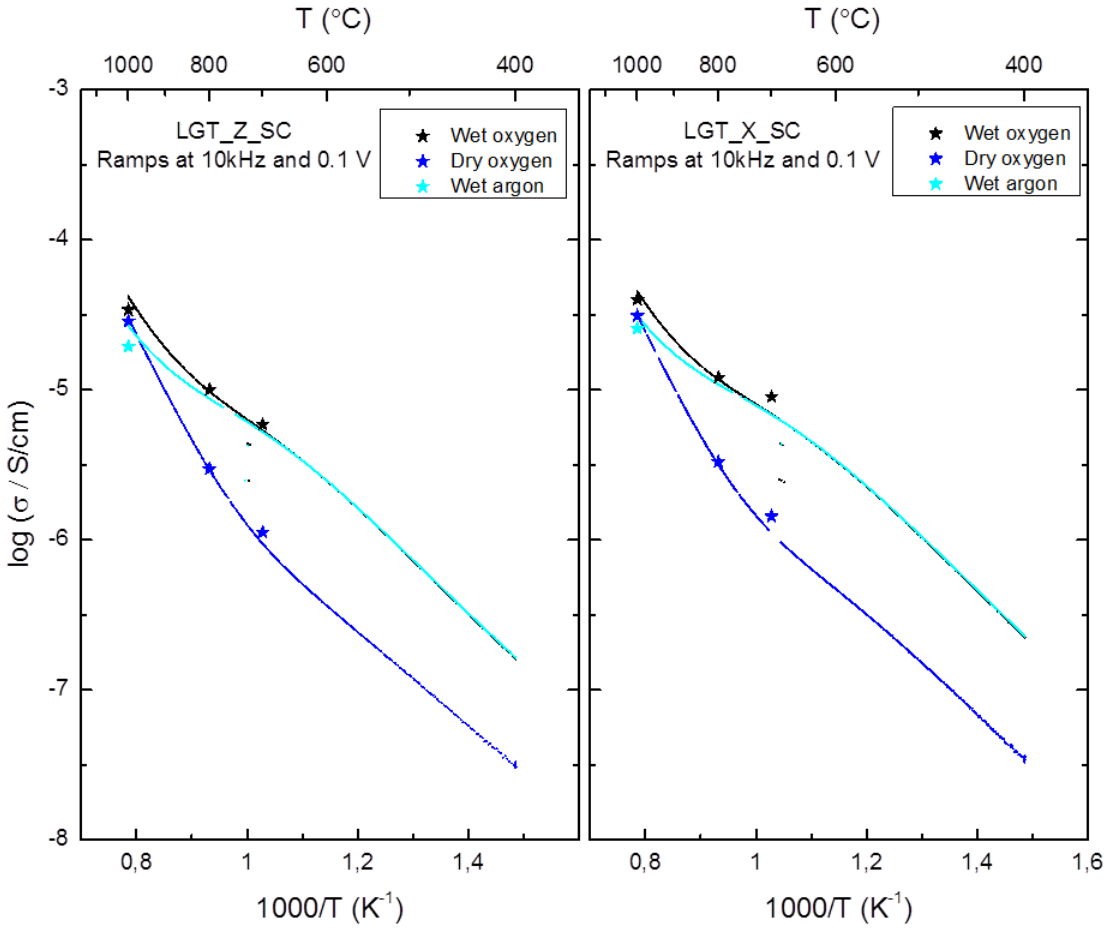

Figure 47 Constant frequency measurement of Z-cut (left) and X-cut (right) single crystal langatate. The solid points show the bulk conductivity as obtained from deconvolution of impedance spectra.

In Table 22 the activation energies of the single crystals measured in wet oxygen are listed. In comparison Davulis *et al.* got a linear curve for the entire temperature range 350 °C to 900 °C and obtained activation energies, E_a, in the Y (σ_{11}) and Z (σ_{33}) directions of 1.04 and 0.95 eV, respectively [21]. These results are more comparable to the polycrystalline undoped langatate measured on in this thesis.

Table 22 Activation energy of the single crystals measured in wet oxygen at different temperature ranges.

Temperature range	**Z-cut LGT (eV)**	**X-cut LGT (eV)**
Low	0.77	0.76
Mid	0.62	0.55
High	1.22	1.13

Figure 48 shows the evolution of the impedance spectra of the Z- and X-cut LGT as temperature changes from 700 °C to 1000 °C. The 10 kHz frequency is in the first semicircle at these temperatures. The impedance spectra for the two single crystals are fairly similar. The semicircles of the impedance spectra of X-cut LGT have a slightly lower resistivity at all temperatures compared with the Z-cut LGT. At 1000 °C, the form of the first semicircle is quite differing in the two cases.

A $(C[(R_1Q_1)(R_2Q_2)(R_2Q_2)])$ circuit was fitted to the impedance spectra at 700 and 800 °C, while $(C[(R_1Q_1)(R_2Q_2)])$ was fitted to the impedance spectra at 1000 °C. In Table 23 the deconvoluted values of the impedance spectra performed in wet oxygen are shown for the different (RQ) elements. These values are corrected for the geometry. As we can see, the first (RQ) element has a capacitance in the bulk range.

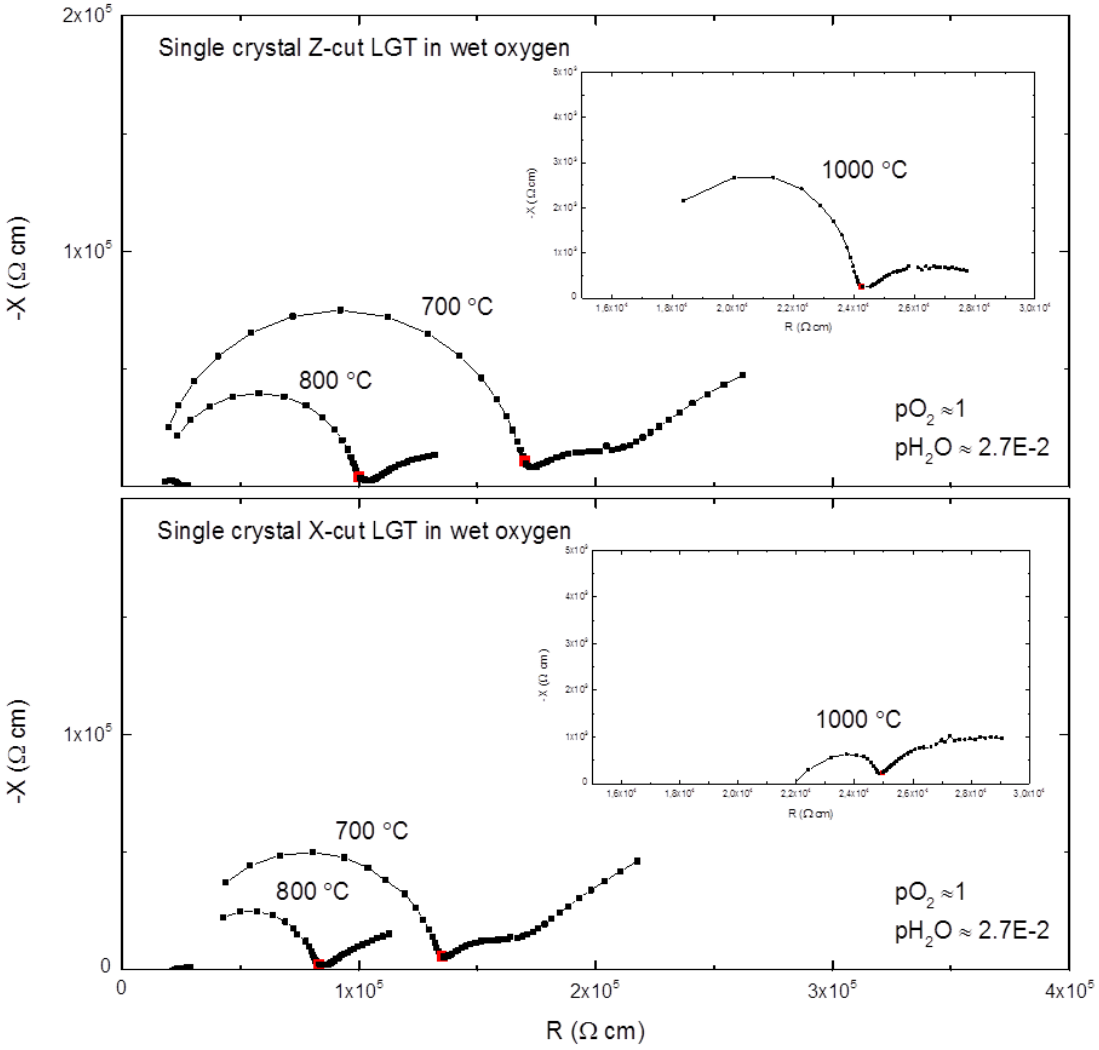

Figure 48 Impedance spectra of the single crystal Z- and X-cut langatate at 700, 800 and 1000 °C. The 10 kHz frequency is shown in red. A magnified image of the 1000 °C impedance spectra is shown as well. The two figures, as well as the magnified, are shown with the same scale.

Impedance spectroscopy of single crystals should ideally only give two contributions; bulk and electrode. However, in Figure 48, we see three distinct semicircles at 700 °C. This could be attributed to the silicon impurities found with EDS (Figure 35) or this could be an effect of the electrode. Since the electrical measurements performed on the single crystals were using a "2 point, 2 wires"-setup, a larger contribution from the electrode compared with the polycrystalline is expected. Inspecting the capacitance of the semicircles obtained from the fitting (Table 23), the contribution from the 2nd semicircle at 700 °C decreases at higher temperature, and is not seen at 1000 °C.

Table 23 The fitted values of the resistivity and specific capacitance of the three semicircles (R_1Q_1) of the single crystal Z-cut langatate at different temperatures in wet oxygen.

	Wet oxygen					
	R_1Q_1		**R_2Q_2**		**R_3Q_3**	
T (°C)	**ρ (Ω cm)**	**C (F/cm)**	**ρ (Ω cm)**	**C (F/cm)**	**ρ (Ω cm)**	**C (F/cm)**
700	1.70E+05	3.28E-12	3.72E+04	2.10E-08	2.62E+05	3.75E-06
800	9.99E+04	2.61E-12	3.42E+03	2.20E-08	7.05E+04	4.39E-06
1000	2.93E+04	1.08E-14	5.49E+03	1.48E-06	-	-

Figure 49 displays the bulk conductivity as a function of pH_2O (left) for both the Z- and X-cut single crystalline langatate. These points were obtained from deconvolution of impedance spectra. The same behaviour as for the acceptor doped polycrystalline langatate is observed; at lower partial pressures, the conductivity seems to flatten out, while at higher partial pressures it approaches a slope of ½. The slope decreases at higher temperatures. There is a slight difference on the slope of the two single crystals. At lower pH_2O, the slopes seem to be parallel while at higher pH_2O the difference increases.

There is a minor effect of pO_2 for both single crystals as seen in Figure 49 (right). The pO_2 dependency does not seem to flatten out at lower partial pressures at 1000 °C. The pO_2 effect diminishes at decreasing temperatures and thus measurements were not performed at lower temperatures.

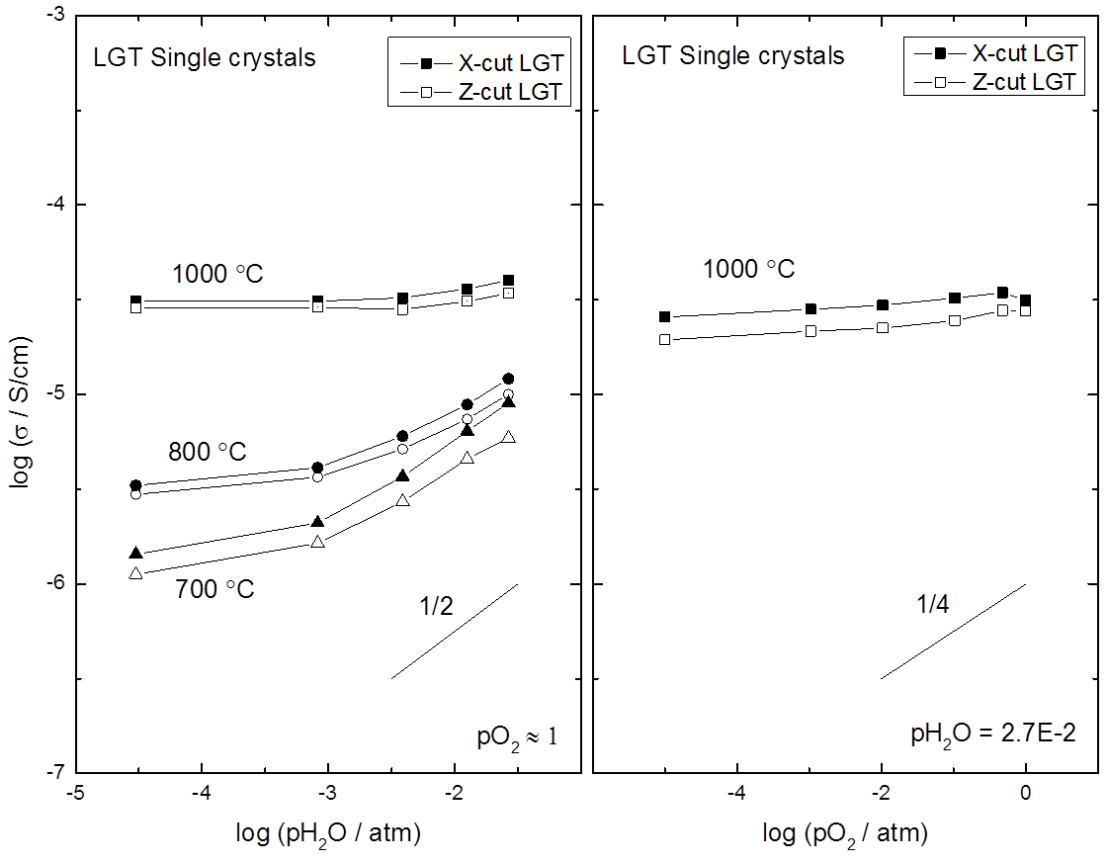

Figure 49 Bulk conductivity as a function of pH_2O (left) and pO_2 (right) on Z- and X-cut single crystalline langatate. The points are derived from deconvolution of impedance spectra.

Impedance spectra of the Z-cut single crystal at different water vapour partial pressure are compared in Figure 50. Bulk resistivity increases when decreasing the pH_2O.

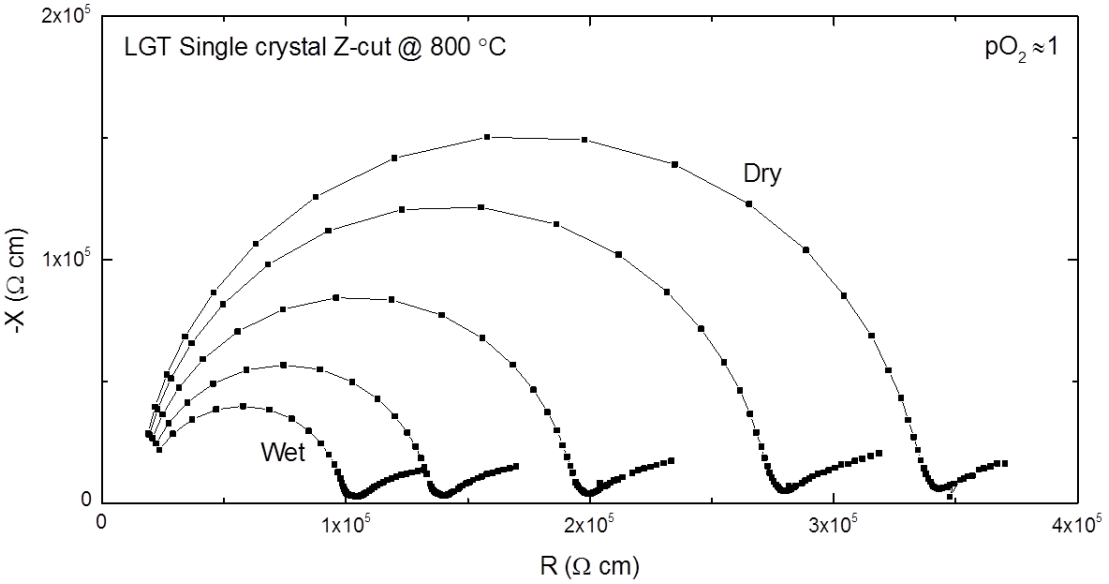

Figure 50 Impedance spectra of Z-cut single crystal langatate at 800 °C at different water vapour partial pressures with the extremes (dry and wet) in each end.

7.4.5 Effects of H_2O vs. D_2O

Figure 51 (left) displays the constant frequency measurements of acceptor doped polycrystalline langatate in H_2O and D_2O wetted argon. The total conductivity in H_2O wetted atmosphere is higher than in D_2O up to 1200 °C, where the two curves seem to converge. Figure 51 (right) displays the constant frequency measurements of Z-cut single crystalline langatate in wet and D_2O oxygen. The total conductivity is higher in wet than in D_2O, however, like the measurements on the polycrystalline the curves seem to converge at higher temperatures. In both cases, the curves for wet and D_2O are quite linear and parallel at temperatures up to 700 °C.

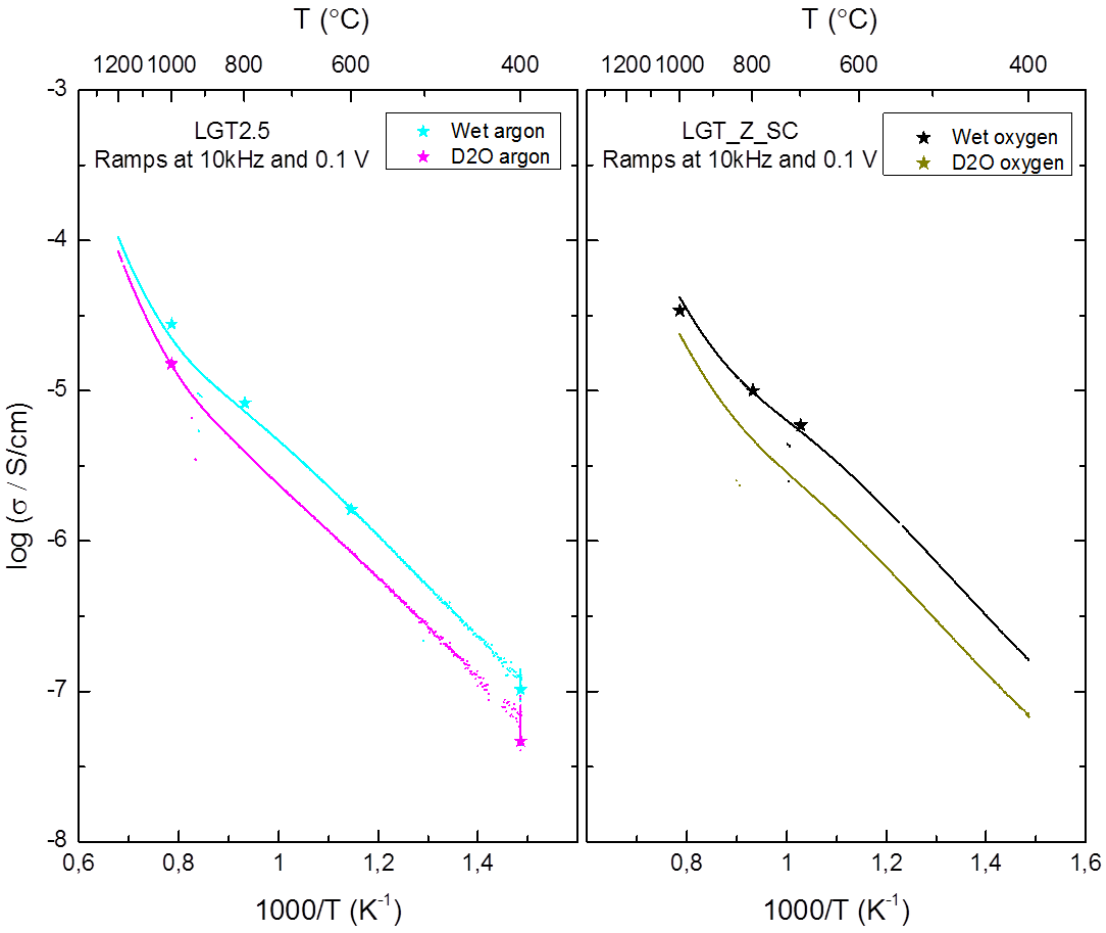

Figure 51 Constant frequency measurements of acceptor doped polycrystalline (left) and Z-cut single crystalline (right) langatate measured in wet and D_2O atmosphere.

Figure 52 displays the ratio of total conductivity in D_2O and H_2O wetted atmosphere (Eq. 52) for the acceptor-doped langatate and the Z- and X-cut single crystals. The data points are derived from chosen points in the ramps, which were done from high temperature to low. As a first approximation a ratio of 0.707 would mean that protons

are the major charge carriers, and a ratio of 1 indicates no proton conductivity. Ideally the ratio should not exceed these values; however as we can see from Figure 52 the ideal case is not upheld. This could be attributed to cation diffusion. Since the D_2O measurements were taken some time after the measurement in H_2O, cation diffusion would lead to a drop in conductivity. The ratio would thus be lower than ideal, as is the case for all samples.

$$\frac{\sigma_{D_2O}}{\sigma_{H_2O}} = \frac{1}{\sqrt{2}} \approx [0.707, 1] \qquad \text{Eq. 52}$$

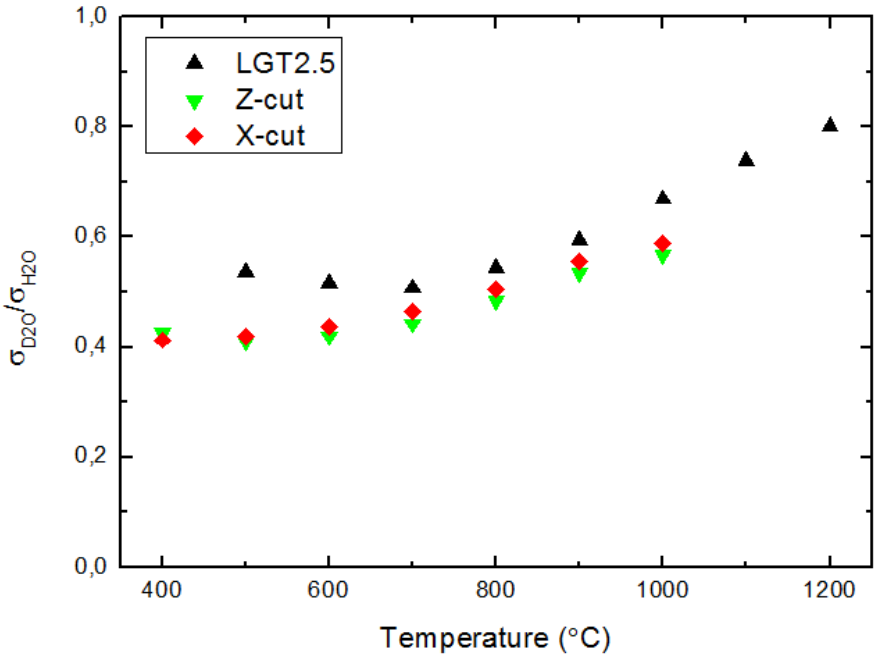

Figure 52 The ratio between the conductivity measured in D_2O and H_2O as a function of temperature. The black points is the ratio for the acceptor-doped langatate measured in argon, while the red and green data points are for the X-cut and Z-cut langatate, respectively, measured in oxygen. The data points are derived from specific temperatures from the ramps.

For acceptor-doped langatate the ratio reaches minima at 700 °C, demonstrating that the transport number of protons reaches its peak, *i.e.* the fraction of the proton conductivity to the total conductivity reaches maxima. The concentration of protons decreases at temperatures above 700 °C as the ratio increases. For the single crystals the transport number reaches a peak at lower temperature. However, this is just a

primitive model, and these data are only used to give a qualitative assessment of protons in the material.

8. Discussion

The results obtained from the experimental results and DFT will be discussed in this chapter. The main focus will be the defect chemistry and transport properties of langatate. Measured values will be compared with values reported in literature.

8.1 DFT

From the calculations of the site preference of tantalum, it can be concluded that tantalum is most stable being six-coordinated at the 1a octahedral site as opposed to the 2d and 3f site (Table 12). These results indicate that the 1a cation site is more easily substituted, *i.e.* when doping langatate; it is the 1a cation site that is affected.

Tantalum at the 2d site would lead to under-coordination of the tantalum ion and this was calculated to be least favourable. However Kaurova *et al.* reported that tantalum in the 3+ oxidation state occupied the 2d tetrahedral. This might be the case as the DFT calculation with tantalum ion on the 2d site did not distort to an octahedron, but remained a tetrahedron. In Table 12 it is observed that tantalum in this site is the least favourable. This could be attributed to the fact that the same electron configuration was used for the calculations on the three different sites, forcing the tantalum to have an oxidation state of 5+. Substituting tantalum at the 3f tetrahedral site lead to some distortions, and the tantalum becomes 6-coordinated. Nevertheless this indicates that tantalum ions with an oxidation state of 5+ are not stable being under-coordinated. This is further strengthened by the calculations on oxygen vacancies. Removal of a doubly charged oxygen bonded to the tantalum at the 1a octahedral site, *i.e.* introducing an oxygen vacancy, results in relaxation of the Ta ion, which renders it 6-coordinated again. In other words the Ta ion attracts another oxide ion to fulfil its original coordination of 6. Gallium ions on the other hand are more stable with one less oxygen ion. However, doubly charged oxygen vacancies seem to be most favourable around the 1a cation (gallium or tantalum) compared with the other sites (Table 15). This is in good agreement with literature; Kuzmicheva *et al.* did neutron diffraction on several single crystalline langatate samples with different composition and reported oxygen vacancies near cation site 1a in all of their samples. [17] Formation of oxygen vacancies on the remaining oxygen sites was not as favourable, although it happened to a small extent. DFT calculations performed by Chung *et al.*

also confirm that oxygen vacancies in the 6g site is more favourable than in the 2d site [24]. However, in either case, it was not reported if the oxygen vacancy near the 1a site had a preference to tantalum or gallium ion. Since the tantalum ions are not stable being under-coordinated and gallium can have a lower coordination, it can be more likely that oxygen vacancies prefer being located near the gallium ions.

The doubly charged oxygen vacancy is the most stable of the oxygen vacancies at lower Fermi level while the neutrally charged oxygen vacancy becomes more stable at higher Fermi level (see Figure 29). The oxygen interstitial becomes more favourable at higher Fermi levels, indicating that it will be the dominating charge-compensating defect in donor doped langatate.

Figure 53 shows the calculated DOS for three hydrogen defects: proton (top), hydrogen atom (middle) and hydride (bottom). As mentioned previously, in the case of the hydrogen atom, the electron is excited to the conduction band and thus leaves behind a proton (Eq. 53).

$$H_i^x = H_i^\bullet + e'_{CB} \qquad \text{Eq. 53}$$

The hydride, however, results in formation of in-gap defect states with valence band character, and the hydrogen atom therefore acts as an acceptor.

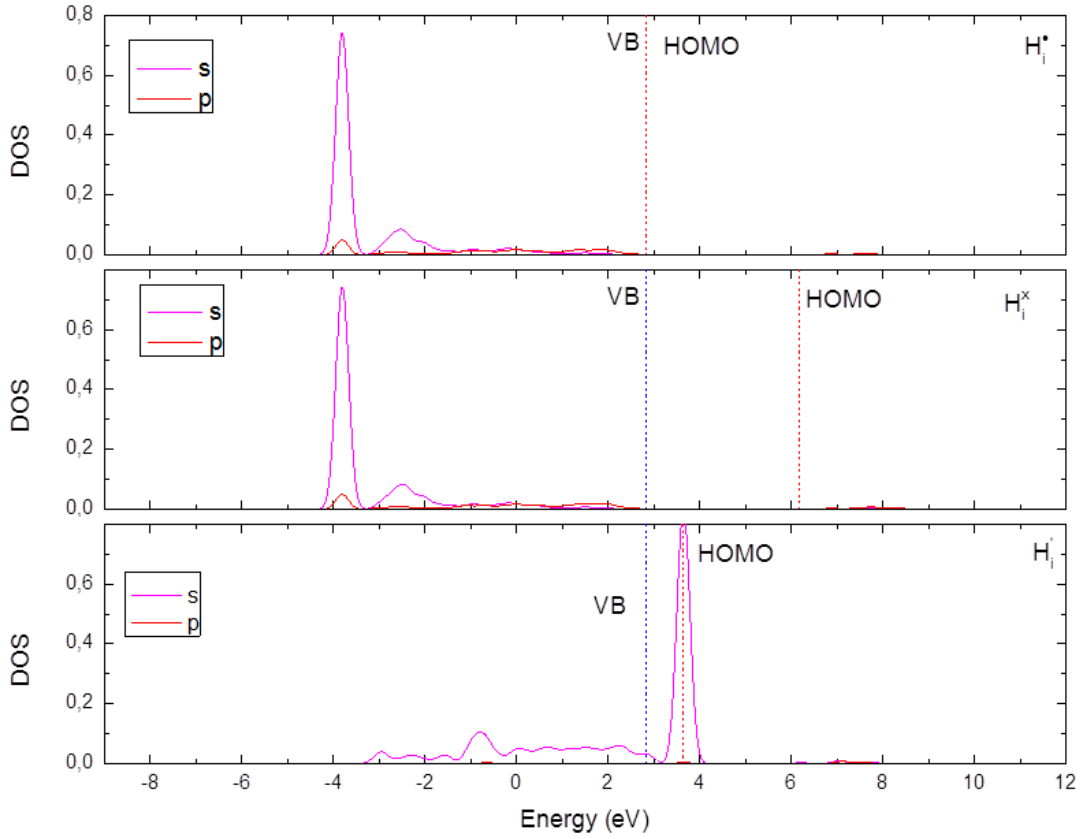

Figure 53 The DOS of the three different hydrogen species; the proton (top), the "hydrogen atom" (middle) and the hydride (bottom).

Formation energy of protons is favourable with the most stable position, listed in Table 16, at -2.04 eV at Fermi level near the valence band edge. As seen in Figure 25 protons prefer being located near gallium atoms. The protons in this figure are within 1 eV from the most stable position and the relative distribution of the energies of these protons is shown in Figure 24. The proton positions with low relative energies give an easier transport route for protons, and there might be a favourable path through the tetrahedral gallium along the xy-plane. However, if the energy difference is too high, the protons get trapped. Even though these calculations were done with no ionic relaxation, they give an indication of the preference of the protons. The most favourable of the gallium sites, however, is the 1a octahedral site (Figure 27).

The hydride takes part in a TaO_6H polyhedral unit. Figure 29 indicates that the hydride always has higher formation energy than the oxygen interstitial. As we can see from Figure 29 the effectively negative charged oxygen interstitial is much more favourable than the effectively negative charged hydride. It has a steeper slope

indicating that the hydride will never surpass the stability of the oxygen interstitial, except at high pH_2.

Oxygen vacancies were shown to have a preference being located near the 1a cation site, and protons preferred being bonded as a hydroxide to gallium ions, preferably octahedral gallium. From these results it can be established that hydration of langatate preferably takes place near the gallium at the 1a site. This reaction has a calculated hydration enthalpy of -0.94 eV (-90 kJ/mol).

We have to remember the limitations of the GGA-PBE potential. This potential is not optimal for calculating the valence band and the conduction band edges. This is the case for all calculations including electrons or holes where the energy of the electron reservoir has been included. The results from UV-VIS-NIR indicate a bandgap near 5 eV (Figure 37) and Chung *et al.* reports a value of 5.3 eV. However we do not know the exact energy of the valence and conduction band edges and this might affect the formation energies of the different defects. For instance the formation energy of the hydride might become negative.

8.2 Comparison of the samples

The polycrystalline were made by solid state synthesis and calcinated and sintered in air with an oxygen partial pressure of roughly 0.21 atm. The single crystals, on the other hand, were grown by Czochralski method with a pO_2 of 0.01 atm. This gives two different synthesis routes as well as two different atmospheres.

Figure 30 shows the colours of the nominally undoped and acceptor doped polycrystalline langatate, as well as the single crystalline langatate. The colour of the nominally undoped langatate is light blue, almost white, while the two other samples are yellow. Comparing the colours with the work done by Kaurova *et al.* presented in Figure 7, the two latter samples should have similar oxygen vacancy content. The colour of the nominally undoped langatate is not as easy to explain from this figure. There might be some effect of impurities or the defect situation in the material.
In all of the measured samples the bulk dominates the total conductivity. Figure 54 displays the constant frequency measurements of all the samples. As can be seen, the

bulk conductivity of the acceptor doped polycrystalline and the single crystals have similar slopes. From this relationship it can be concluded that the defect situation in these samples are similar. The undoped sample on the other hand shows different conductivity behaviour and thus must have a different defect situation. This will be discussed in the following subchapters.

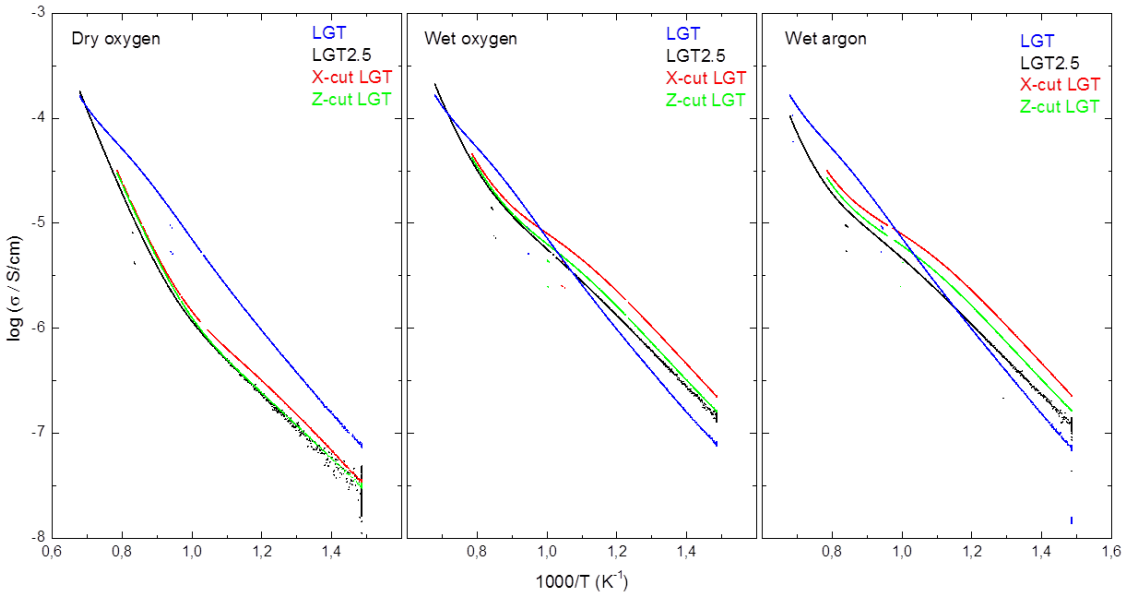

Figure 54 The constant frequency measurements of the 4 different samples measured in this thesis in different atmospheres; the undoped langatate (blue), the acceptor-doped langatate (black) and the X- (green) and Z-cut (red) langatate.

8.3 Nominally undoped langatate

The undoped langatate did not showing any significant effect of either pO_2 or pH_2O on conductivity within the measured temperature interval. This indicates that the contributions to the total conductivity from both electrons/holes and protons are low, leading to the conclusion that the major charge carrier is oxide ions. Since langatate has a disordered cation site which has a ratio that can easily be tipped either way, and the acceptor doped langatate did show effects of both pO_2 and pH_2O, it is fairly likely that the sample is effectively donor doped, *i.e.* tantalum rich, $Ta_{Ga}^{\bullet\bullet}$. Kaurova *et al.* among others report that most of their synthesized samples were effectively donor doped [3] which further strengthens this claim. This must be compensated by an effectively negative charged defect.

Cation vacancies could compensate for the defect; the most significant being lanthanum and gallium vacancies [3] [17]. If we assume that impurity defects are of

low concentration, the electroneutrality is given by Eq. 54. Electronic defects are ignored because of insignificant effects of pO_2.

$$2[Ta_{Ga}^{\bullet\bullet}] = 2[O_i''] + 3[v_{La}'''] + 3[v_{Ga}'''] \quad \text{Eq. 54}$$

The major charge carrier is oxygen interstitial, which has also been reported in langasite [30]. DFT calculations showed that oxygen interstitial become favourable at high Fermi levels, and introduction of a donor introduces states in the bandgap which increase the Fermi level. Cation vacancies can be ruled out because of their low mobility.

From the constant frequency measurement we see that the curves are all practically linear. Activation energy of 0.92± 0.04 eV was obtained from curve fitting. This is comparable to the value Davulis *et al.* obtained from their work on single crystals (1.02 and 0.97 eV for x and z directions, respectively) [21], but far off the values measured by Alp Sehirlioglu *et al.* on their single crystals (0.35 eV and 0.43 eV) [1]. The major charge carriers must be different in these cases. It is not mentioned in their paper in which atmosphere the single crystals were grown. As mentioned in the literature part, the growth atmosphere has a large impact on the composition of crystals. Activation energy for oxygen ion transport of 0.91 eV through vacancies was reported by Seh *et al.* for nominally undoped langasite, which was effectively acceptor doped [31].

The concentration of the oxygen interstitial can be considered constant, and the measured activation energy would thus only reflect the enthalpy of mobility of the interstitial oxygen ion and the total conductivity is given by Eq. 55, resulting in $\Delta H_{mob,O}$ of 89±4 kJ/mol. This value is obtained by fitting Eq. 55 to the constant frequency measurements in each atmosphere and getting an average. This value is comparable to the value calculated by Bjørheim *et al.* for langasite as mentioned in the literature chapter.

$$\sigma_{Tot} = 2F[O_i'']u_{O_i''} = 2F[O_i'']u_{0,O_i''}\frac{1}{T}e^{\frac{-\Delta H_{mob,O}}{RT}} \quad \text{Eq. 55}$$

XRD data of the sintered nominally undoped langatate (Figure 31) does not show any gallium rich secondary phases, which one might have expected for this particular sample since it is donor doped. However, one must consider the limits of XRD and

that the initial mixing and weighing of the oxides for synthesis itself is not 100 % accurate. If we look at the EDS results from the SEM (Figure 36), the undoped langatate seem to have almost double the tantalum content than that of the single crystals and half the gallium content.

8.4 Acceptor-doped langatate

A simplified electroneutrality for the acceptor doped langatate is expressed by Eq. 56. Vacancies at the gallium site have not been reported in gallium rich langatate and thus are not included in the electroneutrality. The following part is discussed along with the Brouwer diagram presented in Figure 4 and the pO_2 and pH_2O dependencies shown in Figure 44.

$$2[v_O^{\bullet\bullet}] + [OH_O^{\bullet}] + p = 2[Ga'_{Ta}] + 3[v'''_{La}] + n \qquad \text{Eq. 56}$$

The isotope effect (Figure 52) gives strong indication that there are protons in the material. At 700 °C the conductivity increases with $p_{H_2O}^{1/2}$ (Figure 44) indicating a region where oxygen vacancies compensate for the acceptor. However, the conductivity does not seem to flatten out at higher pH_2O in the temperature range 700 to 1000 °C indicating that oxygen vacancies compensate for the acceptor in the entire pH_2O range measured. The conductivity from the pO_2 dependencies do not show any sign of flattening out at higher pO_2 either. This indicates that holes never fully compensates for the acceptor. If we assume the concentration of lanthanum vacancies to be insignificant compared with the gallium acceptor concentration, the electroneutrality can be simplified to Eq. 57.

$$[v_O^{\bullet\bullet}] = [Ga'_{Ta}] \qquad \text{Eq. 57}$$

It is seen that the pO_2 dependency on the conductivity is low at lower temperatures but do become more significant at higher temperature, reaching a slope of approximately 1/10 at 1000 °C, which indicate an increasing contributions from holes to the total conductivity. However the dependency does not reach $p_{O_2}^{1/4}$ indicating that there are other significant contributions to the conductivity. In reducing atmosphere electrons become charge carriers in the expense of holes (Figure 45).

The pH_2O dependencies give a slope of approximately ½ at 700 °C, 2/5 at 800 °C and 1/10 at 1000 °C. This indicates that protons are the majority charge carriers at 700 °C while at higher temperatures contributions from oxide ions becomes more significant. The conductivities do seem to flatten out at lower pH_2O indicating contributions from oxide ions. However, given the higher mobility of the protons compared with oxygen, the protons dominate the conductivity at least up to 700 °C in wet conditions. Between 700 °C and 800 °C there seems to be a change in the slope of the conductivity as seen on the constant frequency measurements (Figure 38). This can indicate a change in the majority charge carrier. At temperatures above 700 °C, the pH_2O dependency diminishes, and in context with the pO_2 dependency, the majority charge carrier must be ionic, and thus oxygen vacancy. At temperatures below 700 °C, however, the conductivity might flatten out at higher pH_2O and go into a region where protons compensate the acceptor. However this has to be investigated further.

Tablecurve was used to model the partial conductivities from the constant frequency measurements. The following model was used to fit the measurements:

$$\sigma_{Tot} = e\left(2[v_O^{\bullet\bullet}]u_{v_O^{\bullet\bullet}} + [OH_O^{\bullet}]u_{OH_O^{\bullet}} + pu_p\right) \quad \text{Eq. 58}$$

The mobility of the species, u_i, is expressed by Eq. 14, while the concentrations were given by the following equations, which were derived from the electroneutrality, hydration reaction and the reaction of formation of holes.

$$[OH_O^{\bullet}] = \frac{-1 + \sqrt{1 + 16\frac{[Ga_{Ta}'']}{K_{Hydr}[O_O^x]p_{H_2O}}}}{\frac{4}{K_{Hydr}[O_O^x]p_{H_2O}}} \quad \text{Eq. 59}$$

$$[v_O^{\bullet\bullet}] = [Ga_{Ta}''] - \frac{1}{2}[OH_O^{\bullet}] \quad \text{Eq. 60}$$

$$p = \left(\frac{[v_O^{\bullet\bullet}]p_{O_2}^{1/2}}{K_{v_O^{\bullet\bullet}}[O_O^x]}\right)^{1/2} \quad \text{Eq. 61}$$

It can be assumed that the total conductivity is dominated by bulk. Figure 55 displays the plots from the curve fitting. The figure shows the extracted partial proton, oxide ion and electron hole conductivities. The total conductivity is also displayed. For these fittings 10 parameters were used, and the concentration of the dopant $[Ga''_{Ta}]$ was set to 0.025 mole fractions. Since there are a lot of variables, some guidelines were followed. The enthalpy of hydration was set to be around the calculated DFT value of approximately -90 kJ/mol.

From pH_2O measurements the sum of the partial conductivity of the oxide ion and electron hole was extracted. The "rest conductivity" was derived for 700, 800 and 1000 °C and used as a guideline to fit the sum of these partial conductivities. The fitted values are displayed in Table 24. These values were set to remain the same for all three atmospheres and the only values that were allowed to differ were the pre-exponential terms for the mobility, listed in Table 25. However some of these values were interchangeable and will not be emphasised in this thesis.

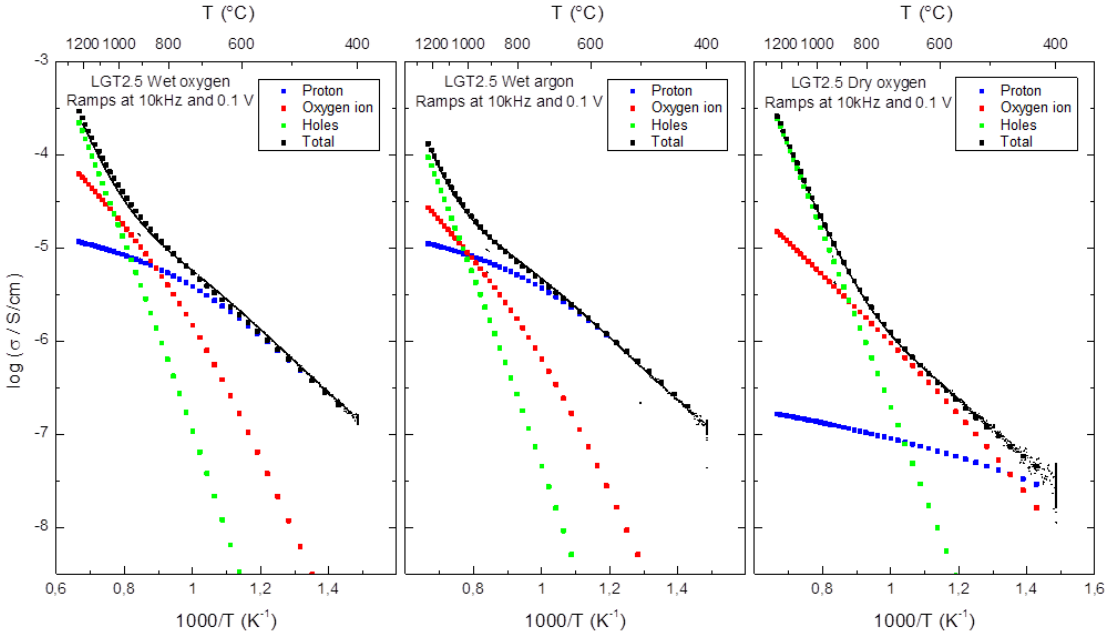

Figure 55 Curve fitting of the constant frequency measurements in wet oxygen (left), wet argon (middle) and dry oxygen (right) of the acceptor doped polycrystalline langatate. The proton conductivity is shown in blue, oxygen ions in red, holes in green and the total conductivity in black squares.

Fitting of the constant frequency measurements with ten parameters yields a good fit. However, with ten variable parameters the significances of some of the values are low. The enthalpy of mobility of the proton is quite accurate as we assume the proton conductivity dominates at temperatures below 700 °C in wet conditions, giving a value of approximately 70±0.5 kJ/mol, which is comparable with the value for langasite calculated by Bjørheim *et al.* of 78±4 kJ/mol.

Table 24 Fitted parameters for the total conductivity measurements for the acceptor doped polycrystalline langatate. The enthalpies have units of kJ/mol and the entropies have units of J/mol*K. These values remained constant for the three curves in **Figure 55**.

ΔH_{Hydr}	ΔS_{Hydr}	$\Delta H_{f,vO}$	$\Delta S_{f,vO}$	$\Delta H_{mob,H}$	$\Delta H_{mob,vO}$	$\Delta H_{mob,p}$
-90	-97	-77	-110	70	78	150

Table 25 Fitted parameters for the total conductivity measurements. The pre-exponential terms are listed here for the three different curves in **Figure 55** with units of cm^2K/Vs.

	Wet oxygen	**Wet argon**	**Dry oxygen**
$u_{0,H}$	1.0	0.88	0.35
$u_{0,vO}$	1.8	0.96	0.43
$u_{0,p}$	0.52	3.9	0.52

8.5 Single crystal langatate

The defect situation in the single crystals is comparable to acceptor doped polycrystalline LGT. As seen in Figure 49 pO_2 and pH_2O dependencies are similar to the acceptor doped polycrystalline sample. Since the same behaviour is observed in the electrical measurements at the different temperatures and atmosphere, it can be concluded that these particular single crystals are effectively acceptor doped, and Eq. 57 is also valid for these samples. The same defect situation and charge carriers as mentioned in the previous chapter, is presumed to be valid for these samples as well.

Tablecurve was used to fit the constant frequency measurements performed on the Z-cut single crystalline langatate (Figure 56). The same acceptor concentration used for the polycrystalline was used for these fittings. However this value is very speculative, as we do not know the exact acceptor concentration.

The same method as for the acceptor doped polycrystalline langatate to fit these data was used. As was the case for the polycrystalline, the significance of some of the parameters is quite low. The enthalpy of mobility of the proton is quite accurate, giving a value of approximately 73±0.5 kJ/mol which is comparable to the value calculated for the acceptor doped polycrystalline langatate. For the X-cut single crystalline langatate a value of 73±0.5 kJ/mol was obtained (not shown).

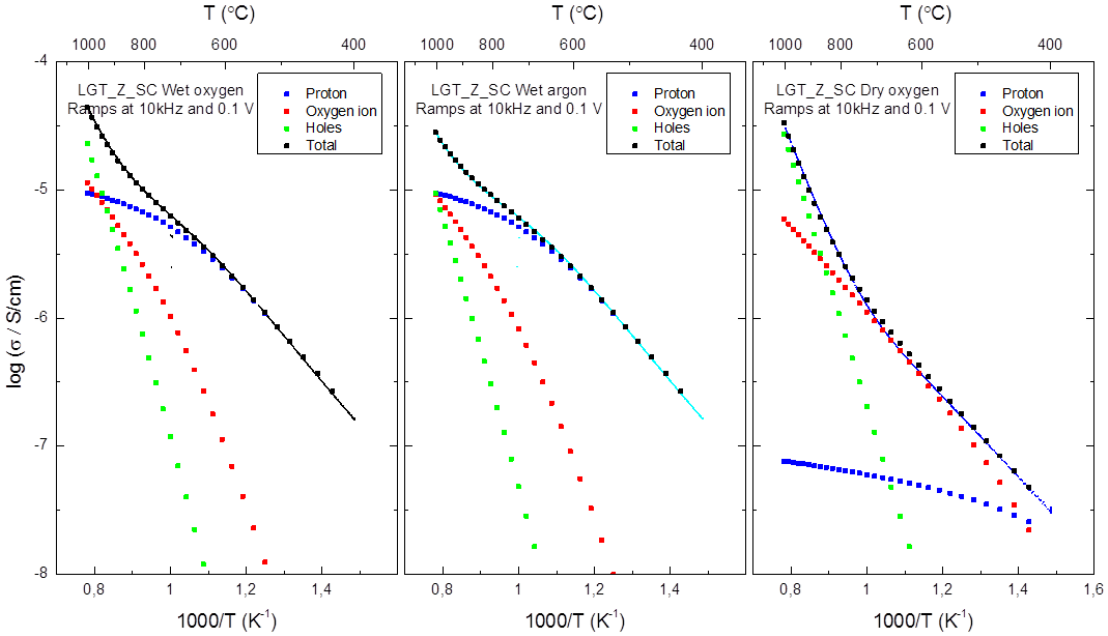

Figure 56 Curve fitting of the constant frequency measurements in wet oxygen (left), wet argon (middle) and dry oxygen (right) of the Z-cut single crystalline langatate. The proton conductivity is shown in blue, oxygen ions in red, holes in green and the total conductivity in black squares.

Table 26 Fitted parameters for the total conductivity measurements for Z-cut single crystalline langatate. The enthalpies have units of kJ/mol and the entropies have units of J/mol*K. These values remained constant for the three curves in **Figure 56**.

ΔH_{Hydr}	ΔS_{Hydr}	$\Delta H_{f,vO}$	$\Delta S_{f,vO}$	$\Delta H_{mob,H}$	$\Delta H_{mob,vO}$	$\Delta H_{mob,p}$
-110	-120	-110	-102	73	72	140

Table 27 Fitted parameters for the total conductivity measurements. The pre-exponential terms are listed here for the three different curves in **Figure 56** with units of cm^2K/Vs.

	Wet oxygen	**Wet argon**	**Dry oxygen**
$u_{0,H}$	2.0	2.0	0.42
$u_{0,vO}$	0.61	0.49	0.25
$u_{0,p}$	1.6	12	1.7

There are some differences between the two single crystals. The pH_2O dependencies shown in Figure 49 shows a slightly higher conductivity for the X-cut crystal and a steeper slope at all temperatures measured. The higher conductivity could be attributed to the uncertainty in the measured electrode area. The difference in slopes, however, might indicate an anisotropic effect. According to these data, proton transport seems to be more favourable along the xy-plane compared with the z-direction. DFT calculations showed that protons prefer being located in the proximity of gallium atoms and from Figure 25 we see that proton positions within 1 eV from the most stable one are all distributed along the gallium ions in the xy-plane.

The values for the hydration enthalpy and entropy for the polycrystalline and single crystals are highly uncertain, and further investigation is needed to assess these values. However it can be concluded that langatate is a modest proton conductor compared to the oxides displayed in Figure 2.

8.6 Possible commercial uses

The effectively donor doped langatate do not show any significant effect of either pH_2O or pO_2 up to at least 1200 °C. This property makes it ideal for use as a piezoelectric in an environment where the atmosphere changes, for instance in-situ SEM with variable temperature and atmospheric conditions.

Both the acceptor doped polycrystalline and single crystalline langatate, on the other hand, shows relatively high sensitivity for pH_2O at temperatures up to 700 °C, which could make it useful as a humidity sensor at higher temperatures. At higher temperatures, however, this material becomes a mixed ionic-electronic conductor in oxidizing conditions. And at 1200 °C in reducing atmosphere, the material shows sign of degradation.

In the literature chapter it was reported that Davulis measured activation energies on single crystal langatate of 1±0.05 eV. Comparing with the activation energy measured on the effectively donor doped polycrystalline it is probable that these have similar defect situation, and oxygen interstitial is the major charge carrier in both cases. Thus

by controlling the growth conditions, single crystalline langatate can be tuned to become either effectively donor or acceptor doped.

8.7 Further work

The composition of the samples should be investigated further to get more accurate numbers. Electron probe microanalyzer (EPMA) is an excellent tool for this. Also neutron diffraction can be utilized to examine site occupancy. Langatate with a higher dopant level can be synthesized, and with EPMA, a correlation between the acceptor level and proton content can be made. It would also be interesting to examine the effect of other dopants on both the 1a cation site and the lanthanum site.

Examining the effect of the different defect situations on the piezoelectric properties of langatate would also be quite interesting, as well as how these properties vary with doping level and dopant type.

Nudged elastic band calculations could be done to investigate activation energies of different defect species and obtain enthalpies of mobility for comparison with the impedance measurements.

9. Conclusions

The defect chemistry of nominally undoped and acceptor doped langatate, as well as single crystalline langatate, was investigated through AC impedance spectroscopy and DFT calculations.

When doping with excess tantalum or gallium, the dopant is most probably introduced to the disordered cation site 1a. This is supported by DFT results. By manipulating the Ga/Ta ratio at this site, one can effectively dope langatate with acceptors or donors. Decreasing this ratio below unity, leads to tantalum ions substituting gallium ions and making the sample donor doped. According to the conductivity measurements, donor doping lead to the dopant being compensated by cation vacancy and interstitial oxygen, where the latter would be the major charge carrier, making this a pure oxide ion conductor up to at least 1200 °C. Donor-doped langatate with excess tantalum does not get hydrated at high water vapour pressures, and langatate with this composition is ideal for use as a piezoelectric in a variable atmosphere up to high temperatures, as the influence of pO_2 and pH_2O is insignificant. From impedance measurements, the enthalpy of mobility of the oxygen interstitial was calculated to be 89±4 kJ/mol.

Increasing the Ga/Ta ratio would substitute the tantalum ions with gallium ions and make the sample acceptor doped. This is in turn compensated by doubly charged oxygen vacancies. Acceptor doped langatate is a mixed ionic-electronic conductor depending on the temperature. At temperatures below 700 °C the material is a pure ionic conductor. In wet conditions the major charge carrier is protons while in dry conditions it is oxide ions. At higher temperatures the concentration of protons drops and its contribution to the total conductivity decreases while the contribution from oxide ions increases. In oxidizing conditions, the contribution from electron holes increase. From impedance measurements enthalpy of mobility of protons was calculated to be 70±0.5 kJ/mol.

From DFT calculations using GGA-PBE potential hydration of the most stable oxygen vacancy yields hydration enthalpy of -90 kJ/mol, which give a good fit with the impedance measurements. The DFT results indicate that hydration involves

vacancies and protons near gallium ions, most preferably at the 1a octahedral site. Increasing the gallium content might be favourable to increase the proton content in the material and might give a higher mobility as well.

The single crystals measured in this thesis have the same defect situation as the acceptor doped polycrystalline, *i.e.* gallium rich. However there seem to be a slightly anisotropic effect between the X- and Z-cut single crystals. Proton transport might be somewhat easier in the xy-plane compared with the z-direction. This could be attributed to the protons preference to the oxygen bonded to the gallium atoms as indicated from DFT. However langatate is a modest proton conductor compared to the oxides used for this purpose.

10. References

1. Alp Sehirlioglu, A.S., Christine Klemenz, *High-Temperature Properties of Piezoelectric Langatate Single Crystals.* 2007.

2. Schulz, M., et al., *Electromechanical properties and defect chemistry of high-temperature piezoelectric materials.* Ionics, 2009. **15**(2): p. 157-161.

3. Kaurova, I.A., et al., *Composition, structural parameters, and color of langatate.* Inorganic Materials, 2010. **46**(9): p. 988-993.

4. Rahtu, A. and M. Ritala, *Compensation of temperature effects in quartz crystal microbalance measurements.* Applied Physics Letters, 2002. **80**(3): p. 521-523.

5. Bjørheim, T.S., *Defects in piezoelectric La3Ga5SiO14.* 2012.

6. Fritze, H., *High-temperature piezoelectric crystals and devices.* Journal of Electroceramics, 2011. **26**(1): p. 122-161.

7. Haile, S.M., G. Staneff, and K.H. Ryu, *Non-stoichiometry, grain boundary transport and chemical stability of proton conducting perovskites.* Journal of Materials Science, 2001. **36**(5): p. 1149-1160.

8. Cherry, M., et al., *Computational Studies of Protons in Perovskite-Structured Oxides.* The Journal of Physical Chemistry, 1995. **99**(40): p. 14614-14618.

9. Ray, H.L., N. Zhao, and L.C. De Jonghe, *Hole percolation and proton conduction in monazite solid solutions: La0.98−xCexSr0.02PO4−δ.* Electrochimica Acta, 2012. **78**(0): p. 294-301.

10. Kao, K.C., *Dielectric phenomena in solids*. 2004: Academic Press.

11. Kreuer, K.D., *PROTON-CONDUCTING OXIDES.* Annual Review of Materials Research, 2003. **33**(1): p. 333-359.

12. Norby, T., *Proton Conductivity in Perovskite Oxides*, in *Perovskite Oxide for Solid Oxide Fuel Cells*, T. Ishihara, Editor. 2009, Springer US. p. 217-241.

13. Per Kofstad, T.N., *Defects and Transport in Crystalline Solids.* 2012.

14. Norby, T., *Electrical Measurements.*

15. Sholl, D.S. and J.A. Steckel, *What is Density Functional Theory?*, in *Density Functional Theory*. 2009, John Wiley & Sons, Inc. p. 1-33.

16. Pavlovska, A., et al., *Pressure-induced phase transitions of piezoelectric single crystals from the langasite family: La3Nb0.5Ga5.5O14 and La3Ta0.5Ga5.5O14.* Acta Crystallographica Section B, 2002. **58**(6): p. 939-947.

17. Kuz'micheva, G.M., et al., *The color of langatate crystals and its relationship with composition and optical properties.* Crystal Research and Technology, 2012. **47**(2): p. 131-138.

18. Kuzmicheva, G.M., et al., *A family of langasite: growth and structure.* Journal of Crystal Growth, 2005. **275**(1–2): p. e715-e719.

19. Georgescu, S., et al. *Eu-doped langasite, langatate and langanite-possible new red phosphors*. in *Romanian Conference on Advanced Materials, Brasov, Romania*. 2009.

20. Axtal. *Langatate Main Properties*. Available from: http://www.axtal.com/info/LGT%20properties.pdf.

21. Davulis, P. and M.P. da Cunha. *Conductivity and complex permittivity of langatate at high temperature up to 900°C*. in *Frequency Control Symposium (FCS), 2010 IEEE International*. 2010.

22. Davulis, P.M. and M.P. da Cunha, *A full set of langatate high-temperature acoustic wave constants: elastic, piezoelectric, dielectric constants up to 900°c.* Ultrasonics, Ferroelectrics and Frequency Control, IEEE Transactions on, 2013. **60**(4): p. 824-833.

23. Chung, C.-Y., et al., *First principles calculation of La[sub 3]Ta[sub 0.5]Ga[sub 5.5]O[sub 14] crystal with acceptor-like intrinsic point defects.* Journal of Applied Physics, 2010. **108**(11): p. 113505-7.

24. Chung, C.-Y., et al., *GW calculations on La3Ta0.5Ga5.5O14 with oxygen vacancies at non-equivalent sites.* Computational Materials Science, 2012. **54**(0): p. 43-47.

25. Chung, C.-Y., et al., *Atomistic configurational effects on piezoelectric properties of La3Ta0.5Ga5.5O14 and a new piezoelectric crystal design.* Acta Materialia, 2011. **59**(16): p. 6473-6479.

26. Kuz'micheva, G.M., et al., *Point defects in langatate crystals.* Crystallography Reports, 2009. **54**(2): p. 279-282.

27. Hafner, J., *Ab-initio simulations of materials using VASP: Density-functional theory and beyond.* J Comput Chem, 2008. **29**(13): p. 2044-78.

28. Shannon, R.D., *Revised effective ionic radii and systematic studies of interatomic distances in halides and chalcogenides.* Acta Crystallographica Section A, 1976. **32**(5).

29. Chung, C.-Y., et al., *First principles calculations of oxygen vacancy in langatate crystal.* Solid State Ionics, 2012. **206**(0): p. 1-6.

30. Taishi, T., et al., *Oxygen defects in langasite (La3Ga5SiO14) single crystal grown by vertical Bridgman (VB) method.* Physica B: Condensed Matter, 2007. **401–402**(0): p. 437-440.

31. Seh, H. and H.L. Tuller, *Defects and transport in langasite I: Acceptor-doped (La3Ga5SiO14).* Journal of Electroceramics, 2006. **16**(2): p. 115-125.